AFRL-OSR-VA-TR-2013-0081

Printable Silicon Nanomembranes for Solar-Powered, Bi-Directional Phased-Array-Antenna Communication System on Flexible Substrates

Harish Subbaraman
Omega Optics, Inc.

April 2013
Final Report

AIR FORCE RESEARCH LABORATORY
AF OFFICE OF SCIENTIFIC RESEARCH (AFOSR)
ARLINGTON, VIRGINIA 22203
AIR FORCE MATERIEL COMMAND

REPORT DOCUMENTATION PAGE

Form Approved
OMB No. 0704-0188

Public reporting burden for this collection of information is estimated to average 1 hour per response, including the time for reviewing instructions, searching data sources, gathering and maintaining the data needed, and completing and reviewing the collection of information. Send comments regarding this burden estimate or any other aspect of this collection of information, including suggestions for reducing this burden to Washington Headquarters Service, Directorate for Information Operations and Reports, 1215 Jefferson Davis Highway, Suite 1204, Arlington, VA 22202-4302, and to the Office of Management and Budget, Paperwork Reduction Project (0704-0188) Washington, DC 20503.
PLEASE DO NOT RETURN YOUR FORM TO THE ABOVE ADDRESS.

1. REPORT DATE *(DD-MM-YYYY)* 02/13/2013	**2. REPORT TYPE** Final Report	**3. DATES COVERED** *(From - To)* 11/14/2010 - 11/13/2012

4. TITLE AND SUBTITLE
Printable Silicon Nanomembranes for Solar-Powered, Bi-Directional Phased-Array-Antenna Communication System on Flexible Substrates

5a. CONTRACT NUMBER
FA9550-11-C-0014

5b. GRANT NUMBER

5c. PROGRAM ELEMENT NUMBER

6. AUTHOR(S)
Harish Subbaraman, PI (Omega Optics, Inc)

5d. PROJECT NUMBER
PR/MIPR: F1ATA00293B025

5e. TASK NUMBER

5f. WORK UNIT NUMBER

7. PERFORMING ORGANIZATION NAME(S) AND ADDRESS(ES)
Omega Optics, Inc - 10306 Sausalito Dr, Austin, TX 78759
The University of Texas at Austin - Austin, TX 78758

8. PERFORMING ORGANIZATION REPORT NUMBER

9. SPONSORING/MONITORING AGENCY NAME(S) AND ADDRESS(ES)
AFOSR/NE 875 North Randolph Street
Suite 325, Room 3112, Arlington VA 22203
Phone: 703-696-6221
Program Manager: Dr Gernot Pomrenke,
email: gernot.pomrenke@afosr.af.mil

10. SPONSOR/MONITOR'S ACRONYM(S)

11. SPONSORING/MONITORING AGENCY REPORT NUMBER
AFRL-OSR-VA-TR-2013-0081

12. DISTRIBUTION AVAILABILITY STATEMENT
Distribution Statement A. Approved for public release; distribution is unlimited.

13. SUPPLEMENTARY NOTES

14. ABSTRACT
Report developed under STTR contract for topic AF08-BT08. In the Phase II program, we have several important achievements related to silicon nanomembrane (SiNM) technology. We developed different SiNM transfer schemes that can enable development of intricate photonic devices on any substrate. In order to couple light efficiently into SiNM devices, we developed a subwavelength grating (SWG) coupler, that can achieve over 40% coupling efficiency using a fiber. Several components crucial for a conformal phased array antenna system, including compact modulator with highest slow down factor, PCW TTD lines with >216ps delay, 1x16 MMI power splitters for array functionality, printed PAA system operation etc were demonstrated. For the first time, demonstration of SiNM photonic devices on other substrates such as glass, Kapton etc was performed. These achievements will lead to the widespread development and use of SiNM based high performance photonic components in several air-borne and space-borne applications.

15. SUBJECT TERMS
STTR Report: Flexible photonics, silicon nanomembrane, subwavelength grating coupler, photonic crystal waveguides, slow-light, modulator, nanomembrane transfer

16. SECURITY CLASSIFICATION OF:			**17. LIMITATION OF ABSTRACT** SAR	**18. NUMBER OF PAGES**	**19a. NAME OF RESPONSIBLE PERSON** Harish Subbaraman, PI
a. REPORT U	**b. ABSTRACT** U	**c. THIS PAGE** U			**19b. TELEPONE NUMBER** *(Include area code)* 512-996-8833, Ext 603

Standard Form 298 (Rev. 8-98)
Prescribed by ANSI-Std Z39-18

Table of contents

2. BRIEF SUMMARY OF WORK

In this AFOSR Phase II program, we worked on developing SiNM based components for light-weight and flexible solar-powered bi-directional phased array antenna communication systems. We have several achievements in this program that will be extremely beneficial for the development of next generation high-performance SiNM based high performance devices on flexible substrates..

One important aspect of the program is to show the efficient transferability of SiNMs onto other substrates. The transfer methods have to be universal, and should facilitate transfer of electronic as well as highly complex photonic structures. Therefore, in this program, we developed and optimized three SiNM transfer techniques, each of which can be used for several unique applications. In the first method, we use photoresist as a mechanical support and utilize a stamp to transfer the fabricated devices from SOI onto other substrates [1]. In the second method, we developed a modified version of the first method in order to introduce pedestals underneath waveguides [2]. The presence of these pedestals tremendously improves the transfer yield, and we can achieve >95% yield using this method. In the third method, we use a bonding and etching process in order to transfer large-area unpatterned SiNM onto other substrates [3, 4]. The advantage of this approach is that the availability of large area SiNM on other substrates enable development of fully integrated systems, not achievable using other transfer techniques. Using these three techniques, we transferred and demonstrated several devices, including waveguides, MMI couplers, PCW-TTD etc [1, 4, 5, 6]

Another important contribution of the Phase II program is the development of subwavelength grating (SWG) couplers that enable surface-normal coupling of light into SiNM waveguides. A conventional cleaving and polishing strategy for butt-coupling from a lensed fiber is extremely inefficient, since the success rate of cleaving and polishing on flexible substrates is poor. SWG enables coupling light from a single mode fiber, directly into the photonic waveguide, with exceptional coupling efficiencies. Moreover, our new design enables fabrication of efficient SWG couplers, simultaneously with photonic components, for the first time. We validated our design by fabricating couplers on an SOI wafer first [3]. We then extended the design for transferred SiNM devices. A high coupling efficiency of over 37.2% was demonstrated on transferred SiNM based devices [6]. Such a high coupling efficiency is not possible using conventional techniques.

We also worked on developing and demonstrating useful building blocks for use in the PAA system, such as compact photonic crystal waveguide true-time-delay lines, ultra-compact modulators, and printed antenna arrays. Conventional PCWs provide a very high dispersion close to the band edge. Band engineering can result in achieving high group index. We worked on the design in order to achieve high group index over a large bandwidth. The advantage of high group index over large bandwidth is that the performance of a modulator will be uniform over the entire bandwidth. By controlling the structural parameters, our design efforts yielded a high group index of 26.5 over 18nm bandwidth [7]. In order to couple light efficiently into these

waveguides, we also developed efficient PCW tapers. The design was used to develop a p-i-n modulator structure, and we demonstrated, for the first time, operation of such a PCW modulator at 2GHz [8]. We also implemented a 1x4 PCW TTD network consisting of 0mm, 1mm, 2mm, and 3mm long high dispersion PCW. We demonstrated a large time delay of 216pm via wavelength tuning [9, 10].

In terms of developing printed antenna elements that can be integrated together with SiNM based devices, we customized a high-rate R2R ink-jet printer in our lab, and demonstrated high-rate printing of antenna structures. For the printed antenna arrays, the far-field patterns were successfully measured.

These achievements lay a solid foundation for the development of communication systems, as well as other high-performance photonic and electronic components on flexible substrates, which is not possible using any other conventional techniques.

3. OBJECTIVES

3.1 Identification and Significance of the Problem or Opportunity

Over the last four decades, there has been tremendous progress in microelectronics industry owing to the development of rigid, flat, crystallographically nearly-perfect silicon. Silicon VLSI plays a key role in information technology today. Progress in silicon photonics over the last 15 years have also significantly moved conventional silicon VLSI to high speed, high bandwidth photonics with lower power consumption for switching and interconnects. Silicon photonics technology is compatible with Si CMOS fabrication processes and has become increasingly important for a myriad of applications [11-17]. Silicon based microelectronic, nano- and micro-photonic devices have the advantage of a compact structure with the potential for monolithic integration with optical-to-electrical on-chip conversion and detection [18].

Since 2001, there has been a growing interest in flexible electronic and photonic devices owing to their tremendous engineering importance [19]. So far, most of the flexible electronics/photonics research has been based on organic, polymer and amorphous semiconductor. One advantage of such a material system is that the devices can be formed using conventional ink-jet/screen printing techniques on low cost flexible substrates. Moreover, the circuits can be integrated on any platform, unlike the conventional silicon devices that can be integrated only on a wafer level. However, the device performance and speeds achievable are still inferior compared to single crystal semiconductor based devices. Therefore, single crystal nanomembranes (NMs) are being considered as practical alternatives for organic semiconductors for developing flexible microelectronic, nano- and micro-photonic devices. Such NM based devices are being widely considered for both military and civilian applications. These include Logic/Memory, Radio- Frequency Identification (RFID), Large Area Flexible Displays, Electronic Paper, Bio-Sensors, Large Area Conformal and Flexible Antennas, Smart and Interactive Textiles, Ubiquitous Sensor Networks (USN), Vehicle Clickers Readers, Real Time Locating Systems, Lighting, Photovoltaics etc.

Silicon nanomembranes (SiNMs) are very thin sheets of silicon that have been released from silicon-on-insulator (SOI) wafers and re-deposited on other rigid or flexible hosts such as glass, polyethylene teraphthalate (PET), Kapton etc using low temperature processes. Silicon nanomembranes (SiNMs) are processable like bulk Si and retain the electronic and optical properties of bulk Si.

	Conventional Electronic Devices	Conventional Optical Devices	Printed Electronic Devices	NM based Hybrid Optical and Electronic Devices
Speed	<40Gbps	>100Gbps	<1Gbps	>100Gbps
Cost	Expensive	Expensive	Cheap	Cheapest
Weight	Lower	Low	Least	Least
Substrate Choice Requirements	Rigid	Rigid	Any	Any
Conformal Large Area Circuits/Reliability	Difficult, Bulky and highly unreliable	Highly difficult and unreliable	Possible, Reliable	Possible, Reliable
Low Temperature Printing Technology	N/A	N/A	Usable	Usable
Electrical Signal Loss - Frequency Dependence	Linear	Constant	Linear	Low, Linear
System Applicability	High/Low end	High/Low end	Low end only	High/Low end
Integration density	Highest	High	Lowest	High
Fabrication Difficulty	Hard	Hard	Easy	Medium
Material Wastage	High	High	Low	Least

Table 3.1.1.1. Comparison among conventional electronic, optical, printed electronic and NM based hybrid optical and electronic device technologies. NM based devices share the performance advantages of all other technologies.

However, due to their thinness, their mechanical properties are interestingly different compared to bulk Si. For example, SiNMs are highly flexible in contrast to bulk Si and re-deposition on flexible substrates make the devices flexible, deformable, conformable and enabling dynamic manipulation, which is otherwise not possible to achieve using conventional Si fabrication technology. Thus, all manner of Si devices can potentially be fabricated, and high-volume manufacturing is feasible, thus utilizing and integrating the best features from different material systems. A comparison among the different technologies is presented in Table 3.1.1.1. It can be seen from the table that SiNM based hybrid electronic and photonic devices feature all of the advantages of bulk Si devices, in addition to demonstrating very good compatibility with flexible substrates, which cannot be achieved by either technology acting alone. Several unique electronic and photonic devices such as flexible modulators, conformal large-area photovoltaics, light sources, adaptive optics, etc, remain to be explored. By using nanomembranes, single-crystal materials with different crystal orientations or different compositions can be integrated for applications requiring stacking of hybrid layers that cannot be obtained by planar growth

techniques. Also, stackability permits access to three dimensional structures and devices with novel optoelectronic, photonic, or electronic properties [19].

Over the last few years, several interesting results showing unique electronic, optical and mechanical properties of this new disruptive technology have been demonstrated [20-26]. However, the technology is still in its infancy and there is not much of literature available on the development of different kinds of electronic and photonic devices or on addressing manufacturing and reliability issues. Part of efforts going on in the research community is also to address these concerns. Crystalline Si-based nanomembranes, not only suggest new and simpler paths to achieving unique system properties, but also extend the reach of Si into several unique areas which were once thought impossible to achieve.

Our system architecture, as shown in Fig. 3.1.1, consists of N stacked layers of SiNM based electronic and photonic devices on a single flexible Kapton polyimide substrate, which is one of the most popular materials used in printed circuit boards (PCBs). Such a conformal circuit can easily be integrated with a pilot's vest, helmet or with the aircraft body, and can provide various functionalities. For example, printed large area conformal solar cells on the top layer, made from ink-jet printing silicon nanoparticle nanofilm, can be used to power circuitry in various layers. Such large area coverage is difficult to achieve using conventional silicon solar cell fabrication technology.

It was our goal in this program to demonstrate manufacturable prototypes of several interesting SiNM based electronic and photonic devices and integrate them together with other necessary components in order to demonstrate a complete electronic-photonic system. As shown in Fig. 3.1.1, we envision one layer consisting of electronic control and another consisting of photonic control for an RF phased array antenna communication system. Other devices such as printed solar cells, active RFID etc can also be integrated for self powering and pilot identification, respectively. In general, one may think of a multilayer system wherein the different layers may contain different SiNM based electronic and photonic devices such as add/drop filters, device drivers, wavelength division multiplexers (WDMs) etc, that further enhance the capabilities of the overall system.

Using the SiNM based photonic and electronic components; a multitude of other devices can be developed. For example, along with the transmitting PAA system in the top layer, other RF devices such as solar powered active RFID tags can be fabricated, which can be used to determine the identity of the pilot and help in distinguishing between a friend or a foe. Using our technology, the possibilities of developing high performance flexible devices are endless.

The above system incorporates the innovative Si-nanomembrane PCW true-time delay lines, PCW modulators, RF amplifiers, fully printable FET switches, along with other printed components on a flexible substrate. The technology will provide a platform for integrating functional single crystal SiNM optical and electronic components and printed SiNM components on multiple layers for the first time.
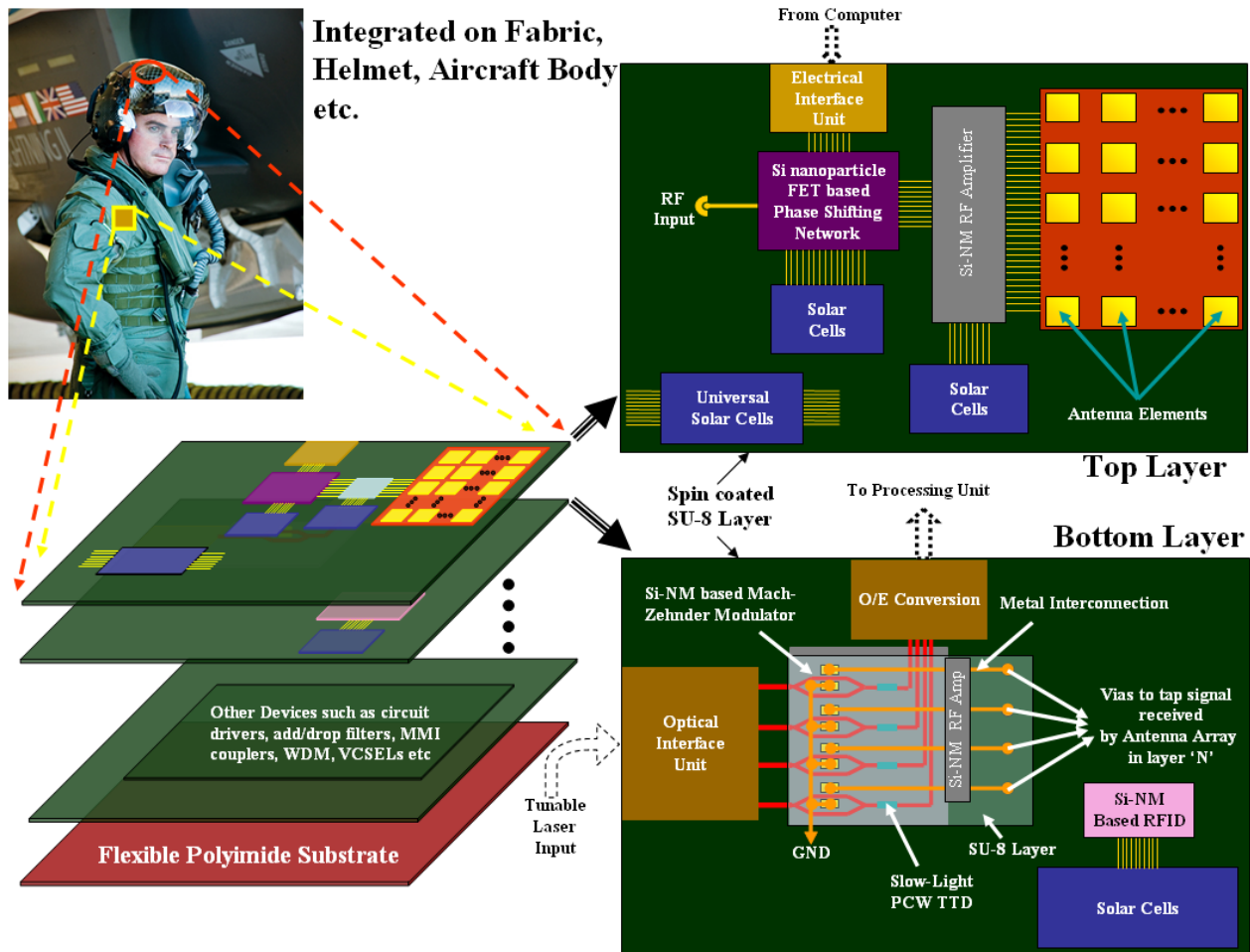
Fig. 3.1.1. Multi-layer system architecture on flexible substrate showing SiNM based microelectronic, nano- and micro-photonic components on different layers. System details of two layers consisting of SiNM devices to form a solar powered, bi-directional phased array antenna communication system are also shown. FET: Field-Effect Transistor; RFID: Radio-Frequency Identification; O/E: Optical-to-Electrical; PCW: Photonic Crystal Waveguide; TTD: True-Time-Delay.

3.2 Objectives for Phase II program

We had the following objectives for the Phase II program

1. Optimize the nanostructure of PCW-TTD lines to provide large time delay within a very short length of the waveguide.

2. Optimize the design parameters and fabrication process the phase shifting network.

3. Design and develop SiNM electro-optic modulator array that can effectively modulate the incoming RF signals onto an optical carrier.

4. Develop the proposed multi-layer system on flexible substrate. To achieve this, we need to:

   a. Further develop multilayer SiNM transfer process with tight alignment control.

b. Develop a multilayer metal interconnection scheme to route electrical signals between different layers.

c. Investigate advanced optical coupling techniques, including surface normal and planar coupling techniques, targeting at the best coupling efficiency through matching optical mode profiles as well as tapering the optical impedance to minimize the reflection loss.

d. Fabricate and test SiNM-based PCW modulator array and PCW-TTD array on flexible substrates, and evaluate their performance to finalize the optimized device structure.

e. Integrate the transferred NM devices together with other printed components such as Si nanoparticle FETs, antenna elements etc using multilayer NM transfer and interconnection techniques.

5. Address manufacturing and testing related issues such as input/output light coupling, reliability, fabrication yield, and optoelectronic integration; and produce a fully packaged prototype of bi-directional communication system on a flexible substrate that can be used for commercialization.

6. Explore several airborne applications of the nano- and micro-photonic and electronic SiNM devices on flexible substrates for U.S. Air Force missions, such as optically controlled PAA transceiver, conformal electronic circuits employing SiNM FETs, active RFIDs, EM wave sensors, solar cells etc, where the SiNM devices can show dominant advantages by eliminating the array of bulky conventional electronic and photonic components.

These objectives shall lay a solid foundation for the system demonstration and commercialization using the proposed SiNM based electronic and optical devices on flexible substrates and, potentially, the widespread presence of NM based nano- and micro-photonics and microelectronics technology in the market.

4. ACCOMPLISHMENTS/NEW FINDINGS

Through this Phase II program, we have achieved several important milestones that can form the basis for future systems. Our major accomplishments are:

1. Design of slow-light PCW and efficient tapers: Designed silicon nanomembrane based photonic crystal waveguide true-time-delay lines and investigated different taper structures for efficiently coupling light into the waveguides.

2. Design and demonstrating of True-Time-Delay (TTD) Lines: Designed efficient tapers for slow light photonic crystal waveguide true time delay lines and developed silicon nanomembrane based ultra compact photonic crystal waveguide true-time-delay lines. Developed a 1x4 TTD network consisting of 0, 1mm, 2mm and 3mm PCWs, and demonstrated large time delay up to

216ps via wavelength tuning. Also demonstrated high group index for SiNM based PCW-TTDs transferred on glass substrates.

3. Compact slot-light PCW based Electro-Optic Modulator: Designed photonic crystal waveguides that can provide high group index over a large bandwidth. The design provides high slow down factor of 0.31, which is the highest reported to date for a structure with a bottom cladding. We also developed an on-chip interferometer for accurately measuring the group index.

Using the designed PCWs, we developed an ultra low power, large bandwidth photonic crystal waveguide modulator. The modulator arms consisted of our designed band-engineered slow light photonic crystal waveguides of item # 2, which demonstrated a large group index of 26.5 over an 18 nm bandwidth. By embedding the photonic crystal waveguide in a PIN diode structure, modulation operation with a record-low $V\pi{\times}L$ of 0.0464 V.mm via carrier injection into an 80 μm long active section was experimentally demonstrated. The modulator $V\pi$ remains nearly constant over the low-dispersion slow-light bandwidth. Using the same structure, a maximum modulator operation up to 2GHz was also obtained.

4. SiNM Transfer Methods: We developed and demonstrated stamp printing of silicon nanomembrane based in-plane photonic devices onto a flexible substrate using a modified transfer printing method that utilizes a suspended configuration which can adjust the adhesion between the released silicon nanomembrane and the handle silicon wafer. With this method, 230 nm thick, 30μm wide, and up to 5.7 cm long silicon nanomembrane based waveguides are transferred to flexible Kapton films with >90% transfer yield. The propagation loss of the transferred waveguides are measured to be ~1.1 dB/cm. Scalability of this approach to transfer intricate structures such as photonic crystal waveguides and multimode interference couplers with minimum feature size of 200 nm and 2μm, respectively is also demonstrated.

We also developed a low temperature nanomembrane transfer technique based on adhesive bonding and deep reactive ion etching, using which a large area (2 cm × 2 cm), 250 nm thick defect-free SiNM can be transferred onto other substrates such as Kapton, Glass etc. We fabricated a 1×16 power splitter, consisting of two cascaded levels of 1×4 MMIs. An output uniformity of 0.96dB at 1545.6nm across all channels, and insertion loss of 0.56 dB is experimentally demonstrated.

5. Efficient Coupling of Light into SiNM Waveguides: We developed surface normal grating couplers utilizing subwavelength structures. Our subwavelength grating (SWG) couplers do not complicate the fabrication process, and the devices and SWG can be fabricated in a single step. Using the developed SWG, we demonstrated high coupling efficiency of 37.2% into transferred SiNM waveguides.

6. SiNM Devices on Unusual Substrates: We transferred SiNM and demonstrated operation of photonic devices, such as MMI, waveguides, PCW, ring resonators on glass, Kapton etc. For the PCW TTD, high group index of 28.5 is demonstrated.

7. Ink-Jet Printing of Antenna Array: We developed short channel TFTs using printing. We also developed 1x4 PAA using continuous high-rate ink-jet printing, and demonstrated beam steering from the fabricated conformal PAA systems.

The following sections describe the work performed during Phase II in greater detail.

4.1 Silicon Nanomembrane Based True Time Delay Lines

4.1.1 Design of efficient tapers for slow light photonic crystal waveguides

We first designed efficient tapers in order to couple light efficiently into the PCW. A schematic of a PCW is shown in Fig. 4.1.1.1(a). The photonic crystal is a hexagonal lattice of air holes (red) in silicon slab (grey). In order to engineer the band structure of the PCW, we tuned 4 parameters. We tuned the size of the gap (*g*) between the two innermost rows, which without any change is $a\sqrt{3}$, where *a* is the lattice constant. For a tuned structure, *g* is given as $(1+dW)a\sqrt{3}$. dW is the fractional change in the normal width (W) of the defect waveguide, given as $W = a\sqrt{3}$.
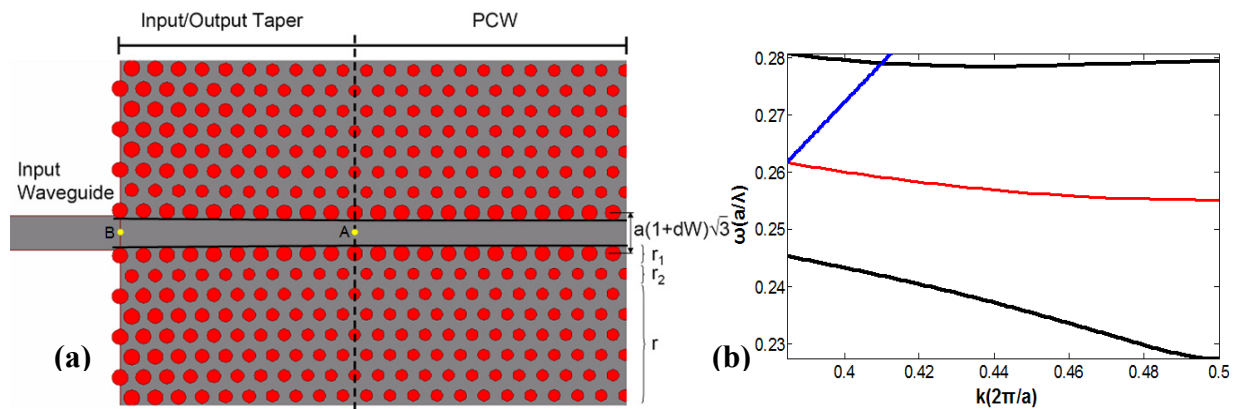

Fig. 4.1(a) A schematic of the band-engineered PCW structure and the input/output coupling taper structure. The design parameters (r₁, r₂, r₃ and dW) are shown. The input and output tapered PCW couplers are mirror images of each other in the actual implementation, (b) Band structure of the optimized photonic crystal waveguide (red). The blue and black lines show the light line (n=1.45) and the band gap edges, respectively

We also tuned the radii of the hole in the inner rows (r_1), the second inner row (r_2) and all other rows (*r*) as shown in Fig. 4.1.1.1(a). In order to prevent high total losses, in addition to minimizing the fabrication errors, also designed an efficient adiabatic taper structure for the 3D geometry by gradually reducing the high index of PCW band to a value close to that of the input/output dielectric waveguide. Note that the structure holds its inversion symmetry with respect to the PCW gap. By changing *dW*, r_1, r_2 and *r*, we optimized the band structure for highly dispersive applications by minimizing the total propagation loss. We used BandSolve™ to simulate the PCW band structure for *r*=0.262*a*, r_1=0.338*a*, r_2=0.202*a*, and *dW*=0 as shown in Fig. 4.1.1.1(b).

For these adiabatic tapers, the operating principle relies simply on reducing the light reflectance $|R|$ at discontinuities based on the effective medium approximation $|R| = \dfrac{(n_{g1} - n_{g2})^2}{(n_{g1} + n_{g2})^2}$, where n_{g1}

and n_{g2} are group indices of the two PCWs at either side of the discontinuity. However, using this relation in the case of hexagonal lattices (with air holes), which is the most common on-chip structure for PCWs, leads to significant underestimation of the coupling efficiency values reported before (e.g., ng1 = 5, ng2 =100, T =1–R=80% [27]. McPhedran et al argued that the high transmission is due to the excitation of an evanescent mode on the high n_g side of the interface [28]. The evanescent mode has amplitude comparable to that of the fundamental propagating mode, and its phase is such that it results in a small total field at the interface with the low ng PCW to satisfy the boundary conditions. Away from the interface, however, the evanescent mode decays and the total field amplitude increases to its maximum. Note that the final field amplitude in the high ng PCW is much larger than that in the low n_g PCW due the slow down effect. In the Phase II work, we compare the effect of evanescent modes and group index tapering on the total coupling efficiency from a strip waveguide to a high ng PCW. We numerically investigated the effect of PCW taper with different lengths and tapering profiles, including a step profile.

A schematic of the strip waveguide to high n_g PCW structure with an intermediate low n_g PCW coupling structure is shown in Fig. 4.1.1.2.
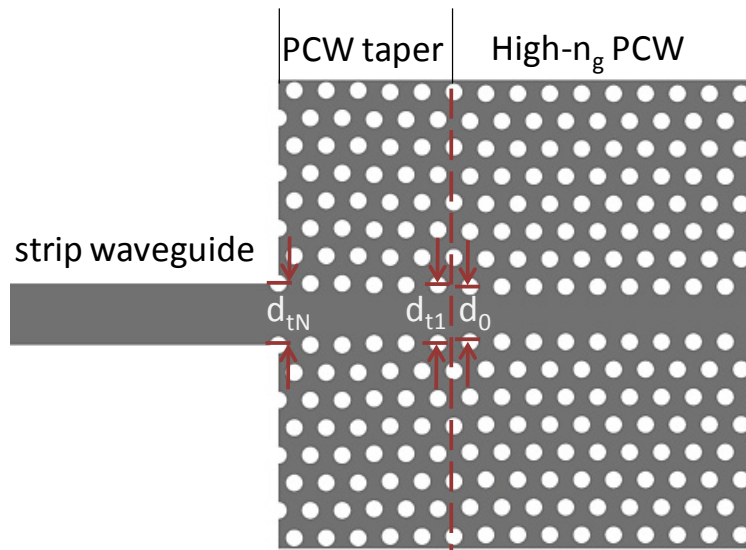

Fig. 4.1.1.2. A schematic of the strip waveguide to high group index photonic crystal waveguide coupling structure. The PCW on the right side of the interface is assumed to support high n_g propagation at the wavelength of operation.

The high n_g PCW is a W1.0 PCW ($d_0 = a\sqrt{3}$), where a=395nm is the lattice constant. Hole radii for both the PCWs is the same, r=0.26a. The width of the line defect in the PCW taper changes from d_{t1} [chosen as $a(\sqrt{3}+0.2)$] at the interface with the strip waveguide to d_{tN} [assumed as $a(\sqrt{3}+0.2)$] at the interface with the high n_g PCW, where N is the number of periods in the PCW taper. A Silicon-on-Insulator (SOI) with silicon device layer thickness of 230nm is used. In the case of a step taper, the line defect width is constant throughout the taper, also d_{t1}= d_{tN}. In the case of adiabatic tapers, d_i values assume either a linear or a parabolic from d_0 to d_{tN}. In the case

of split tapers, $d_1 = ... = d_{N/2} = a(\sqrt{3}+0.1)$ and $d_{N/2+1} = ... = d_N = a(\sqrt{3}+0.2)$. Note that the step taper is the same as the hetero-group velocity PCWs investigated in [29], with the difference that we consider much shorter low n_g PCW taper (N≤16, PCW taper length <7μm). Note that all the holes have the same radius in the high n_g PCW and the PCW taper. This scheme is more suitable for implementation those schemes in which there are different hole sizes in the design [30].

In order to calculate the group index, we simulate the PCW band structure using 3D Plane Wave Expansion (PWE) method. Fig. 4.1.1.3(a) shows the band structure for a W1 PCW. Fig. 4.1.1.3(b) depicts variations of group index as a function of wavelength for PCWs with various line defect widths. As shown in this Figure, gradual increase in the line defect width can be used for adiabatic tapering for the group index based on the same technique used in [31-33]. As shown in Fig. 4.1.1.3(b), further widening the line defect width [more than $a(\sqrt{3}+0.2)$] does not significantly reduce the group index in the bandwidth of interest (20<n_g<100).

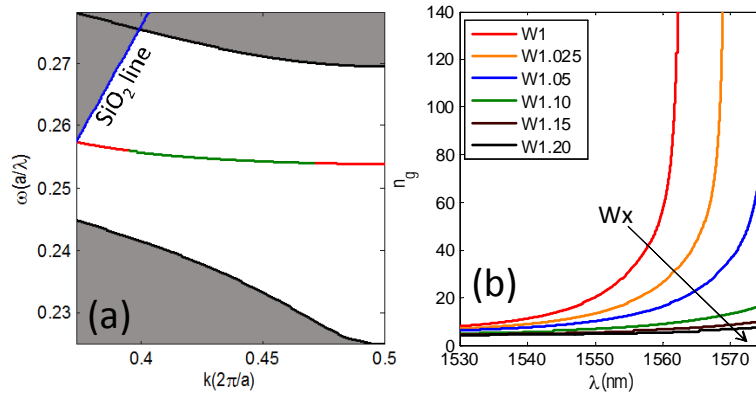Fig 4.1.1.3. (a) Band structure for W1 PCW, r=0.26a, slab thickness=230nm, n(SiO₂)=1.45, n(Si)=3.47. Green section is the bandwidth over which the 20<n_g<100. (b) Group index vs. wavelength for infinitely long PCW with different defect line width.

We use 3D Finite Difference Time Domain (FDTD) simulations to calculate the coupling efficiency. In order to isolate the effect of the PCW taper from the Fabry Perot oscillations due to reflection at the input and output ports, we only simulate one port (one strip waveguide-PCW taper- high n_g PCW). In the FDTD simulations, 12 periods of the high n_g PCW are used. We simulate the transmission spectra for step, linear, parabolic and split tapers for N=4, 8 and 16, as shown in Fig. 4.1.1.4. We observe that for any number of periods, the step taper results in highest transmission almost throughout the slow light region. As the number of periods in the taper increases or as the group index increases, all the taper types result in similar performance. Interestingly, the linear taper and the step taper show similar behavior in the slow light region for all N values. For N=16, when n_g>80, both linear and split tapers show a slightly better performance (~with 5%) compared to the step taper. For N=16, very close to the band edge (λ=1562.5nm), the parabolic taper outperforms the step taper. Back scattering losses in PCWs increase as n_g^2. However, both adiabatically increasing group index in a chirped PCW on SOI substrate [34] and the transmission spectrum of GaAs PCW membranes [35] have shown that the disorder-induced scattering completely disrupt transmission for n_g>30. Therefore, for PCW based

slow-light devices, in the range of power-law governed transmission, the step taper outperforms the adiabatically and split tapered ones. From the 3D FDTD simulation results we found that step tapering for a small number for periods in the taper ($N<8$) has the highest coupling efficiency. The adiabatic tapers only outperform the step taper at n_g values not supported by current state of art fabrication technology, and only at longer tapers. So, we can conclude that the effect of the evanescent mode in coupling between low n_g and high n_g PCW is more dominant than the effect of the group index tapering in practical compact devices.
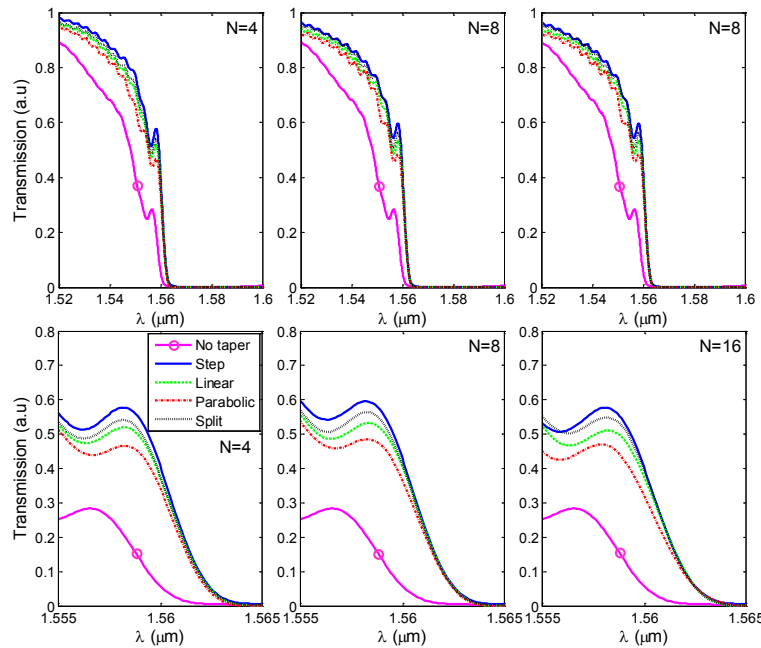

Fig 4.1.1.4 3D FDTD simulation results for direct coupling of strip waveguide and PC slab waveguide (no taper) and coupling through PCW tapers, with step, linear, parabolic and split profiles, for N=4, 8 and 16. The lower row graphs were zoomed at the band-edge region.

4.1.2 Fabrication and Testing of Efficient Tapers for Photonic Crystal Waveguide

In order to confirm the above claim, we fabricated PCWs on SOI (SOITEC) with a 250nm top silicon layer and a 3µm buried oxide layer with different types of taper structures. A 50nm oxide layer was thermally grown as an etching mask, consuming 20nm silicon. The length of the high n_g PCW section is 100µm in order to suppress the Fabry-Perot effect on the transmission. The pattern was transferred to the SOI through JEOL JBX6000 electron beam lithography system, followed by the reactive ion etching. SEM pictures of fabricated devices are shown in Fig. 4.1.2.1.

The photonic crystal waveguide was tested on a Newport six-axis auto-aligning station. The light from a broadband amplified spontaneous emission (ASE) source (Thorlab ASE-FL7002), covering 1520~1620 nm, was TE-polarized with an extinction ratio of over 20dB and butt coupled into/out through a polarization maintaining lensed fiber with a mode diameter of 2.5µm. Transmitted light was analyzed by an optical spectrum analyzer (ANDO AQ6317B) with 0.05
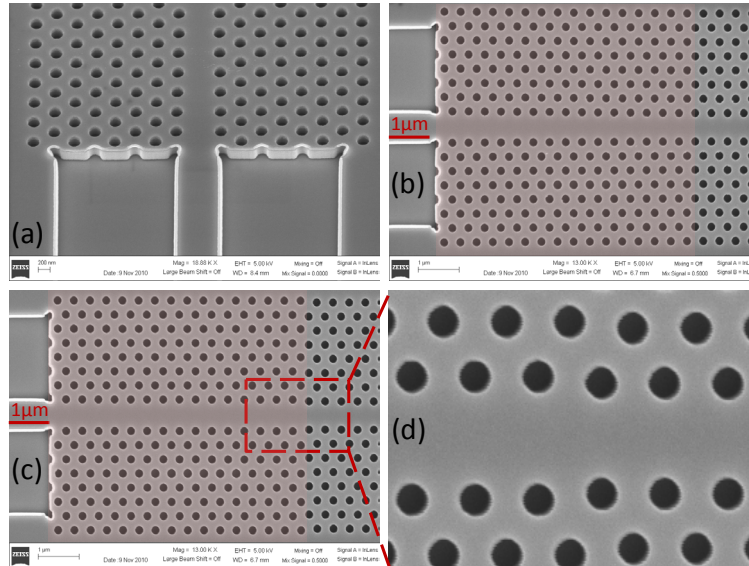
Fig. 4.1.2.1 SEM picture of fabrication PCWs butt coupled to strip waveguides, (a) a tilted view showing the silicon slab PCW, (b) 16-period linear taper, (c) 16-period step taper, and (d) interface of step taper (left) with high n_g PCW (right). (please show left and right in the figure)

nm resolution. Fig. 4.1.2.2 shows the transmission spectra of direct coupling between strip waveguide and PCW, and also coupling through step and linear PCW tapers with 8 and 16 periods. The oscillation amplitude for the direct coupling is 6dB (full swing), while it is about 3dB for coupling with either step or linear tapers, N=8 and 16. The transmission spectra are blue-shifted by about 20nms, which is due to 15nm expansion in the hole size. Similar to the 3D FDTD results, the step tapers slightly outperform the linear tapers in both N=8 and 16 cases. Also, as the N increases, the performance of the step and linear taper converge together.
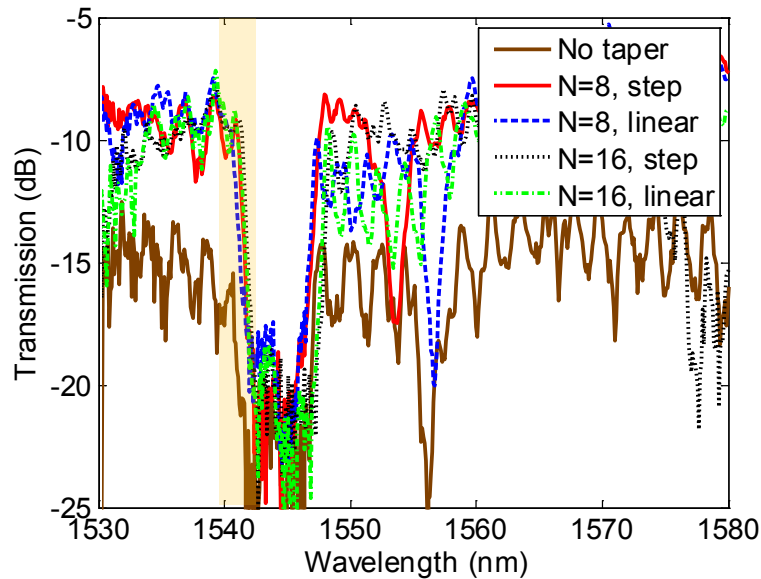

Fig. 4.1.2.2. Measurement results, transmission vs. wavelength for direct coupling of strip waveguide and PC slab waveguide (no taper) and coupling through PCW tapers, with step and linear profiles, for N=8 and 16. The near band-edge wavelength (slow light region is highlighted).

Therefore, by comparing the effect of different PCW taper profiles on transmission in the slow light region, we tried to find whether group index tapering or existence of evanescent modes at the boundary of a low n_g and a high n_g PCW has a dominant role in enhancing light coupling between strip waveguide and a PCW operating in the slow-light region. Numerical analysis and experimental measurements showed that the use of short low n_g PCW as an intermediate coupler, in which group index tapering is absent, is advantageous over adiabatically tapered PCW coupler. Our results also indicate that for an efficient coupling, a low n_g PCW coupler much shorter than previously demonstrated is sufficient.

4.1.3 Photonic Crystal Waveguide Based Compact True-Time-Delay Lines

The micrograph of the PCW TTD module is shown in Fig. 4.1.3.1(a). The optical input power is uniformly divided into four channels using a 1x4 multimode interference (MMI) beam splitter, which has a width and length of 16μm and 117.7μm, respectively. The input and output access waveguides widths are 2.5μm on a 230 nm silicon nanomembrane on a silicon-on-insulator (SOI) wafer, which has been optimized for high MMI performance. The FIMMPROP Eigenmode decomposition based simulation result of TE polarized light propagation inside the MMI at λ=1.55μm is shown in Fig. 4.1.3.2(a). Each channel consists of carefully chosen lengths of silicon strip waveguides and PCWs[11], such that at any given wavelength within the bandwidth of interest, a constant time delay difference is setup between adjacent channels. Channel-1 contains a 5mm-long silicon strip waveguide and no PCW, and is chosen as a reference line.
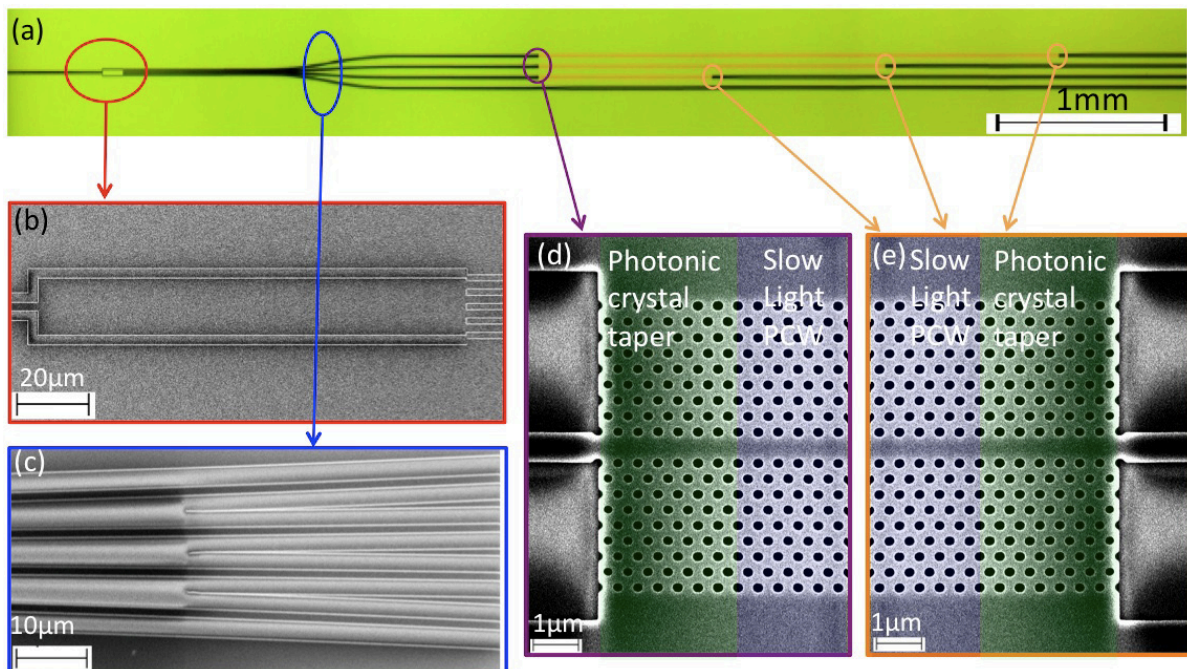

Fig. 4.1.3.1(a) Microscope picture of the TTD beamformer based on a 1x4 MMI and PCWs. (b) SEM picture of the enlarged view of the 1x4 MMI power splitter. (c) Enlarged view of the S-bends that increase the waveguide separations. (d) and (e) SEM pictures of the PCW region containing photonic crystal taper and slow light PCW region [9].

Channels-2, 3, and 4 contain 4mm, 3mm, and 2mm silicon strip waveguides and 1mm, 2mm, and 3mm-long PCWs, respectively, with identical PCW parameters. When the operating wavelength λ is tuned, this configuration creates proportional relative time delay 0, τ, 2τ, and 3τ in channels-1~4, respectively. Note that since a different τ_i time delay difference is achieved for different tuning wavelength λ_i, the time delay profiles can provide appropriate phase distribution at the output for operation in a PAA. Scanning electron micrographs of the 1x4 MMI and the waveguide splitting section for four channels are shown in Fig. 4.1.3.1 (b) and (c), respectively. The enlarged view of the slow light PCWs and the PCW taper regions are shown in Figs. 4.1.3.1 (d) and (e), respectively [9].
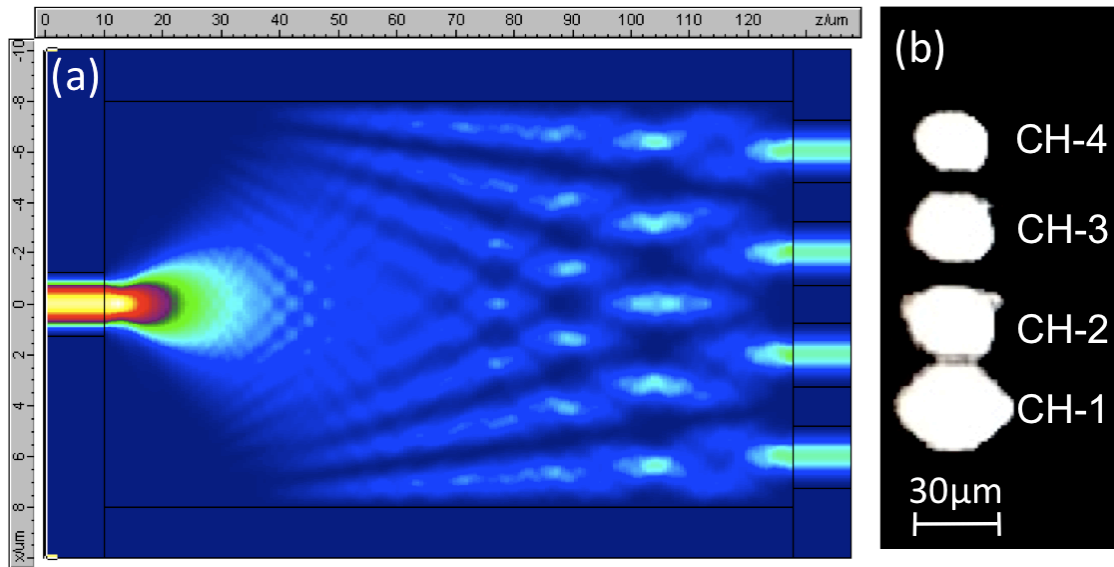

Fig. 4.1.3.2(a) Simulation of the field profile of a 1x4 MMI (b) MMI output at 1550nm imaged by top view IR camera [9]

In our design, the lattice constant (a), hole diameter (d), and slab thickness (h) of the W1 PCWs are chosen as 405nm, 190nm, and 230nm, respectively so that the PCWs support a guided mode covering 1533~1573nm. To minimize the coupling loss into the slow light PCW, we utilize two photonic crystal tapers at the strip-PCW interfaces. These structures significantly improve the matching of the two different waveguide modes and reduce coupling loss. Such a design enables operation in the high-group index region near the band-edge, which gives much larger delay time and faster tuning based on wavelength tuning.

The on-chip TTD module is fabricated on a Unibond SOI wafer with a 250 nm top silicon layer and a 3μm buried oxide (BOX) layer. First, a 45 nm of thermal oxide is thermally grown as an etching mask for pattern transfer. Then, MMI power splitter, PCWs, photonic crystal tapers, and strip waveguides are patterned in one step with a JEOL JBX-6000FS electron-beam lithography system followed by reactive ion etching.

The TTD module is tested on a Newport 8-axis precision automated alignment station, which has a 10nm horizontal alignment accuracy and 5nm vertical alignment accuracy. In order to measure the output characteristics of the fabricated device, light from a broadband laser source is TE polarized and coupled to the TTD module through a polarization maintaining lensed fiber. The output signal from the TTD module is collected using single mode lensed fibers. The output power uniformity of the 1x4 MMI splitter is characterized first. The infrared (IR) image of the 1x4 MMI output at 1550nm taken using a top down IR camera is shown in Fig. 4.1.3.2 (b). According to the measurement data, the power fluctuation of the 1x4 MMI is within 8%, which is reasonable given the fabrication tolerance.

Transmission spectra of the channels containing PCWs were also characterized to identify the transmission bands of the PCWs experimentally. Note that the measurement data were taken from integrated devices, i.e. the transmission through MMI and PCWs. Transmission spectra for channel-2~4are shown in Fig. 4.1.3.3, which clearly show overlapping transmission bands from 1533nm to 1573nm.Each set of data is composed of 1200 data points to ensure good accuracy, and the results for each of the channels from 2~4 were normalized to the transmission of the strip waveguide channel. The coupling loss of PCWs is significantly reduced due to the implementation of PCW tapers. The highest transmission point is -2.68dB for channel-2, which contains 1mm long PCW [9]. The increasingly large fluctuation in the transmission spectra for longer PCWs channels are mainly due to the propagation loss from the fabrication related imperfections in the PCWs.
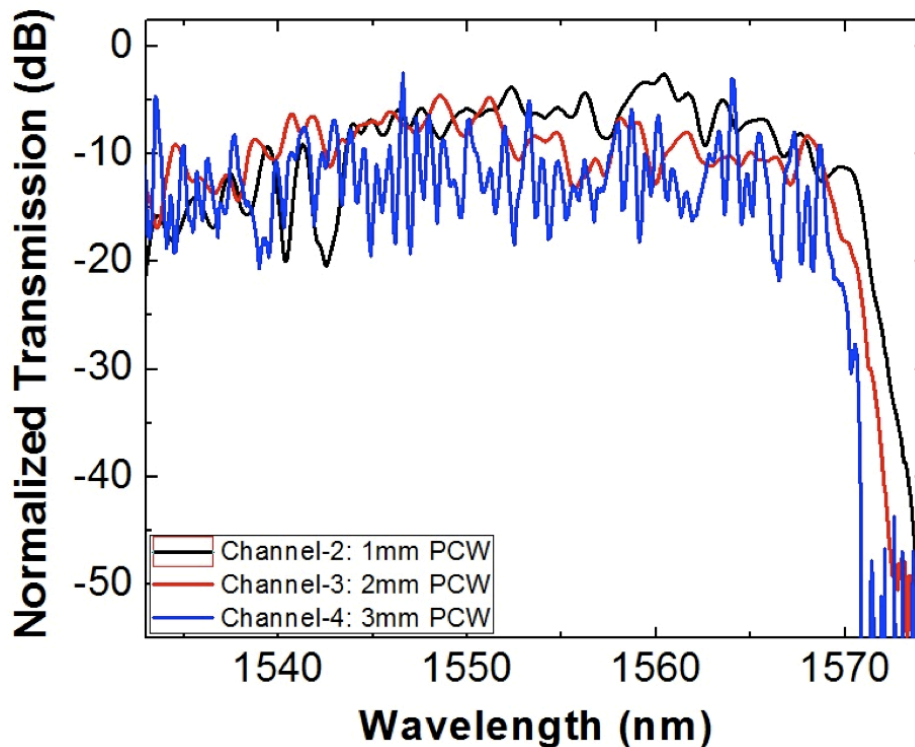

Fig. 4.1.3.3 Transmission spectra of the channels containing 1~3mm PCWs [9].

The schematic of the measurement setup is shown in Fig. 4.1.3.4 (a). In order to measure the time delay from the TTD lines, a X-band (8-12GHz) RF signal from an HP8510C vector network analyzer (VNA) is modulated onto an optical carrier from a tunable continuous wave laser by a LiNbO$_3$ modulator. The output of the modulator is coupled to the on-chip TTD module using the same method used to characterize the transmission spectra of TTD channels. A photodetector (PD) covering the X-band frequency range is used to convert the modulated optical signal to an electrical signal, which is then amplified using an X-band RF amplifier and fed back to the network analyzer. The phase vs. frequency relationship of all the channels is measured on the network analyzer. Due to the strong fluctuation in transmission spectra below 1545nm and above 1572nm, time delay measurements were only performed between 1545nm and 1572nm to avoid strong optical loss. The measurement results are shown in Fig. 4.1.3.4 (b)~(d). The phase-frequency results are normalized to the strip waveguide channel (channel-1) using VNA to show the relative phase change. Highly linear phase-frequency relation is seen in all the channels,
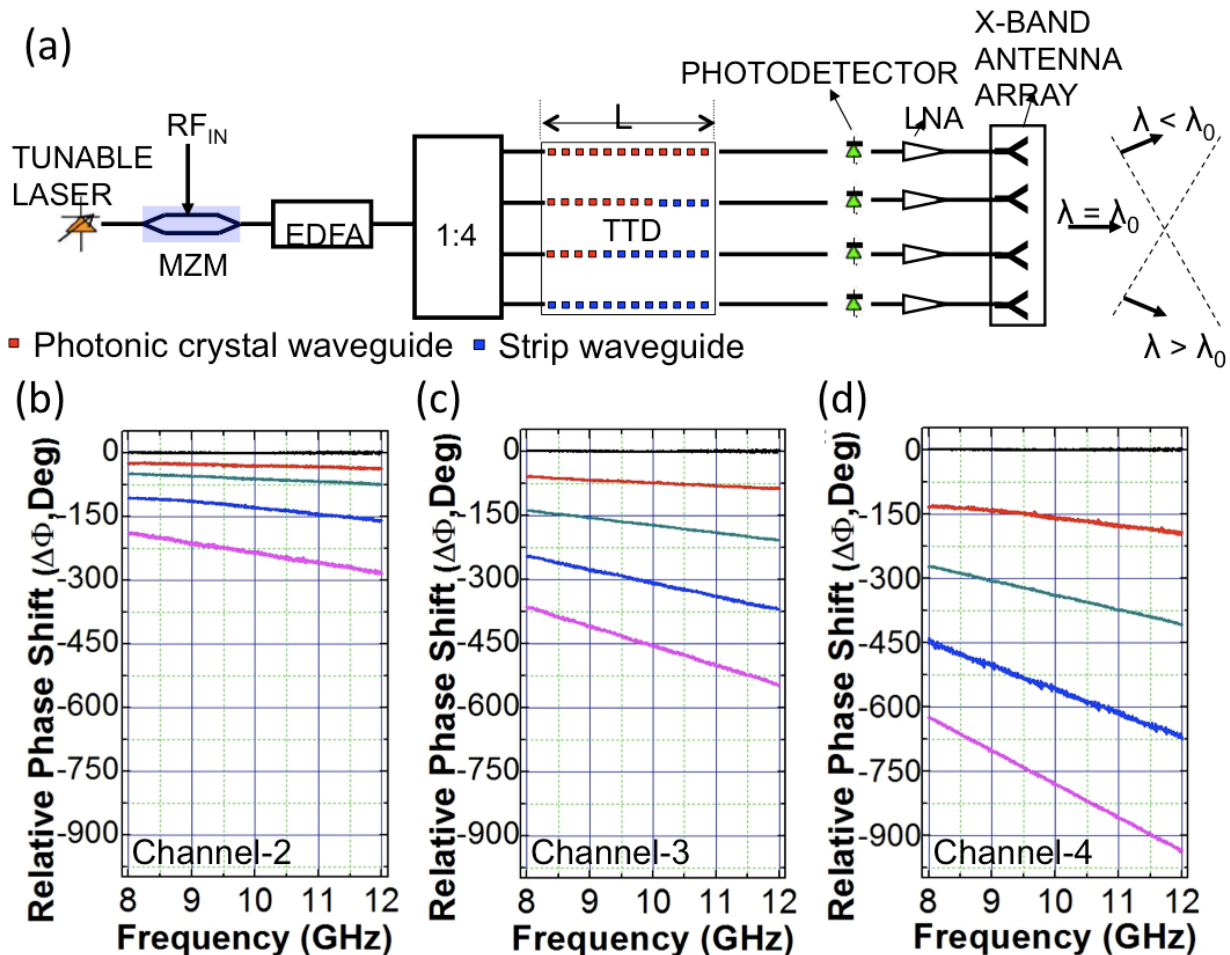

Fig. 4.1.3.4(a)A schematic of the measurement setup of a PCW-based TTD module. Measurement results of phase vs. frequency relation for (b) channel-2, (c) channel-3, and (d) channel-4. Measurement results were normalized to the strip waveguide (channel-1). The horizontal line (black) in (b), (c), and (d) represents the normalized phase shift of channel-1 [9].

which clearly shows the signature of true time delay. This characteristic is critical to have a wide band phased array antenna without beam squint effect covering the whole X-band (8 to 12.5 GHz). The time delay (τ) in the PCWs is derived from a linear regression fit following the relation $\tau = \Delta\Phi/\Delta\omega$, where $\Delta\Phi$ represents the changes of phase in the measurement frequency range $\Delta\omega$. Accordingly, the maximum time delays obtained are 64.96ps, 126.31ps, and 216.66ps for channels-2, 3, and 4, respectively. The wavelength-tunable time delay results are summarized in Fig. 4.1.3.5.
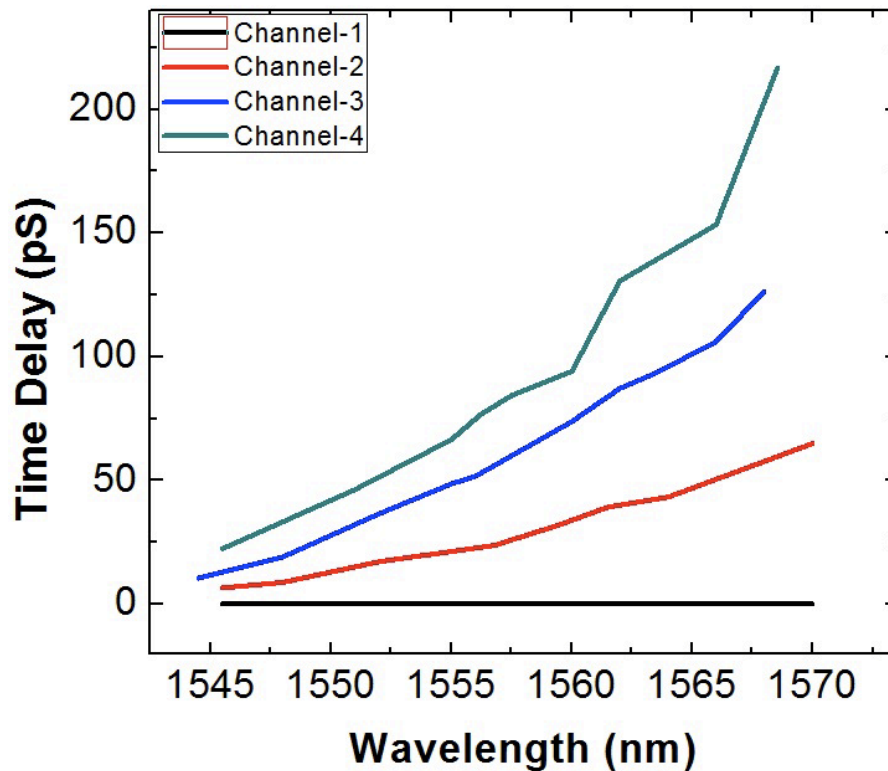

Fig. 4.1.3.5 Wavelength-Tunable Time Delay for all four channels[9]

When external tunable delay lines are used to offset the time delay difference between adjacent delay lines, this TTD module can provide a steering angle from -44.34 degree to 44.34 degree if wavelength is tuned from a central wavelength λ_0=1558.5nm for an X-Band PAA with inter-element spacing of 1.25cm. Thus, we have achieved the first on-chip compact TTD lines utilizing photonic crystal waveguides.

4.2. Silicon Nanomembrane Band-Engineered Photonic Crystal Waveguide Modulator

4.2.1. Design of Band Engineered Photonic Crystal Waveguide with Large Slow-Down Factor

In the previous sections, we presented the design of slow light photonic crystal waveguides for true time delay lines. In this section, we will present the design of a band-engineered photonic crystal waveguide that can be used for achieving a broadband modulator. As will be shown, this structure also exhibits the highest slow down factor (SF), which is the normalized bandwidth -

group index product, as high as 0.31 that has been reported to date for oxide cladded silicon-nanomembrane based PCWs. A lattice-shifting based design is utilized for achieving low-dispersion slow-light SOI PCW [7, 8].

A schematic of the band engineered PCW is shown in Fig. 4.2.1.1. The lattice constant (a) is 392nm. The thickness of the silicon layer and the buried oxide layers are 250nm and 3μm, respectively. Band engineering can be done by tuning the hole sizes [36] or the positions of the rows adjacent to the line defect. However, lattice shifting is more desirable as it has proved to be a fabrication friendly approach [37], while the accurate control of several different hole sizes is a challenging task. Two different approaches of lattice shifting, longitudinal (parallel to the defect line) and lateral (perpendicular to the defect line), are shown in Fig. 4.2.1.1. A slow-down factor as high as 0.3 was demonstrated for an air-bridged PCW band-engineered by lateral lattice shifting [38]. Thus far, the highest experimentally determined SF for a PCW band-engineered by longitudinal lattice shifting has been 0.19 [39]. Theoretically however, SF as large as 0.35 is estimated by longitudinal lattice shifting of the two innermost rows [40].
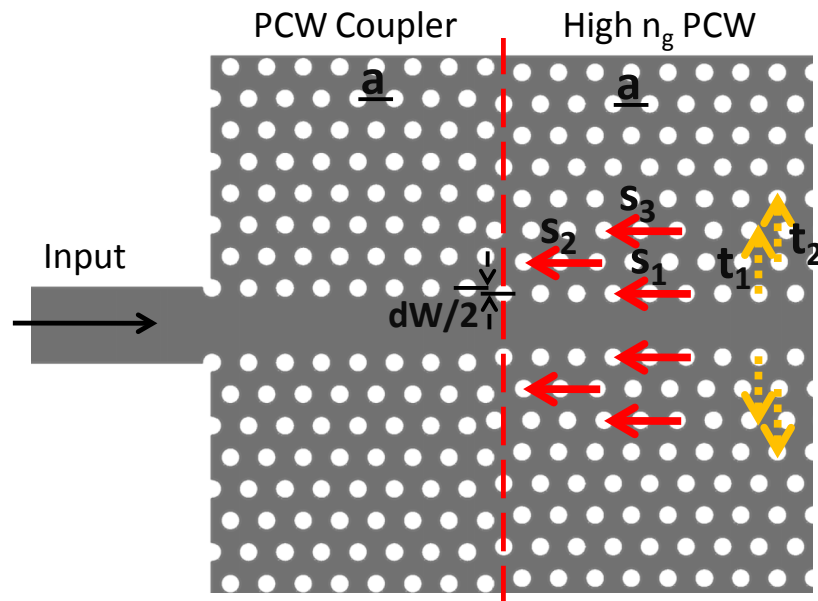

Fig. 4.2.1.1 Schematic of band engineered PCW, along with PCW taper. Longitudinal (parallel to the defect line) and lateral (perpendicular to the defect line) lattice shifting are depicted by red (solid) and yellow (dashed) arrows, respectively. The direction of the arrows indicate the positive direction assumed in this paper.

We performed simulations using RSoft 3D BandSolveTM. Figs. 4.2.1.2(a) and (b) show the effect of longitudinal and lateral lattice shifting, respectively, on the band structure. An important observation is that longitudinal lattice shifting does not change the position of fundamental PCW defect mode in the fast light region. In the case of lateral lattice shifting, for a large SF value, a large positive value of t_1 is necessary [38] that effectively increases the defect line width (dW), and thus causes red shift in the defect mode band. Therefore, for our design, we chose the longitudinal lattice shifting of the first three rows on the two sides of the defect mode. As will be discussed later, this choice also helps in the design of the input/output coupler. For design

optimization process, we utilized sequential quadratic programming (SQP), a nonlinear programming technique that exploits the gradients of the objective and constraint functions at each iteration to accelerate convergence [41]. The independent variables are s_1, s_2, s_3 and r, where s_i (i = 1, 2, 3)-represents the amount of lateral shifting for the ith row of air holes, and r is the hole radius. Similar to the results presented in [40], we found that a large longitudinal shift of the innermost rows results in a minimum in the defect mode dispersion curve below the silica light line and at normalized k<0.5 [Fig. 4.2.1.2(a)]. Although the resulting SF can be large, using FDTD, we found that coupling into the desired section of the defect mode band in such PCWs is inefficient (typically, maximum normalized transmission <15%). In contrast, in the case of band engineered PCWs, with their defect mode minimum at the band-edge (k=0.5), normalized transmission over the low-dispersion bandwidth can reach 50% without any couplers [Fig. 4.2.1.2(d)]. Thus, another constraint in the optimization process is to keep the defect mode minimum at the band-edge. Fig. 4.2.1.2(c) shows the band structure of the designed band-engineered low-dispersion slow light PCW (r=0.27a, s_1=0, s_2=-0.05a and s_3=0.25a) with n_g=26.7 ± 10% over a bandwidth of 18nm, corresponding to SF of 0.31. Note that the second and third rows are shifted in opposite directions.
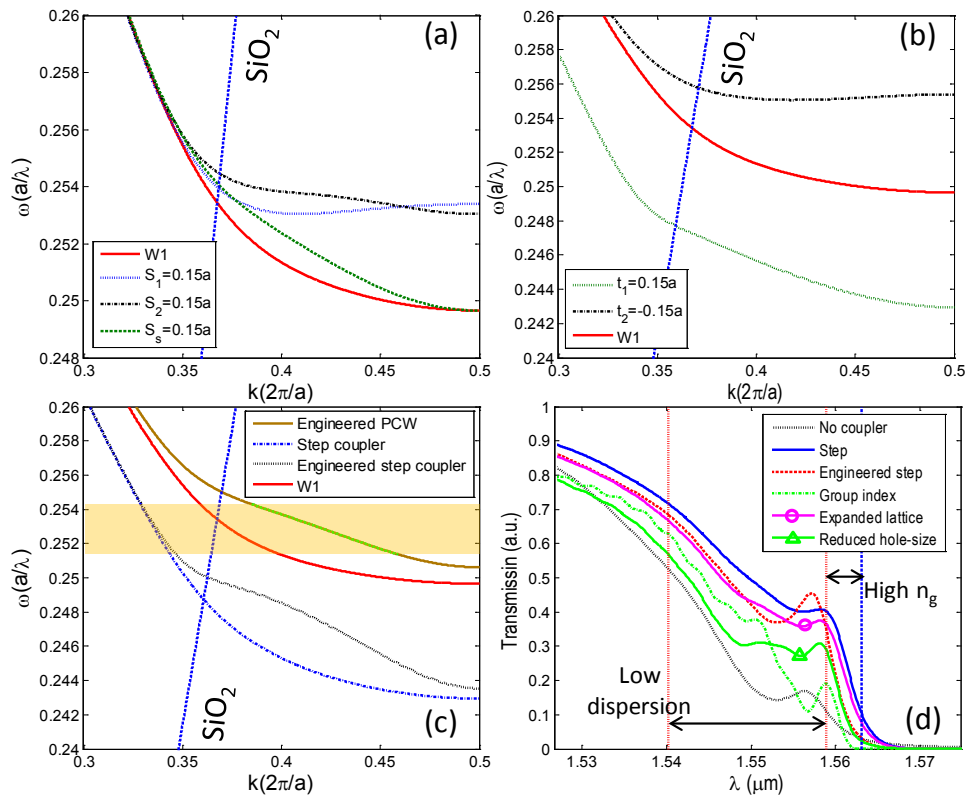

Fig. 4.2.1.2 PWC band structures with (a) 0.15a longitudinal lattice shifting, (b) 0.15a lateral lattice shifting. (c) Band structures of the designed band-engineered PCW, dW=0, s_1=0, s_2=-0.05a, s_3=0.25a, step coupler (r=0.27a, dW=0.15a, s_1=s_2= s_3=0), and an engineered step coupler (r=0.27a, dW=0.15a, s_1=0, s_2=-0.05a, s_3=0.25a). (d) FDTD simulations of a single interface between different fast-light PCW and the designed band-engineered PCW. In all cases, the coupler (or taper) length is 8 periods.

An important consideration for practical applications is efficient coupling into the slow-light region from an access ridge waveguide. Coupling efficiency can be improved by inserting a group index taper [33, 42] or a fast light PCW region between the access ridge waveguide and the PCW [38, 44-46]. In principle, the performance (transmission efficiency) of the group index tapers scale badly with increasing group index, while the existence of evanescent modes at the interface in fast light PCW couplers helps satisfy the boundary conditions [44], thus improving coupling efficiency. Numerical and experimental investigation also revealed that even at group index $n_g<30$, a step coupler, which is a special implementation for the fast light PCW region, outperformed group index tapers realized by the defect mode width modulation [44].   In comparison to the slow light PCW, a fast light PCW coupler defect mode is red-shifted so that the steep section of its defect mode overlaps with the desired bandwidth of the slow light PCW. This can be realized in different ways, such as by reducing the hole sizes while retaining the original lattice constant [46], expanding the hole spacing while retaining the same hole size, and by increasing the defect mode width (also known as the step coupler) while retaining all the other parameters the same [44].

The step coupler presented in [44] was designed for efficient coupling into a W1 PCW. An increase in the defect line width red-shifts the defect mode band, and thus, its low-group index overlaps with the bandwidth of interest. 3D FDTD simulations show that increasing the defect line width more than about 0.15a-0.20a results in diminishing returns. However, a question to be answered is whether the fast light PCW designed to couple light into band engineered PCW should itself be band engineered. In other words, how the values of s_1, s_2 and s_3 must be chosen? Fig. 4.2.1.2(c) shows the band structures of a non-engineered PCW step coupler (r=0.27a, dW=0.15a, $s_1=s_2=s_3=0$) and an engineered PCW step coupler (r=0.27a, dW=0.15a, $s_1=0$, $s_2=$-0.05a and $s_3=0.25a$). From the figure, one notices that the non-engineered coupler has a more consistent slope inside the low-dispersion bandwidth. Another important observation is that the usable part of the band in the case of a step coupler lies slightly above the silica light line, however, both numerical and experimental results show that the silica bottom cladding does cause negligible radiation loss for a small number of periods (less than 16) [44]. The same phenomenon was also observed in the case of the group index coupler [33]. We believe that as long as the holes are not filled with silica, the effective light line lies between that of air and silica, and specifically, the radiation loss can be ignored for small number of periods.

In order to numerically investigate the efficiencies of different couplers, we simulated transmission through a structure consisting of a ridge silicon waveguide, 8 periods of a fast light region and 13 periods of the designed engineered PCW (dW=0, $s_1=0$, $s_2=$-0.05a and $s_3=0.25a$) using RSoft 3D FDTD. Note that step couplers with longer than 8 periods do not further improve the transmission efficiency for group indices lower than 30 [44]. The length of the slow light section was chosen as 13 so that the transmission spectrum becomes independent from the number of periods.

For the sake of comparison, we also simulated a structure only consisting of a ridge silicon waveguide and 13 periods of the designed engineered PCW with no coupler. Fig. 4.2.1.2(d) compares the normalized transmission of several different couplers against the case in which no coupler is used. Couplers (or fast light PCWs) include *Step coupler* (r=0.27a, dW=0.15a, s_1=s_2=s_3=0); *Engineered Step coupler* (r=0.27a, dW=0.15a, s_1=0, s_2=-0.05a and s_3=0.25a); *Group Index Taper* (dW=0, s_1=s_2=s_3=0), where the hole radii are gradually increased (quadratically) from the interface of the engineered PCW with the fast light PCW to the interface of fast light PCW with the ridge waveguide by 15nm [33]; *Expanded Lattice coupler* in which the hole spacing in the fast light region is increased by 30nm (see Fig. 5 of REF. [37]); and finally, *Reduced Hole-size* coupler (r=0.24a, dW=0.15a, s_1=s_2=s_3=0), in which the holes sizes are about 10nm smaller in radius compared to the engineered PCW [46].

From the fabrication point of view, only *Step coupler* and *Expanded Lattice coupler* result in complete design with a uniform hole size. As demonstrated in Fig. 4.2.1.2(d), the *Step coupler* outperforms all the other types, and in the bandwidth of interest. Also, the performance of the *Step coupler,* whose design is simpler, is closest to that of the *Expanded Lattice coupler*. The *Engineered Step coupler* provides the sharpest transition near the band edge, and thus, is a good candidate for devices such as band-edge cut-off based modulators [47].

Here, we notice an advantage of longitudinal lattice shifting compared to lateral lattice shifting in designing the coupler region. When liberalizing the defect mode band by lateral lattice shifting, the defect mode of the fast light PCW is red-shifted compared to that of the slow-light PCW. Since longitudinal lattice shifting does not red-shift the defect mode, designing the coupler requires less widening of the defect line, and also the larger gap-size is expected from the experimental results. We found that best coupling though the step coupler to the designed engineered PCW is at least 4% more efficient over the low-dispersion bandwidth than coupling through the step coupler to a lateral lattice shifted design (dW=0, r=0.295a, t_1=0.15a, and t_2=0) with nearly similar SF=0.28 and n_g=25.5. Our final device consists of 250 periods of the designed band engineered PCW (r=0.27a, dW=0, s_1=0, s_2=-0.05a and s_3=0.25a) and 8 periods of the Step coupler (r=0.27a, dW=0.15a, s_1=s_2=s_3=0) on each side.

For an accurate measurement of group index, an integrated, on chip device which works based on Fourier transform spectral interferometry [48] is also designed and fabricated. Compared to the other group-index measurement techniques, such as detecting Fabry-Perot interference inside the sample itself [49] or time of flight measurements [50], this method provides group index as a function of wavelength over the transmission band in a single-shot measurement, and without uncertainty in choosing the fringes [48]. The scheme presented herein, integrates delay lines, beam splitters and beam combiners on the same chip as the PCW device and also eliminates post-sample polarization compared to the Mach-Zehnder interferometric setup presented in [48].

4.2.2 Fabrication and Testing of Band-Engineered PCW for Modulator

The chip is fabricated on commercially available SOI wafers from SOITEC, which have a 250nm thick silicon device layer, 3μm thick buried oxide (BOX) layer and a 500μm thick silicon handle substrate layer. After electron beam lithography (JEOL JBX-6000) and developing, the resist pattern is transferred to the silicon layer using an HBr/Cl$_2$ RIE etch. A microscope image of the fabricated chip is shown in Fig. 4.2.2.1.
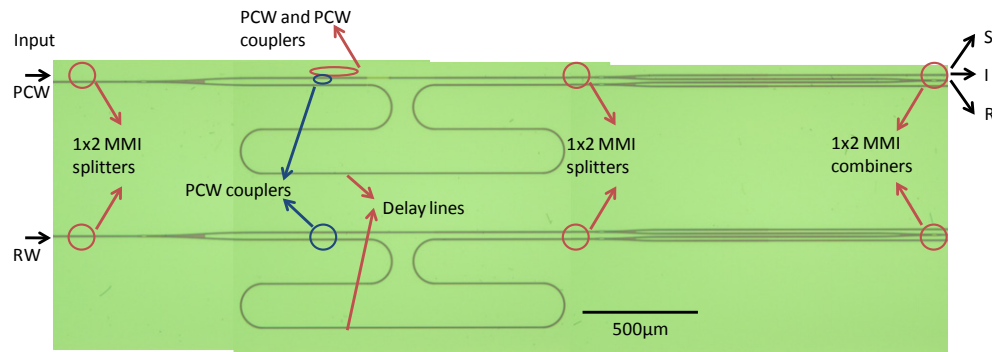

Fig. 4.2.2.1 A microscope image of the fabricated on-chip group index measurement device. The top device contains the PCW and PCW couplers in one arm of the Mach-Zehnder structure and a delay line and PCW couplers in the other arm. In the bottom device, the PCW is replaced with a ridge waveguide.

A scanning electron microscope (SEM) picture of the fabricated PCW device is shown in Fig. 4.2.2.2. The red dashed line shown in Fig. 4.2.2.2(a) demarcates the high n$_g$ PCW from the specially engineered PCW step coupler. The purpose of the step coupler is to provide efficient light coupling from a silicon strip waveguide into the high n$_g$ PCW device. A zoomed in SEM image of the PCW air holes is shown in Fig. 4.2.2.2(b).
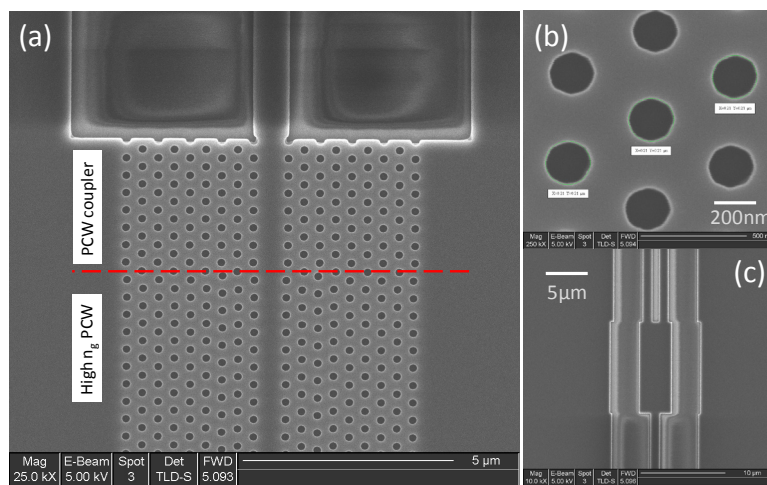

Fig. 4.2.2.2 (a) SEM pictures of the fabricated PCW device showing the PCW coupler and high n$_g$ region, (b) close up of the PCW air holes, (c) 1x2 MMI device employed for splitting and merging the signal coming from two arms of MZI device.

In order to test the device, light from a broadband amplified spontaneous emission (ASE) source, covering 1520~1620 nm, was Transverse Electric (TE)-polarized with an extinction ratio of over

30dB and butt coupled through a polarization maintaining (PM) fiber into each of the two devices shown in Fig. 4.2.2.1. In the top device, the input power is then uniformly divided into two arms of a Mach-Zehnder structure using a 1x2 multimode interference coupler (MMI) shown in Fig. 4.2.2.2(c). One arm (Signal) in the MZ is down tapered and connected to the band-engineered PCW with input/output step couplers. The other arm (Reference) in the MZ is down tapered and connected to 16 periods of the step coupler (combining the input 8 period and output 8 period couplers with no band-engineered PCW). Following the step coupler in the reference arm is a long delay waveguide with length > 5mm, which is needed for phase calculations. The reason for including the PCW couplers is to enhance transmission though the device and to suppress Fabry-Perot oscillations between highly reflective interfaces. Both the Signal and Reference arms are connected to 1x2 MMIs to provide 2 samples of each signal (S and R). One output from each of these MMIs is combined to provide the Interference signal (I). The bottom device is similar to the top one, however, the engineered PCW is replaced with a ridge silicon waveguide, and this bottom device is required in order to normalize the test results [7, 8]

4.2.3. Analysis and Discussions of Test Results for Band-Engineered Low-Dispersion Photonic Crystal Waveguide

The mathematical approach to map the group index of the dispersion profile is given in [48]. For the sake of completeness, we summarize the technique as follows. The interference (I) spectral intensity from any of the two arms is given as

$$I(\omega) = S(\omega) + R(\omega) + \sqrt{S(\omega)R(\omega)} \exp(i\varphi(\omega) - i\omega\tau) + c.c. \qquad (4.2.1)$$

where, $S(\omega)$ and $R(\omega)$ are the spectral intensity outputs of the Signal (S) and Reference (R) arm, respectively, and τ is the time delay from the delay line. $\varphi(\omega)$ is the phase difference between S and I, and therefore, contains the group index data. In order to calculate the group index, the complex interference term is extracted from I by numerically filtering the signal peak with a peck at τ in the time domain. The result is then Fourier transformed back into frequency domain from which the phase data, $\varphi(\omega) - \omega\tau$, is extracted. Then, the group delay of the top device containing the device under test (PCW), $\Delta T^{PCW} = d(\varphi(\omega) - \omega\tau)/d\omega$ is calculated. Applying the same technique on the signals measured from the bottom device, the group delay (ΔT^{RW}) is obtained. Finally, the group index from the PCW is calculated from the difference between the calculated group delays from the two devices, given as

$$n_g(\omega) = (\Delta T^{PCW}(\omega) - \Delta T^{RW}(\omega))c/L + n^{RW}(\omega) \qquad (4.2.2)$$

where, L is the engineered PCW without the couplers and n^{RW} (from RSoft FEMSim simulations) is effective index of the ridge waveguide replacing the engineered PCW in the bottom device. In order to increase the accuracy of the measurement we also include the input/output PCW couplers in Mach-Zehnder setup. However, their effect on the group index measurement is cancelled out because the PCW couplers are included in both arms of both devices.

The measured I, S (the same as PCW transmission) and R signals for our device are shown in Fig. 4.2.3.1(a). Note that our choice for the length of reference arm is made so that the slowing of light in the PCW arm decreases the difference in group delay between the two arms, thus leading to an increase in fringe spacing. Fig. 4.2.3.1(b) shows the calculated group index as a function of wavelength based on the experimental data. Our results indicate a low-dispersion (with less than ±10% fluctuations in group index) transmission over 18 nm bandwidth with an average group index of 26.5. With respect to a ridge waveguide, the PCW device (including the couplers) has a low insertion loss about 3.8 dB independent of wavelength over the low dispersion bandwidth.
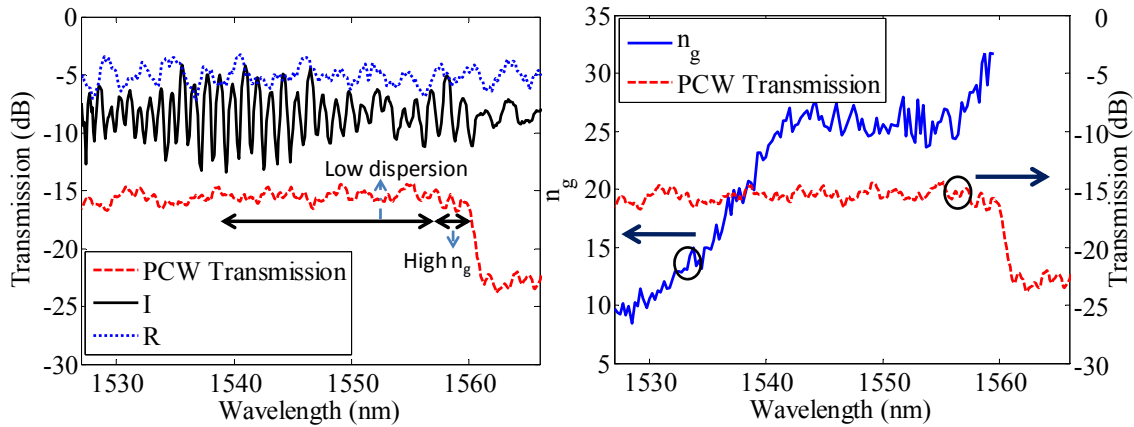

Fig. 4.2.3.1(a) Output spectrum of PCW device (red curve), ridge waveguide (blue curve) and their interference (black curve). (b) Output spectrum of PCW device (red curve) and the calculated group index based on FT method (blue curve). The PCW transmission curve is also provided as a reference [7, 8].

4.2.4. Fabrication and Testing of Mach-Zehnder Modulator

In order to design a MZI modulator, one notices that utilizing the perturbation theory, one can show the required length (L) of the MZI to achieve a π phase shift is given as [51]

$$\frac{L}{\lambda_0} \approx \frac{1}{2\sigma}\left(\frac{n}{\delta n}\right)\frac{1}{n_g}$$

(4.2.3)

where, $\lambda 0$ is the free space wavelength, σ is the fraction of the total optical mode energy that propagates inside the region where the refractive index (n) is perturbed by an amount of δn. ng=c/vg is the group index, where c and vg are the speed of light and optical mode group velocity, respectively. Due to the high group index (c/vg > 25) offered by our design, the length of the electrodes along the PCW can be short. We choose a length of 80 µm, in order to achieve π phase shift with low power operation, i.e. low δn change. In order to achieve the required refractive index perturbation, plasma dispersion effect in a PIN structure is utilized. A schematic of the structure in the active arm is shown in Fig. 4.2.4.1(a), and the doping profile is shown in Fig. 4.2.4.1(b) [8].
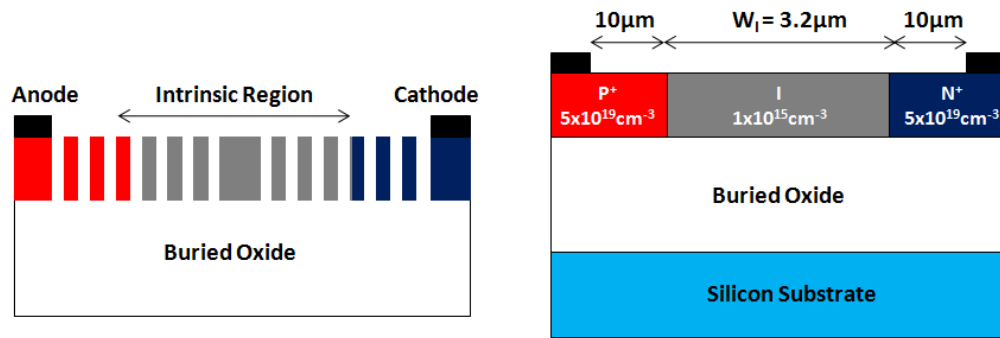
Fig. 4.2.4.1. Schematic of (a) PIN diode embedded PCW modulator arm, and (b) cross section showing doping concentrations and structural dimensions [8]

In our previous demonstrations of PIN modulator, an intrinsic region width WI of 4 μm was chosen and device operation up to 1 GHz was successfully demonstrated [44, 52]. In order to push the operating speed beyond 1 GHz, and as a compromise between the switching speed and the propagation loss. For this work we choose WI of 3.2 μm [53, 54].

Normally, the modal field profile changes drastically with wavelength near the band-edge [55] resulting in wavelength dependent σ. We notice a beneficial feature of the dispersion engineering that is constant group index over large optical bandwidth relatively distant from the band-edge. Therefore, we expect the PCW MZI to have similar characteristics (n_g and σ) over the entire low-dispersion slow light bandwidth.
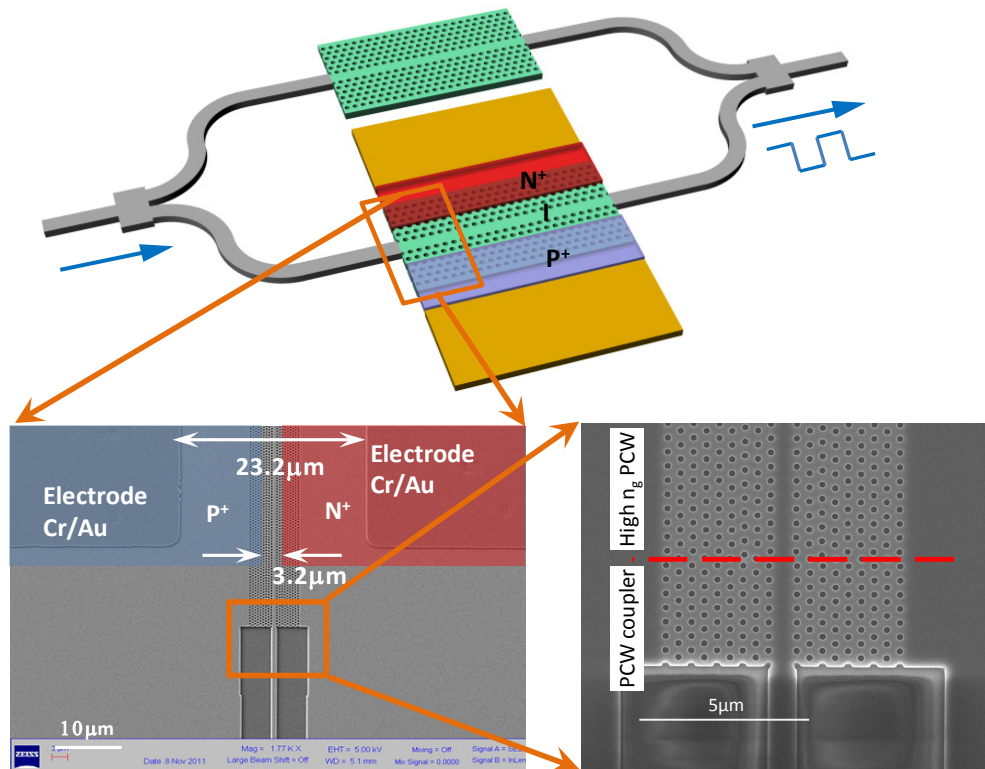

Fig. 4.2.4.2. A schematic of photonic crystal MZI modulator; scanning electronic microscope images of the active arm of the modulator and the photonic crystal waveguide coupler are shown as insets.

A symmetric MZI is designed by placing two 98 μm long PCWs (including 6.3 μm couplers) at the two arms. 1x2 Multimode Mode Interference couplers (MMIs) are used for beam splitting/combining as shown in Fig. 4.2.4.2(a). One of the PCWs is doped to from a PIN as shown in Fig. 5.2.4.2(b). The length of the electrodes is slightly less than that of the slow light PCW to avoid break-down due to the generation of dense currents along the edges of PCWs as discussed in [56].

The modulator is fabricated on a Uni-bond silicon-on-insulator wafer with a 250 nm top silicon layer and 3 μm buried oxide layer. Photonic crystal waveguides, photonic crystal couplers and strip waveguides are patterned in one step using a JEOL JBX-6000FS electron-beam lithography system followed by reactive ion etching. The windows for P+ and N+ implantation were opened by photolithography. Ion implantations of Boron at 30 KeV (surface concentration of $3.00\times10^{14}/cm^2$) and phosphorus at 50 KeV (surface concentration of $1.72\times10^{14}/cm^2$) were performed to obtain an average doping concentration of about 5×10^{19} cm^{-3}. Thermal rapid annealing for 1 min at 950 ^{o}C in a flowing nitrogen environment was performed afterwards to anneal the lattice defects and activate the implanted ions.

Electrode contact windows were then opened by photolithography and the native oxide inside the windows was removed. Aluminum electrodes were made by electron-beam evaporation and a subsequent lift off process. Finally, an ohmic contact was formed by post metallization annealing at a temperature of 400 ^{o}C for 30 mins [53]. SEM images of the fabricated PCW on one arm of the fabricated modulator device are also shown in Fig. 4.2.4.2.

Before performing the modulation tests, we first performed static tests on the fabricated modulator devices. The static characteristic of the PIN diode obtained using Agilent B1500a semiconductor parameter analyzer is shown in Fig. 4.2.4.3. The forward linear resistance is ~200 Ohm.
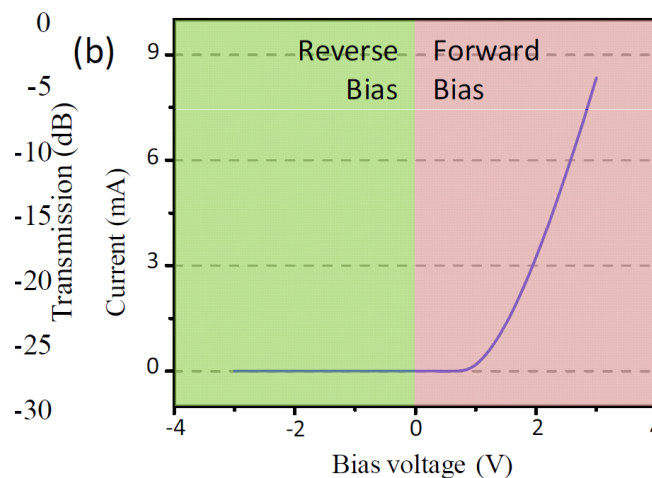

Fig. 4.2.4.3.Static characteristic of the PIN diode [8]

Measurements of the figure of merit Vπ×L and data transmission, described below, are carried out by coupling light from a TE-polarized tunable laser (Santec MLS-2000) into the device through butt coupling and tuning to λ = 1550.48 nm. The modulated output is detected with a gain switchable photodetector (Thorlab PDA10CS) and displayed on the oscilloscope (Agilent 86100A). The voltage Vπ required to produce a carrier injection-induced π phase shift is measured by applying a 100 kHz triangular electrical drive signal, as shown in Fig. 4.2.4.4(a), to a MZI modulator with 80 μm long active arm under a forward bias Vbias = 1.25 V. The drive amplitude is increased until the slope of the modulated optical signal changed sign at the peaks/troughs of the drive waveform, as illustrated in Fig. 4.2.4.4(a) [57]. A complete half-period of optical modulation is observed for a peak-to-peak applied voltage of Vπ = 0.58 V, leading to a figure of merit of Vπ×L = 0. 0464 V.mm, which is less than one third of the lowest Vπ×L for a PCW modulator reported so far [57].

Next, by tuning the optical carrier wavelength over the C band (1520 nm-1560 nm), we obtained variations of Vπ versus optical wavelength as shown in Fig. 4.2.4.4(b). Due to Fabry-Perot oscillations caused by the input and output facets and also back reflections at the MMI's and PCW's interfaces with the strip waveguides, the output optical power fluctuates with wavelength over the low-dispersion bandwidth. At wavelengths that correspond to the peaks of the Fabry-Perot oscillations, the output optical power is high and we are able to observe clear over-modulations [see Fig. 4.2.4.4(b)]. From the over-modulated signal, we are to deduct the Vπ value.

According to Eq. (4.2.3), at a constant L, since δn is linearly proportional to Vπ, one can show

$$V_\pi \approx B \frac{\lambda_0}{n_g}$$

(4.2.4)

where, B is a constant. The trend in Vπ variations closely follow those of the group index as depicted in Fig. 4.2.3.1(a). Interestingly, the group index slightly increases at shorter wavelengths over the low-dispersion slow light bandwidth (λ≳1539nm); one notices that the Vπ slightly decreases at shorter wavelengths over the low-dispersion slow light bandwidth consistent with Eq. (4.2.4) (λ≥1539nm).

The rectangular electrical signal for GHz operation is generated through Agilent 8133A 3 GHz pulse generator. The Vbias is 1.25 V and the Vpp is 1.50 V. The output optical signal is amplified by erbium-doped fiber amplifier and converted to electrical signal by 22 GHz photodetector (DSC30S). The waveform is captured by Agilent 86100A as shown in Fig. 4.2.4.4(c) [8]. We were able to achieve 2 GHz operating speed using 80 μm long lumped electrodes. Due to excess noise generated by our EDFA, we are unable to accurately determine the extinction ratio of our modulator device.
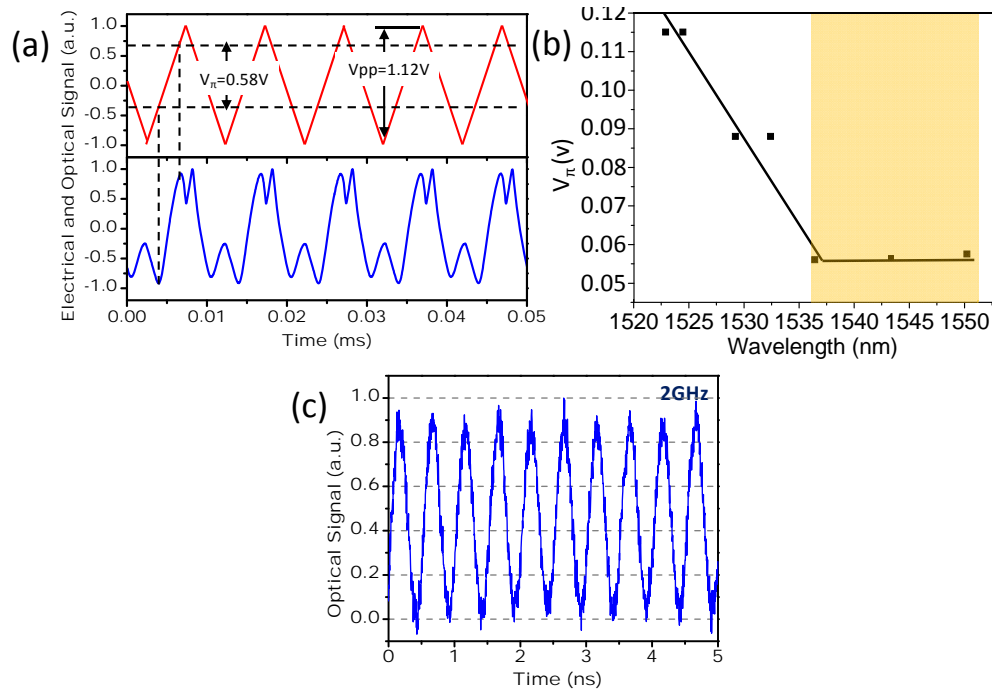
Fig. 4.2.4.4. (a) triangular electrical drive signal with a Vpp of 1.12 V and Voffset of 1.25 V (top). The over modulated optical signal indication a Vπ of 0.58 V (bottom); (b) Variations of Vπ versus the optical carrier wavelength; (c) the optical signal of 2 GHz operation at λ = 1550.48 nm. The low-dispersion slow-light wavelength range is highlighted in (b) [8]

4.3. Silicon Nanomembrane Transfer Process

4.3.1 Introduction to Transfer Process

Flexible electronics and photonics have attracted a lot of attention in the past decade owing to their potential utility for a wide range of applications. Single crystal silicon forms the fundamental backbone of modern microelectronic industry. However, by far the devices are limited to rigid substrates which can not satisfy the growing demand for flexible electronics and photonics seen in the last few years. Encouraging successes in this emerging field include flexible and rollable paper-like displays [58], flexible silicon integrated circuits [59], photonic crystal filters [60, 61], smart skins [62], etc. Among all the transferable materials, single crystal silicon-based nanomembrane may be most promising for both electronic and photonic devices [60], because it not only possesses high carrier mobility and mechanical durability, but is also optically transparent in the near infrared region. However, transferring in-plane photonic components onto flexible substrates is still a great challenge because the photonic devices are sensitive to any kind of shifting or fracture [63].

There are three methods to fabricate and transfer silicon nanomembranes on other target substrates, such as flexible substrates: 1) Bonding and back polishing, 2) peel up transfer and 3) stamp transfer techniques.

31

In the bonding and back polishing method, a silicon wafer is bonded to the flexible substrate and polished down to the desired thickness. However, it is difficult to polish the wafer down to several hundred nanometers while maintaining good uniformity. An alternative approach is to bond a patterned or an unpatterned silicon on insulator (SOI) wafer top side down on the flexible substrate and perform deep silicon etch to remove the handle wafer [64]. The dry etch stops at the buried oxide layer, and therefore, the thickness of the nanomembrane is set by the silicon device layer. The device yield from this kind of a method is considerably higher than other methods.

In the peel up and stamping methods, free-standing silicon nanomembrane is obtained by immersing the SOI wafer into hydrofluoric (HF) acid solution. The HF solution selectively etches the buried oxide away and releases the silicon nanomembrane from the SOI wafer. For the two methods, it is crucial to have the released silicon nanomembrane settle and conformally bond with the handle wafer via weak Van der Waals forces. In order to ensure this, the thickness of the buried oxide layer must be small enough. In order to transfer the nanomembrane onto the flexible substrate using the peel up method, a flexible substrate coated with a sticky layer on one side is used to peel the nanomembrane from the handle wafer. This method requires the adhesive has stronger adhesion to the flexible substrate than to the silicon wafer, otherwise the adhesive will be peeled off and adhere to the handle silicon wafer during the peel up process. Materials that satisfy these requirements, and at the same time providing good optical and electrical characteristics, are very limited. Stamp printing provides a solution to this problem through transferring the silicon nanomembrane based device onto an intermediate media first, before transferring the nanomembrane onto the flexible substrate in the final step. The fact that the adhesion between the silicon nanomembrane and the polydimethylsiloxane (PDMS) stamp is strong at high peeling speeds, while weak at low peeling speeds makes PDMS a good option for the stamp materials [65]. This special property can be further enhanced by using appropriately designed microstructures on the surface of the stamp [66].

Table 4.3.1. Comparison of the nanomembrane transfer methods

Methods	Advantage	Disadvantage
Bonding and Back polish	High yield Large Area Unpatterned Nanomembrane	High cost
Peel up	Simple	Not suitable for alignment and multilayer stacking Material Issues
Stamp printing	Suitable for alignment	Complicated Process Transferring delicate photonic

	Can transfer multiple materials High potential for mass production Low cost	components is difficult

Stamp printing method has been used for transferring various membrane based components [67-69], including silicon nanomembrane based electrical circuits. However, this method cannot be applied to transfer in-plane photonic devices because the devices usually have large length to width ratio and are sensitive to shifting and breaking. In this Phase II program, we modified and further developed the stamp printing method in order to facilitate transfer of delicate photonic devices.

4.3.2 Transfer Process Utilizing Photoresist as a Mechanical Support

The photonic devices are fabricated on commercially available SOI wafers (SOITEC) with 230 nm top silicon layer and 3 μm buried oxide, as shown in Fig. 4.3.2.1(a) [1]. The silicon device layer is first oxidized to create a 50 nm thick top oxide layer which serves as a hard mask for the silicon etching. This oxidation consumes 20 nm of silicon, leaving a final silicon thickness of 230 nm. The photonic devices are patterned using electron beam lithography. Following this, a 20 nm nickel layer is deposited using electron beam evaporation and a standard lift-off process is used to realize image reversal. The pattern is transferred to the silicon oxide hard mask using reactive ion etching (RIE). A HBr/Cl$_2$ RIE etch is then used to transfer the pattern to the silicon layer. Finally, the metal is removed by piranha cleaning. The top oxide layer is then removed using buffered hydrofluoric (BHF), as shown in Fig. 4.3.2.1(b).

Unlike electronic devices, photonic devices usually have high length to width ratios, which makes the transfer more difficult. The performance of photonic devices can be impaired by any small shifting or nanomembrane fracture during the transfer procedure. Therefore, providing mechanical support during the transfer process becomes necessary, especially when the buried oxide layer is >300nm. Before releasing the nanomembrane by etching the underlying BOX layer, a photoresist is spun cast over the device layer in order to provide mechanical support to the devices during transfer. After baking, the photoresist is patterned to open several specially designed windows for etchant penetration. Hard bake is carried out after developing [Fig. 4.3.2.1(c)]. If either HF or BHF is utilized to remove the sacrificial layer, shifting and breaking of nanomembrane devices is possible due to the thick buried oxide layer. In order to address this critical issue, HF vapor, instead of solution is used to minimize shifting of devices. Upon complete removal of the buried oxide layer, the residual HF is cleaned thoroughly using acetone vapor. Following this, the chip is baked at 65°C in order to evaporate the water generated by the reaction of the HF and buried oxide so that the device bonds well with the silicon handle wafer [Fig. 4.3.2.1(d)]. The photoresist is then removed using Acetone and Oxygen plasma, as shown in [Fig. 4.3.2.1(e)].
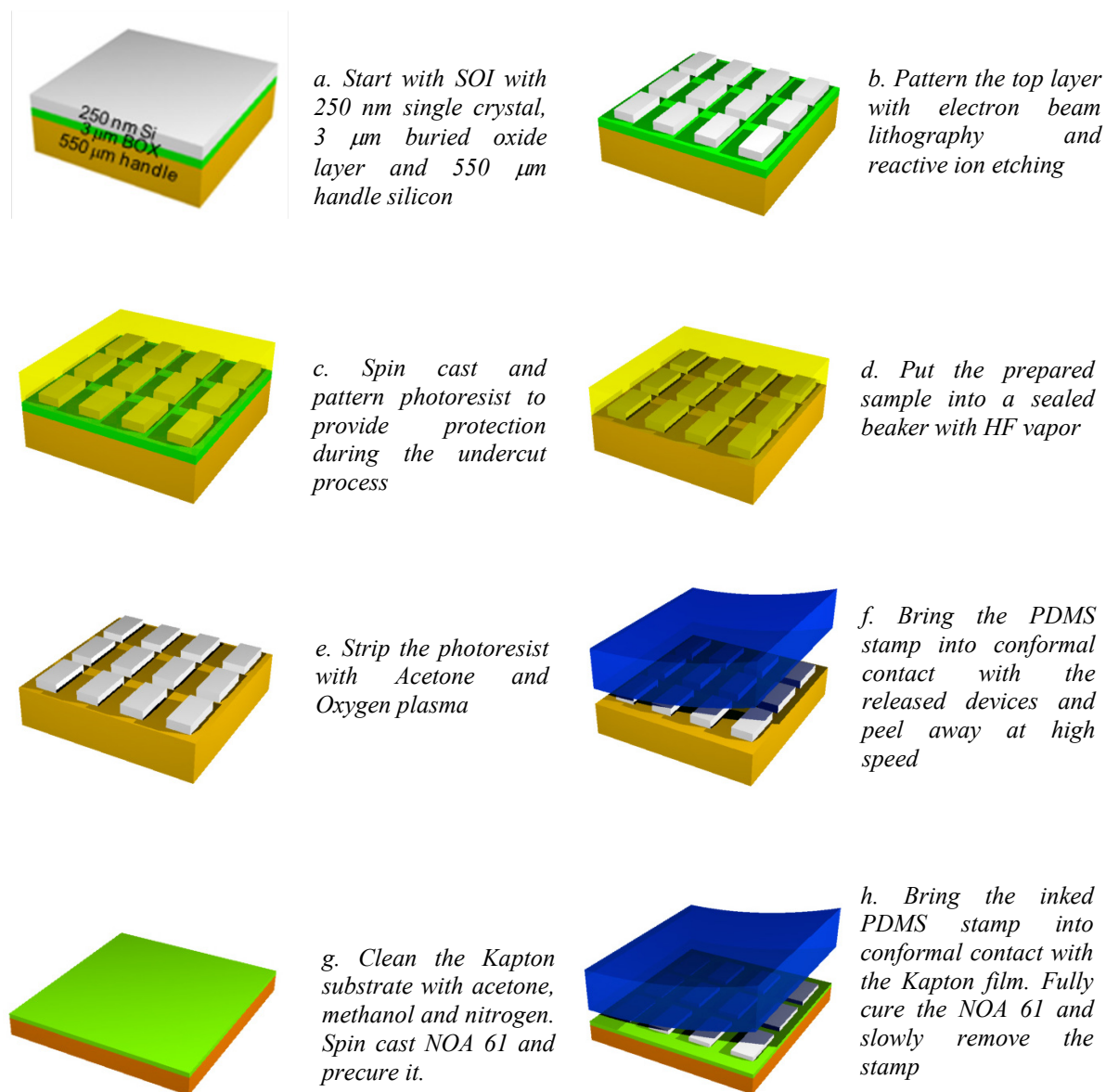
a. Start with SOI with 250 nm single crystal, 3 µm buried oxide layer and 550 µm handle silicon

b. Pattern the top layer with electron beam lithography and reactive ion etching

c. Spin cast and pattern photoresist to provide protection during the undercut process

d. Put the prepared sample into a sealed beaker with HF vapor

e. Strip the photoresist with Acetone and Oxygen plasma

f. Bring the PDMS stamp into conformal contact with the released devices and peel away at high speed

g. Clean the Kapton substrate with acetone, methanol and nitrogen. Spin cast NOA 61 and precure it.

h. Bring the inked PDMS stamp into conformal contact with the Kapton film. Fully cure the NOA 61 and slowly remove the stamp

Fig. 4.3.2.1 Process flow for transferring Si nanomembrane based photonic devices on to flexible substrate

The PDMS stamp is prepared by mixing the base and agent with a ratio of 5:1 and curing at 90°C for 60 mins. The base and agent ratio is chosen to make the PDMS rigid enough to prevent the bending induced breaking of the devices during the printing process. The PDMS is bonded to a glass slide after treating the surface of PDMS and glass slide with minor Oxygen plasma and bringing the treated surfaces into contact under pressure. The assembly is then put in an oven for two hours in order to strengthen the bonding. The Oxygen plasma can neither be either too strong or too weak. Strong Oxygen plasma increases the roughness of the PDMS surface, while the surface of PDMS cannot be activated with weak Oxygen plasma. The prepared PDMS stamp is then brought into a conformal contact with the released photonic device on the handle wafer, and is peeled up at high speed, leading to the transfer of nanomembrane device from the handle

wafer onto the PDMS stamp [Fig. 4.3.2.1(f)]. It has been observed that at high peeling speeds, the adhesion between PDMS and silicon nanomembrane is larger than the Van der Waals force between silicon nanomembrane and the handle wafer [65]. The Kapton film is cleaned by acetone and methanol before use. A gentle oxygen plasma or UV exposure could improve the adhesion between the adhesive and the Kapton surface. Later on, NOA 61 is spun cast on the Kapton substrate to a thickness of 5 µm [Fig. 4.3.2.1(g)]. The advantage of using NOA 61 is that it has good optical characteristics and low shrinkage during the curing procedure. NOA 61 is pre-cured for 5 mins with 100W UV lamp. Then, the 'inked' PDMS is brought into contact with NOA 61 on the Kapton substrate and cured together through illuminating NOA61 from the top. After fully curing the NOA 61, the PDMS stamp is removed at low speed, leaving the devices on the Kapton substrate [Fig. 4.3.2.1(h)]. We fabricated and transferred several photonic components including multimode interference (MMI) couplers, strip waveguides etc. Fig. 4.3.2.2(a) shows a microscope released multimode interference (MMI) coupler. The shape and position after buried oxide removal are preserved, indicating that the protection layer is effective. A picture of the inked PDMS containing 60µm wide waveguides is shown in Fig. 4.3.2.2(b).
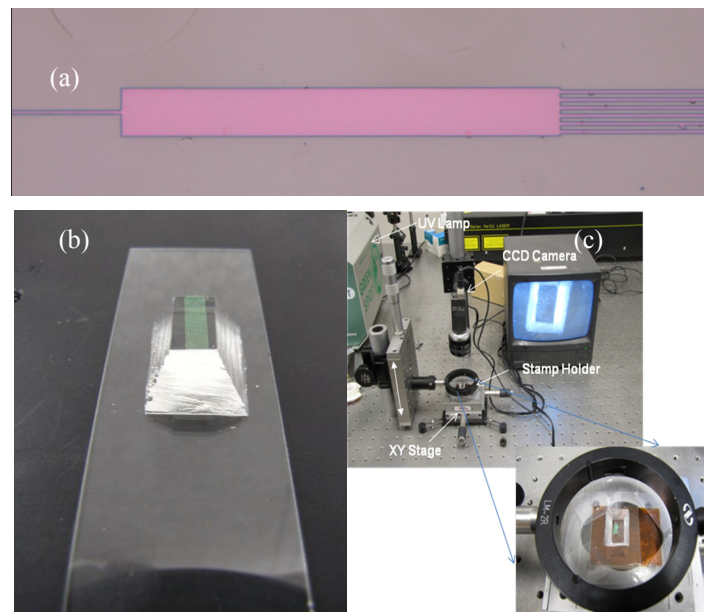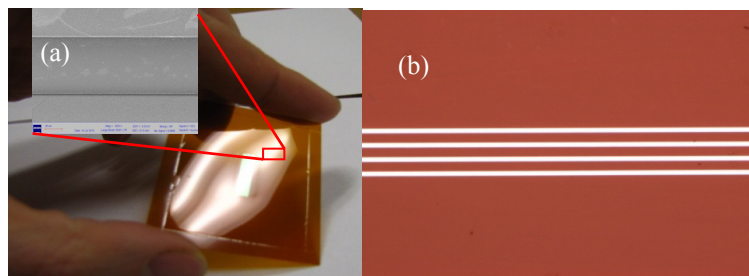

Fig. 4.3.2.2 Pictures showing (a) released multimode interference (MMI) coupler with no shifting; (b) the inked PDMS (with 60µm waveguides); (c) set up for nanomembrane transfer
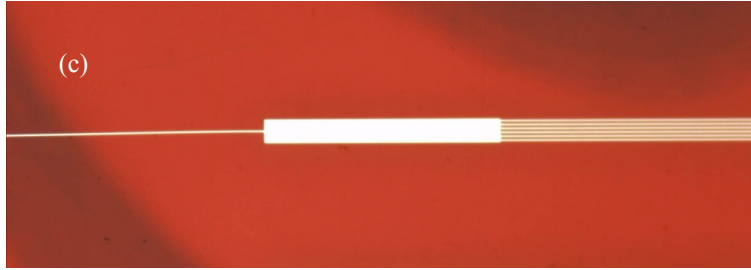
Fig.4.3.2.3 Transferred photonic components (a) microscope and SEM picture (inset) of 60 μm waveguides;

(b) 2μm waveguides; (c) 1 by 6 multimode interference (MMI) coupler

The process described above is realized using a simple set up, as shown in Fig. 4.3.2.2(c). The PDMS is mounted on the stamp holder at a small angle to reduce the formation of bubbles during the contacting procedure. The stamp is lowered and brought into a conformal contact with the released devices. Then, the stamp is peeled up quickly. During the printing process, the PDMS stamp is lowered down to contact the pre-cured NOA 61 film on the Kapton substrate. The whole system is cured by illuminating UV light from the top of PDMS. The stamp is slowly removed from the substrate by rotating the knob of the moving stage after curing. Fig. 4.3.2.3(a) shows the transferred 60 μm straight waveguides on a 125 μm thick Kapton film. The transferred devices have high flatness as shown in the inset of Fig. 4.3.2.3(a). Fig. 4.3.2.3(b) shows the microscope picture of 2 μm wide, 8mm long straight waveguides we transferred. Fig. 4.3.2.3(c) shows a successful transfer of a 1x6 multimode interference (MMI) coupler.

4.3.3. Modified Transfer Process Utilizing Suspended Configuration

In section 4.3.2, a general transfer process we developed to transfer SiNM onto flexible substrates was presented. However, such a method is not suitable for transferring very narrow waveguides since the adhesion between the NM and PDMS during transfer is weak. Therefore, we modified our transfer process in order to be able to transfer any kind of photonic structure onto flexible substrates.

In this section, we present a new stamp printing method with which 30 μm wide, 230 nm thick, up to 5.7 cm long multimode waveguides are transferred onto a flexible substrate with yield > 90% [2]. The propagation loss of the transferred waveguide is measured to be ~1.1 dB/cm, which is comparable with waveguides on SOI. This method has also been applied to transfer other intricate structures such as PCW and MMI with minimum feature sizes of 200 nm and 2 μm, respectively, and this process is relatively independent of the thickness of the BOX. According to the best of our knowledge, this is the first demonstration of operational SiNM based in-plane flexible photonic devices, which we believe, could open an entirely new field with a wide range of useful applications.

A 30 μm wide, 8 mm long waveguide is fabricated with commercially available SOI from SOITEC with 250 nm single crystal silicon, 3 μm BOX and 500 μm handle silicon. The SOI is first oxidized to create 45 nm top oxide layer, which serves as hard mask for silicon etching. This oxidation consumes 20 nm silicon, leaving a silicon layer of 230 nm. After electron beam

lithography (JEOL JBX-6000), a 20 nm nickel layer is deposited and a standard lift-off process is used to invert the pattern. The pattern is transferred to the silicon oxide hard mask by reactive ion etching (RIE). The metallic layer is then removed by piranha cleaning. An HBr/Cl$_2$ RIE etch is used to transfer the pattern to the silicon layer, as shown in Fig. 4.3.3.1(a).
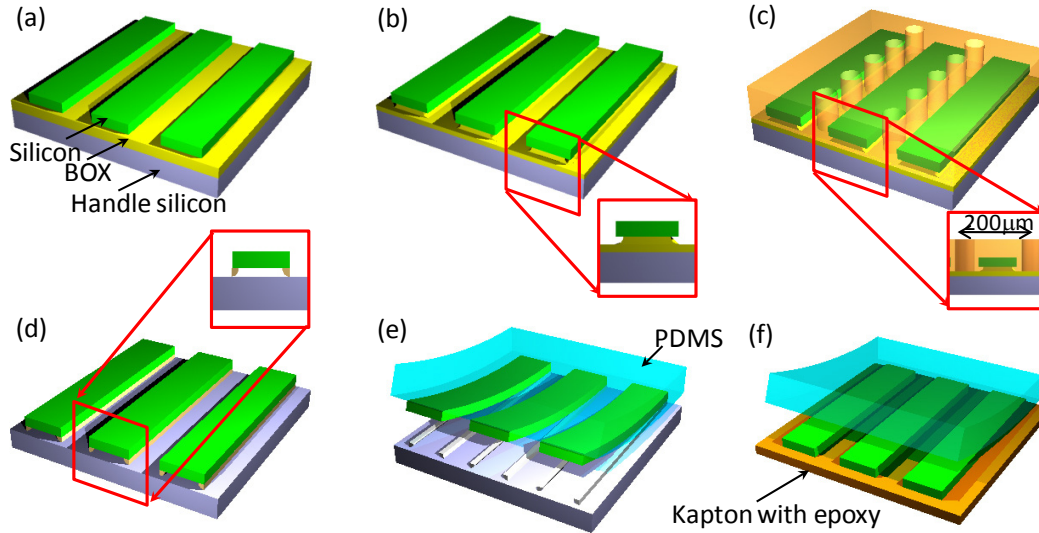

Fig. 4.3.3.1. Schematic illustration of the stamp printing process exploiting a suspension structure. (a) The patterned SOI chip. (b) Illustration of chip after first undercut etching. (c) Application and patterning of the supporting layer. (d) SiNM suspension on pedestals after complete undercut etching. (e) Peeling up of the released SiNM with PDMS stamp. (f) Printing of SiNM devices onto a polyimide film [2].

To form pedestals, the patterned wafer is put into a 6:1 buffered oxide etch (BOE) for 5 mins to partially remove the silicon dioxide underneath the waveguide, as shown in Fig. 4.3.3.1(b). Then, AZ 5214 photoresist is spin coated at 4000 rpm for 30 seconds, resulting in a film thickness of ~1.7 μm. The resist also fills the exposed edges under the waveguides, thus forming polymeric pedestals, as shown in Fig. 4.3.3.1(c). Array of holes with diameter of 100 μm and pitch of 200 μm are patterned on the resist to let the etchant penetrate for BOX removal. The sample is hard baked at 110 °C for 3 mins, and then put into a beaker filled with HF vapor. HF vapor can be generated simply by covering a beaker with concentrated HF solution. The etch rate is ~50 μm/h, which can be controlled by opening different sizes of holes on the cover. After completely removing the BOX, the SiNM, protected by the photoresist, will settle down to the handle silicon. The supporting layer and vapor etching sufficiently prevent the SiNM from the shifting caused by the fluid flows during HF etching. The result can be further improved by heating the sample up during the undercut etching process to let the by-product water from the chemical reaction evaporate. After gently cleaning and drying the sample with nitrogen, oxygen plasma is used to remove the photoresist everywhere, except the region underneath the nanomembrane, as shown in Fig. 4.3.3.1(d). The center region of the SiNM sags down and contacts the underlying substrate. The contact area can be controlled by tuning the dimensions of the pedestal through adjusting the first step BOX etching time. This controllability is important because, when the contact area becomes too large, it becomes very difficult to peel the SiNM up.

The etching time is controlled in order to initiate sufficient delamination formation between silicon nanomembrane and silicon surface during retrieval with an elastomeric stamp. The etching time is optimized to 5 mins, forming a pedestal ~200 nm high.

A polydimethylsiloxane (PDMS) stamp is prepared by mixing base and agent with a ratio of 6:1, and cured at 90°C for 2 hours. The stamp is bonded to a glass slide through oxygen plasma surface activation and 2 hour 90 ^{o}C annealing. Bringing the stamp into contact with the substrate and then peeling it back at high speed lifts the SiNM structure from the handle silicon through initiating delamination at the interface between the pedestals and the SiNM, as shown in Fig. 4.3.3.1(e). A 125 μm thick polyimide film (Kapton, DuPont) is cleaned with Acetone and Methanol. NOA 61 (Norland Optical Adhesive) is spin coated at a speed of 4000 rpm for 60s, forming a film thickness of ~7 μm. The epoxy is pre-cured for 10 mins (7.5 mW/cm^2). Then, the "inked stamp" is brought into contact with the pre-cured epoxy film. The film is cured from top side down through the PDMS, and the stamp is slowly retrieved, leaving SiNM on the flexible substrate, as shown in Fig. 4.3.3.1(f). The whole sample is put into an oven at 60°C for 12 hours to achieve better adhesion between NOA 61 and SiNM. The fully cured NOA 61 has good transmission at 1550 nm with a refractive index of ~1.54. The scanning electron microscope (SEM) and the optical microscope images for the corresponding steps outlined in Fig. 4.3.3.1 are shown in Fig. 4.3.3.2.

In order to test the transferred waveguides, the end facets are prepared. The flexibility of the SiNM, NOA 61 and Kapton makes it very difficult to prepare the end facets of the SiNM waveguide for light coupling. Therefore, we first use RIE (CHF_3/O_2) to etch the end of the waveguide and the NOA 61 underneath away. Then, the Kapton substrate is diced less than 14.5 μm away from the edge of waveguide in order to enable light coupling using a polarization maintaining (PM) lensed fiber with working distance of 14.5 μm and spot diameter of 2.5 μm. The cross section of the prepared facet is shown in Fig. 4.3.3.3(a). The output light from the waveguide is collected with multimode fiber with a mode diameter of 50 μm. Through a top down infrared camera, as shown in Fig. 4.3.3.3(b), the output spot can be clearly observed, indicating strong light emission. The measured insertion loss is ~25 dB for 7 mm transferred waveguide, which is about 6 dB more than the waveguide before transfer, as shown in Fig. 4.3.3.3(c).
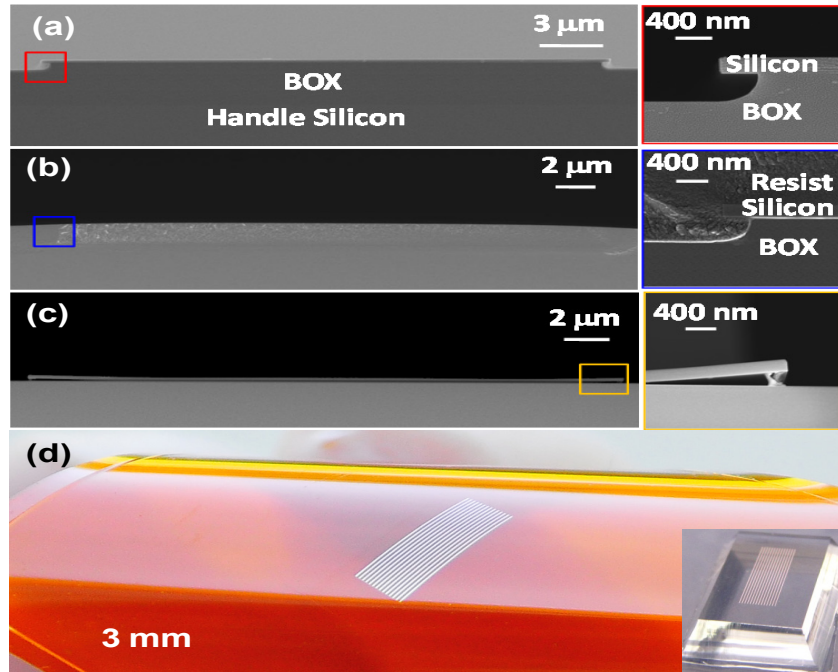
Fig. 4.3.3.2. (a~c). SEM image of the cross section of the SiNM. (a) After BOE etching for 5 min. (b) After spin casting photoresist. (c) After full undercut etching and removing photoresist with oxygen plasma. (d). Transferred SiNM waveguide showing good flexibility and the PDMS "inked" with SiNM (inset) [2]

This transfer technique has been used to also transfer intricate devices such as 1x6 MMI and PCW, with a minimum dimension of 2 μm and 200 nm, as shown in Fig. 4.3.3.3(a) and 4.3.3.3(b), respectively, which are not feasible to be transferred using conventional approach.
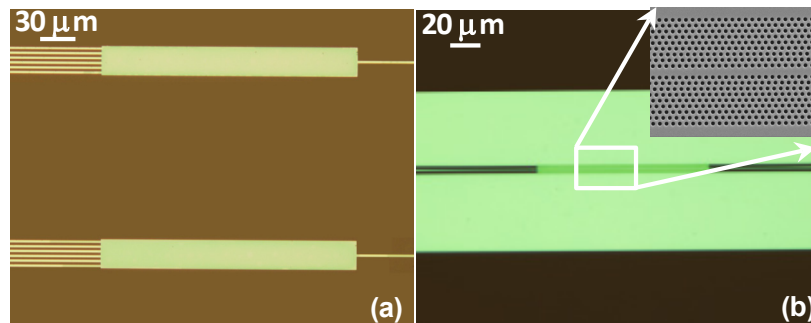

Fig. 4.3.3.3 (a) Transferred 1 by 6 MMI couplers. (b) Transferred Photonic crystal waveguide [2].

In summary, we have developed a new stamp printing process based on supporting layer and suspension structure. Intricate SiNM devices such as MMI and PCW, which are difficult to transfer using conventional techniques, have also been transferred successfully using our technique. This demonstration opens vast possibilities for a whole new area of high performance flexible photonic components using SiNM technology.

4.3.4. Large Area Nanomembrane Transfer via Bonding and Etching

The transfer process flow is described in Fig. 4.3.4.1 [4]. As illustrated in Fig. 4.3.4.1(a), the entire material stack from top-down contains a SOI wafer (675 μm silicon handle, a 3 μm BOX

layer, a 250 nm single crystal silicon device layer), a 5 μm SU-8 coated on the silicon device layer, a 5 μm SU-8 coated on the glass slide, and a 1 mm thick glass slide. Before bonding, a 2 cm × 2 cm SOI chip and a 2.5 cm × 2.5 cm glass slide are thoroughly cleaned in piranha solution. The native oxide on the surface of SOI is removed with buffered oxide etchant (BOE). After being rinsed in de-ionized water and dried with nitrogen, the chip and the slide are dehydrated in a convection oven. Next, a 5 μm thick SU-8 layer is spun on the SOI chip and also on the glass slide, and soft baked at 95 ^{o}C to evaporate the solvent. Then, the SOI chip is put upside down on the glass slide and placed in an oven at 65 ^{o}C for 20 mins without applying any pressure. The glass transition temperature of the non-cross-linked SU-8 is 64 ^{o}C [70, 71], and at the glass transition temperature or above, SU-8 exhibits excellent self-planarization, which minimizes the edge bead effect as well as other thickness variations [71]. Pressure is applied afterwards through a home-made bonder, which is shown in Fig. 5.3.4.1(g). The material stack is mounted between the two thick Pyrex glass slides. The steel ball and the Belleville washer spread the point force generated by the thumb screw onto the thick Pyrex glass plate. The pressure is higher at the center than at the edges. This gradient pressure distribution avoids the formation of air cavities in between the two SU-8 layers. As the polymer flows, the pressure decreases, which can be compensated by the thermal expansion of the Belleville washers. The sample is kept in a 65 ^{o}C vacuum oven for 20 hours to allow for polymer to reflow and to squeeze out the trapped air bubbles. After that, the sample is illuminated by 365 nm ultraviolet light through the glass slide to crosslink the SU-8 polymer. Exposure dose is around 900 mJ/cm^{2}. A second long term post exposure bake (PEB) at 65 ^{o}C is done to further crosslink SU-8. Baking at a low temperature helps minimize the strain, as the thermal expansion coefficients of silicon and SU-8 are different. It is also possible to tailor the stress by controlling the PEB temperature, which can be exploited to build active photonic devices such as modulators [3].

After bonding, the silicon handle is removed by DRIE, as described in Figs. 4.3.4.1(c) and 4.3.4.1(d). Since DRIE generates heat, the carrier wafer, on which the sample sits, is kept at ~ 10 ^{o}C through Helium flow underneath. However, the thermal conductivities of SU-8 and glass slides are merely 0.2 W/mK and 0.96 W/mK, respectively, and thus the heat generated by the etching process cannot be dissipated fast enough. Consequently, a significant temperature gradient builds up between the top surface and the glass slide, subjecting the sample to cracking. The mismatch of the coefficients of thermal expansion (CTE) further aggravates the thermal issue. To control the thermal budget, the silicon handle is mechanically polished down to ~100 μm, as shown in Fig. 4.3.4.1(c) and Fig. 4.3.4.1(h), to shorten the etching time. The etching recipe is also carefully modified to accommodate the thermal requirements. The conventional Bosch process contains three steps: polymer deposition, polymer etching, and silicon etching. The polymer deposition time is set to 5 s to protect the perimeter of the membrane, because the charges accumulated on the glass surface bend the electric field and etch silicon and SU-8 from the side. The anisotropic polymer etching step is skipped in this application because the quality of the perimeter is not important. The polymer is removed during the silicon etching step. The inductively coupled plasma (ICP) power is carefully tuned to keep it slightly above the threshold

of maintaining plasma to reduce the heat generation rate to match the heat dissipation rate. However, this adjustment sacrifices the etch rate. To compensate it, a long silicon etching time of 30 s is used in each cycle. The silicon etch rate of this recipe is around 2.7 μm/cycle. Besides, the recipe has a high selectivity (~80) of oxide to silicon, meaning the 3 μm BOX can be used as a stopping layer to protect the SiNM underneath, and it can be removed by hydrofluoric (HF) acid etching afterwards. The SiNM with BOX after DRIE is shown in Fig. 4.3.4.1(i).
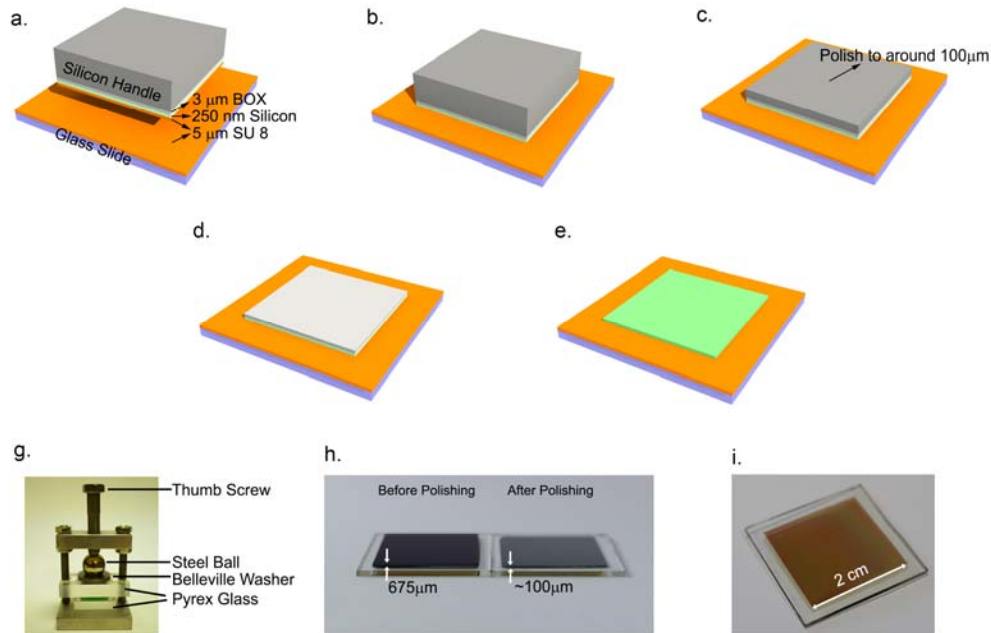
Fig. 4.3.4. 1. Transfer process flow chart. a. The material stack structure. From top down, a 675 μm thick silicon handle, a 3 μm thick BOX layer, a 250 nm thick single crystal silicon device layer, a 5 μm thick SU-8 on silicon layer, a 5μm SU-8 on a 1 mm thick glass slide. b. Bond the SOI upside down onto the glass slide. c. Polish the handle silicon down to ~100 μm. d. Etch the silicon handle away with deep reactive ion etching using BOX as a stopping layer. e. Remove the remain of BOX with concentrated HF solution. f. Pattern the transferred SiNM with photolithography or electron beam lithography. g. Schematics of the home made bonder. h. Side view of a sample before and after polishing. i. transferred SiNM after removing the handle [4].

Before removing the BOX layer, photoresist is applied on both the bottom and the top of the sample except the BOX region to protect the glass slide and the SiNM . Instead of immersing the whole sample into HF solution, which causes delamination because HF attacks the bonding between glass and polymer, a few droplets of HF are applied on the BOX directly. The surface tension of the silicon dioxide constrains the solution within the SiNM without flowing over. The drawback is that etching speed could fall as the HF concentration decreases. Thus, a few more drops of HF needs to be added to maintain necessary HF concentration. A picture of the transferred SiNM is shown in Fig. 4.3.4.2. After transfer, the thickness of the SU-8 is measured to be around 9.4 μm, as indicated in the scanning electron microscopy (SEM) picture shown in the inset of Fig. 4.3.4.2. The thickness variation across the entire chip is ~200 nm, due to uneven pressure during the bonding step. The transferred SiNM is examined with an optical microscope, and no visible defects are found.

The transferred SiNM can be patterned into photonic structures through conventional techniques such as photolithography and e-beam lithography. We used e-beam lithography to pattern the SiNM. The patterning process is similar to that described in [6], except the resist processing condition. The resist ZEP 520 is spin-coated at 6000 rpm for 35s, forming a film of ~300 nm. Due to the CTE mismatch between silicon and SU-8, the resist film, with CTE being optimized to match silicon, is subject to cracking if baked at the standard process temperature of 180 $^{\circ}$C. Therefore, the sample is pre-baked at a lower temperature of 90 $^{\circ}$C for an extended duration of 30 mins to evaporate the solvent. The resist is patterned with JEOL 6000, and then the pattern is transferred onto SiNM through reactive ion etching (RIE).
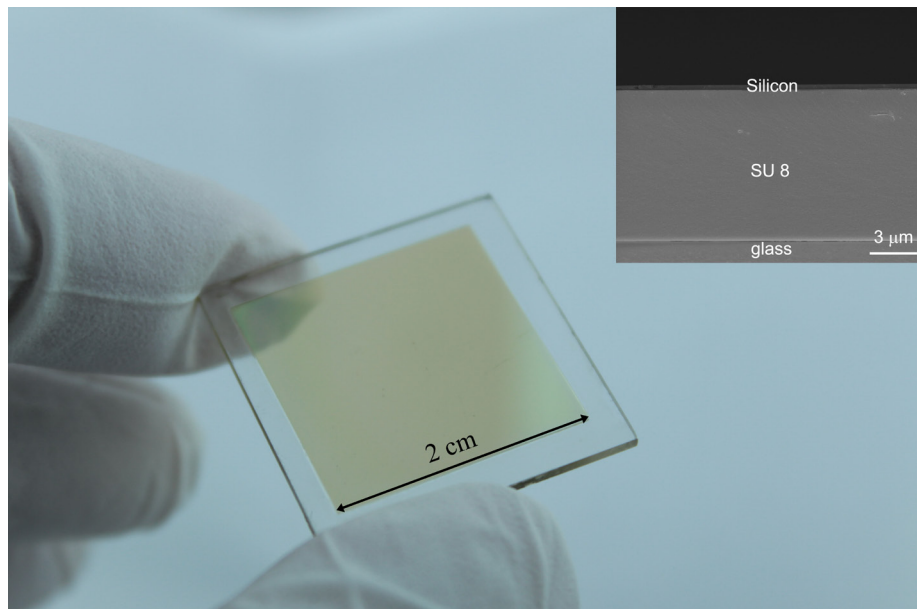

Fig. 4.3.4.2. Transferred SiNM on glass slide. Inset: cross section SEM image of the transferred SiNM. After transfer, the SU-8 layer is ~9.4μm thick [4].

4.4 Coupling

This task represents a key element for the SiNM photonic devices. After transferring photonic devices onto flexible substrates, there needs to be a way to couple light into and out of waveguides in order to make use of these components for practical applications. We are investigating both planar and surface normal coupling schemes that can be used for different applications

4.4.1. Waveguide Facet Preparation and End-Fire Coupling Scheme

A difficulty in characterizing the transferred flexible in-plane photonic devices is in preparing high quality facets. After transferring, there are three layers of different materials including silicon nanomembrane, NOA 61 and the Kapton substrate. Therefore, the traditional cleaving technique is no longer feasible. A scheme for preparing the end facets in order to test the transferred waveguides is shown in Fig. 4.4.1.1 [1, 2].
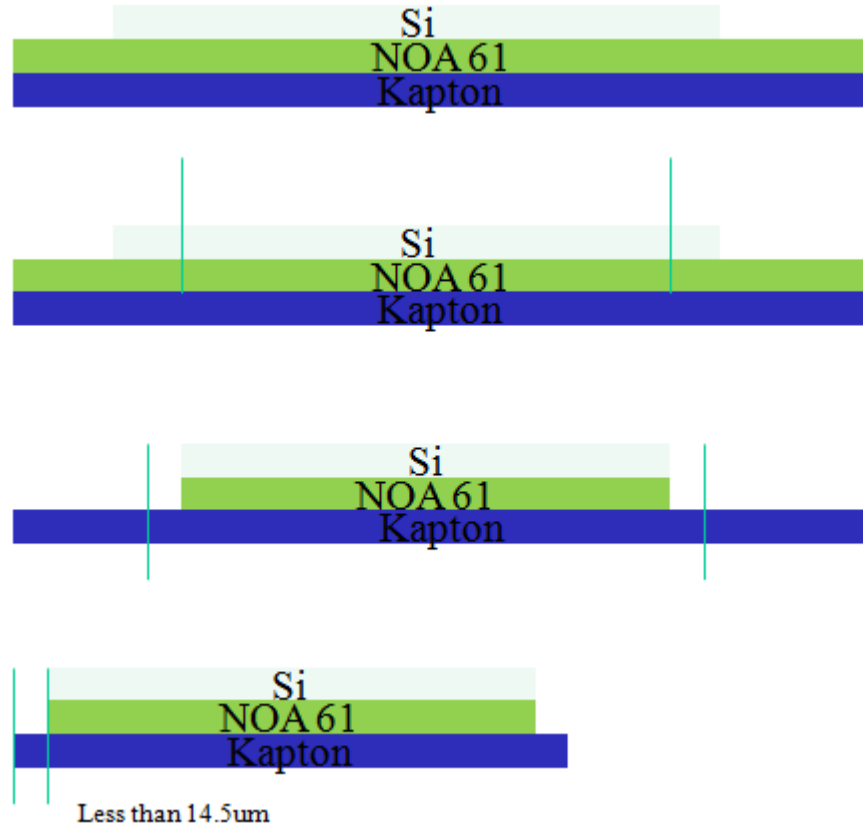
Fig. 4.4.1.1. Scheme for preparing end facets on the transferred SiNM based in-plane photonic devices [1, 2]

The flexibility of the SiNM, NOA 61 and Kapton makes it very difficult to prepare the end facets of the SiNM waveguide for light coupling. Therefore, we first use RIE (CHF_3/O_2) to etch the end of the waveguide and the NOA 61 underneath away. Then, the Kapton substrate is diced less than 14.5 μm away from the edge of waveguide in order to enable light coupling using a polarization maintaining (PM) lensed fiber with working distance of 14.5 μm and spot diameter of 2.5 μm. The cross section of the prepared facet is shown in Fig. 4.4.1.2(a). The output light from the waveguide is collected with multimode fiber with a mode diameter of 50 μm. Through a top down infrared camera, as shown in Fig. 4.4.1.2(b), the output spot can be clearly observed, indicating strong light emission. The measured insertion loss is ~25 dB for 7 mm transferred waveguide, which is about 6 dB more than the waveguide before transfer, as shown in Fig. 4.4.1.2(c). This is possibly due to the increase of facet roughness caused by the mechanic vibration during the dicing process. To measure the propagation loss of the waveguide, a structure shown in Fig. 4.4.1.2(d) is transferred. Through varying Δ*L*, the length of the waveguide can be changed by 2.6 cm. The measured loss is ~1.1 dB/cm in the region from 1530 nm to 1600 nm, which is comparable with the SOI based waveguide.
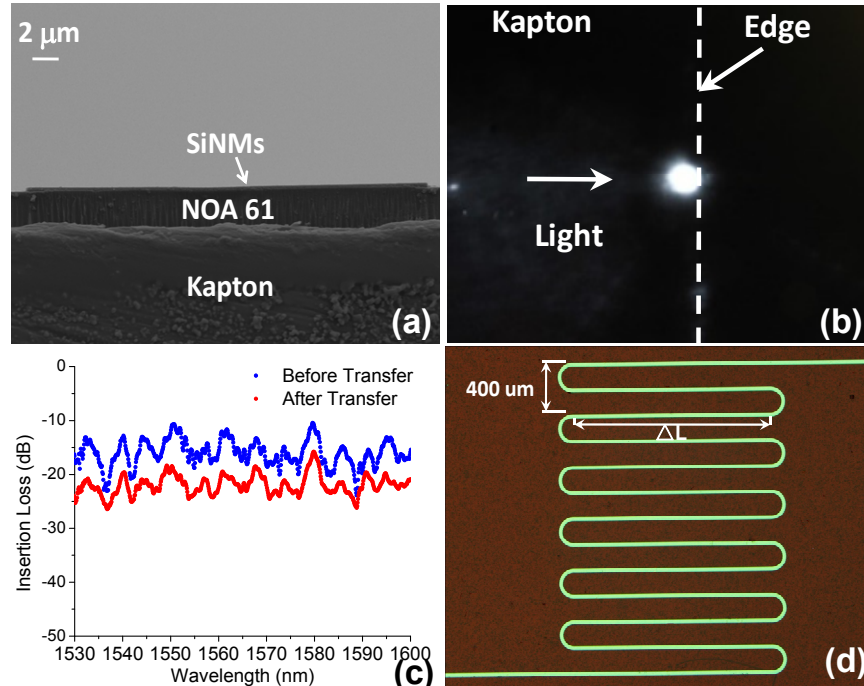
Fig. 4.4.1.2. (a) SEM image of the cross section of the waveguide after transfer. (b) The output spot captured by an topside down IR camera. (c) The insertion loss of 7mm SiNM based flexible waveguide (red) and the SOI based waveguide (blue) (d) The structure used to measure the propagation loss of the waveguide [2].

4.4.2 Subwavelength Grating (SWG) Couplers

In this program, we also developed efficient coupling structures using subwavelength periodic holes in order to couple light into the photonic devices. Such subwavelength grating (SWG) couplers are extremely crucial in order to enable practical realization of SiNM based photonic devices. In this section, we will begin by discussing our initial design, fabrication and testing on an SOI wafer, followed by extending the design and demonstration to a transferred nanomembrane. High coupling efficiencies > 40% are achievable, which will tremendously benefit several applications.

4.4.2.1 Subwavelength grating couplers on SOI

Silicon photonics has been considered a promising platform for high density integration of optoelectronic devices [72, 73]. The high index contrast between silicon and its cladding materials (air, silicon dioxide, etc.) allows for the fabrication of submicron structures such as single mode waveguides, resonators, photonic crystals, etc. However, coupling light into and out of these devices through fiber butt coupling suffers from high losses induced by the large mode and effective index mismatches between fiber and strip waveguides with submicron cross sections. The reported efficient coupling schemes include end-fire coupling and off-surface coupling [74]. The inverse taper, proposed in 2002 [75], has proven to be an effective solution for end-fire coupling. The highest coupling efficiency demonstrated so far is ~0.5 dB for transverse electric (TE) polarization [76]. The strip waveguide tip must be sufficiently narrow (e.g. 30 nm) to stimulate a delocalized mode. As a result, the height-to-width aspect ratio of the

tip is so high that the lithography becomes challenging resulting in a low yield. Furthermore, the resulting mode spot size is still much smaller than that of a single mode fiber, and a lensed fiber is needed to further ameliorate mode matching [77, 78]. In many cases, the chip needs to be diced and polished so that the distance from the nanotaper tip to the chip edge becomes ~3 μm or less [78]. These crucial requirements limit the application of inverse tapers. To overcome these limitations, a subwavelength edge coupler was proposed [79], and a 0.9 dB coupling efficiency was demonstrated experimentally [80]. We further worked on developing a high efficiency TE polarization SWG design, that enables efficient coupling into and out of photonic devices [3].

The subwavelength grating (SWG) we developed is based on a SOI comprising of a 250 nm silicon device layer and a 1μm buried oxide (BOX) layer. The grating is formed by periodically replacing parts of the silicon layer (n_{si}=3.476) with SWN, as shown in Fig. 4.4.2.1(a). Optimization of the SWG with 3D finite-difference-time-domain (FDTD) is not possible because its simulation time is prohibitively long [16c]. In this letter, an alternative model is utilized. According to effective medium theory (EMT) [81], a composite medium comprising two different materials interleaved at the subwavelength scale can be approximated as a homogenous medium with an effective refractive index between these two materials. Therefore, the SWG is equivalent to the conventional GC shown in Fig. 4.4.2.1(b). The subwavelength region is regarded as a homogeneous material with an effective index n_{sub} [82]. The uniform material is then replaced with a SWN, as shown in Fig. 4.4.2.1(c) [74].
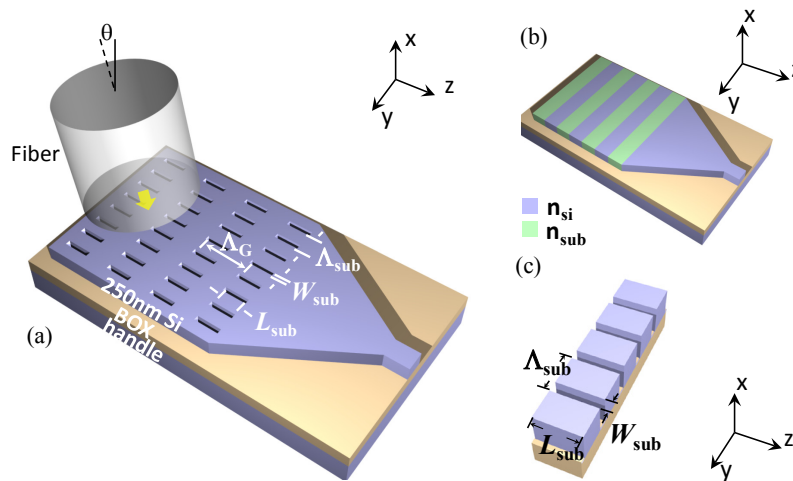

Fig. 4.4.2.1 (a) Schematic of the proposed SWG. (b) The equivalent conventional GC. The trenches are filled with SWN of refractive index n_{sub}. (c) Schematic of the SWN. The refractive index of the material can be controlled by tuning the air trench width W_{sub} and the period Λ_{sub} of the subwavelength structure[3]

To optimize the grating design, a 2D simulation package CAMFR, which is based on the eigenmode expansion technique, is utilized to search for an optimal combination of grating period Λ_G and n_{sub} giving the highest coupling efficiency to air through the SWG. The duty cycle of the grating is optimized to be 50%, and 25 periods are employed. The grating region is 10 μm wide and 17.1 μm long. These dimensions match well with the mode size of a single mode fiber
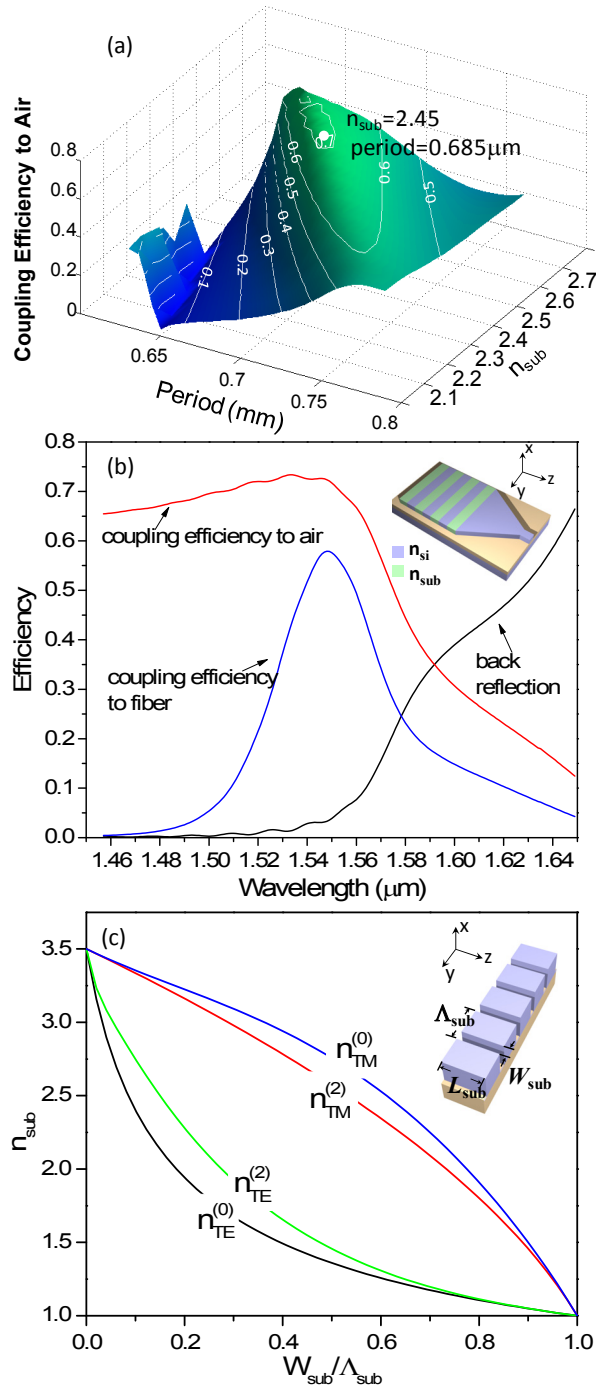
Fig. 4.4.2.2 (a) Coupling efficiency to air as a function of grating period Λ_G and the effective refractive index n_{sub} of the subwavelength structure. The highest coupling efficiency to air (white dot) is obtained when Λ_G is 0.685 μm and n_{sub} is 2.45. (b) Coupling efficiency to air (red), Coupling efficiency to fiber (blue), and back reflection (black) from the simplified structure shown in the inset. (c) Refractive index of the SWN for different filling factors, calculated by EMT with zeroth-order and second-order approximations when Λ_{sub} is 300 nm [3]

[74]. An exhaustive parameter sweep shows that the maximum coupling efficiency to air is 72% with an emitting angle of 9.4^o when $\Lambda_G = 0.685$ μm and $n_{sub} = 2.45$, as indicated in Fig. 4.4.2.2(a).

The corresponding coupling efficiency to air versus wavelength is shown in Fig. 4.4.2.2(b) (red curve). To verify the design, 2D FDTD simulations of the grating are also performed, and its results match with those obtained by CAMFR with a discrepancy within 2%. The coupling efficiency to a fiber, shown by the blue curve in Fig. 4.4.2.2(b), is evaluated by calculating the overlap integral with a Gaussian fiber mode. Since the width of the grating is much larger than its height, decoupled 3D modes can be established in the y and z directions [82]. Since the y dependent overlap integral is close to 1 [83], the overlap integral can be simplified to an integration along the z direction. The reflection back into the waveguide is around 3.8% at the wavelength of 1550 nm, as shown by the black curve in Fig. 4.4.2.2(b). The design is used for both input and output couplings. The 2D FDTD shows that the difference between input and output coupling efficiency is negligible.

Theoretically, any SWN (e.g. photonic crystals) with an effective refractive index of 2.45 may be used to "fill" the low index regions of a periodic structure, which is a grating in our case. However, as indicated in Fig. 4.4.2.2(a), the coupling efficiency heavily relies on n_{sub}, so a precise control of n_{sub} is crucial for achieving high coupling efficiency. In this letter, a thoroughly investigated 1D stratified structure is chosen so that the refractive index of the SWN can be precisely controlled [84]. As shown in Fig. 4.4.2.1(c), silicon and air slices are periodically laminated along the y direction. The guided wave propagation direction is parallel to the layers (z direction) and the electric field is perpendicular to the layers (y direction). In this configuration the refractive indices of SWN for TE and TM can be calculated through Eqs. (1) and (2) that are shown below [84]:

$$\text{TE:} \quad \frac{\sqrt{n_{si}^2 - n_{TE}^2}}{n_{si}^2} \tan\left(\frac{2\pi\sqrt{n_{si}^2 - n_{TE}^2}\,(\Lambda_{sub} - W_{sub})}{2\lambda}\right) = -\frac{\sqrt{n_{trench}^2 - n_{TE}^2}}{n_{trench}^2} \tan\left(\frac{2\pi\sqrt{n_{trench}^2 - n_{TE}^2}\,W_{sub}}{2\lambda}\right) \tag{1}$$

$$\text{TM:} \quad \sqrt{n_{si}^2 - n_{TM}^2} \tan\left(\frac{2\pi\sqrt{n_{si}^2 - n_{TM}^2}\,(\Lambda_{sub} - W_{sub})}{2\lambda}\right) = -\sqrt{n_{trench}^2 - n_{TM}^2} \tan\left(\frac{2\pi\sqrt{n_{trench}^2 - n_{TM}^2}\,W_{sub}}{2\lambda}\right) \tag{2}$$

where n_{TE} and n_{TM} are the refractive indices of SWN for TE and TM polarizations, respectively. n_{si} and n_{trench} are the refractive indices of the silicon and the material in the holes, respectively. In our design, the holes are filled with air (n_{trench}=1). Λ_{sub} is the period of the SWN, and W_{sub} is the width of the rectangular air holes. The filling factor of the SWN is defined as $f_{sub} = W_{sub}/\Lambda_{sub}$. As the transcendental Eq. (1) and Eq. (2) do not have explicit analytical solution, polynomial expansion is exploited to approximate the tangent function. The n_{sub} versus f_{sub} based on zeroth-order and second-order approximations are illustrated in Fig. 4.4.2.2(c). The zeroth-order approximations are accurate only under the condition that along any arbitrary direction, the change in the electromagnetic field within a distance of Λ_{sub} is sufficiently small[84]. The condition can be formulated as $2\pi n_{eff}\Lambda_{sub}/\lambda \ll 1$. Here, n_{eff} is the mode effective index in the silicon slab waveguide with 250 nm thickness. For TE polarization, the corresponding f_{sub} for n_{sub}=2.45

is ~0.09 according to the first-order approximation. The smallest W_{sub} that can be fabricated is ~40 nm. Thus, Λ_{sub} becomes close to the wavelength inside the slab waveguide. The zeroth-order approximations, therefore, are no longer applicable [85]. Including second-order expansion terms can improve the accuracy of the approximation as long as the permittivity of one material is not vastly different from the other [84]. Fig. 4.4.2.2(c) confirms that the first-order approximation underestimates the refractive index by 0.33 when the filling factor f_{sub} is 20%. Thus, the second-order approximation is used in this work. Considering fabrication yield and repeatability limitations, the trench width is fixed to 80 nm with a corresponding Λ_{sub} of 388 nm.

The designed GC is fabricated using electron beam lithography (EBL) and RIE. The top view and the cross view scanning electron microscopy (SEM) images of the fabricated grating are shown in Fig. 4.4.2.3. A magnified view of the air trenches is shown in the inset of Fig. 4.4.2.3(a).
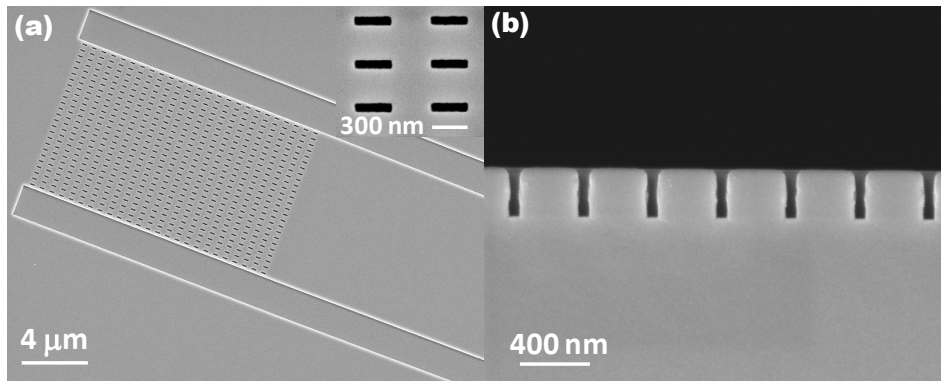

Fig. 4.4.2.3 (a) SEM images of the fabricated GC. Inset: the magnified view of the air trenches. (b) the cross section of the rectangular air holes [3]

The GC is characterized by measuring the fiber-to-waveguide-to-fiber insertion loss. The measurement setup is shown in Fig. 4.4.2.4(a). The input and output fibers are mounted on two 10° wedges, which are in turn mounted on rotating stages. The tilt angle can be adjusted from 0° ~ 20°. For this design, both the input and output fibers are tilted ~9.4^o from normal incidence. The fiber positions are controlled by two xyz stages. A camera is mounted at a 45° angle to visually aid alignment. The input fiber is a polarization maintaining fiber (PMF), and the polarization is controlled via a polarization controller (PC). Light is coupled into an 8 mm long, 2.5 μm wide waveguide via a pair of grating couplers. Since the fundamental mode contains most of the power, the existence of higher order modes has negligible effects on the testing results. A pair of linear waveguide tapers, each with a length of 500 μm, is utilized to bridge the 10 μm wide grating region to the waveguide. The coupling efficiency is extracted assuming equal coupling efficiencies for both gratings. The transmission spectrum, as shown in Fig. 4.4.2.4(b), is measured with a broad band amplified spontaneous emission (ASE) source. The peak efficiency is measured to be 59% (-2.29 dB). The peak wavelength shifts to 1551.6 nm possibly due to fabrication errors. The 1 dB and 3 dB bandwidths are 32 nm and 60 nm,
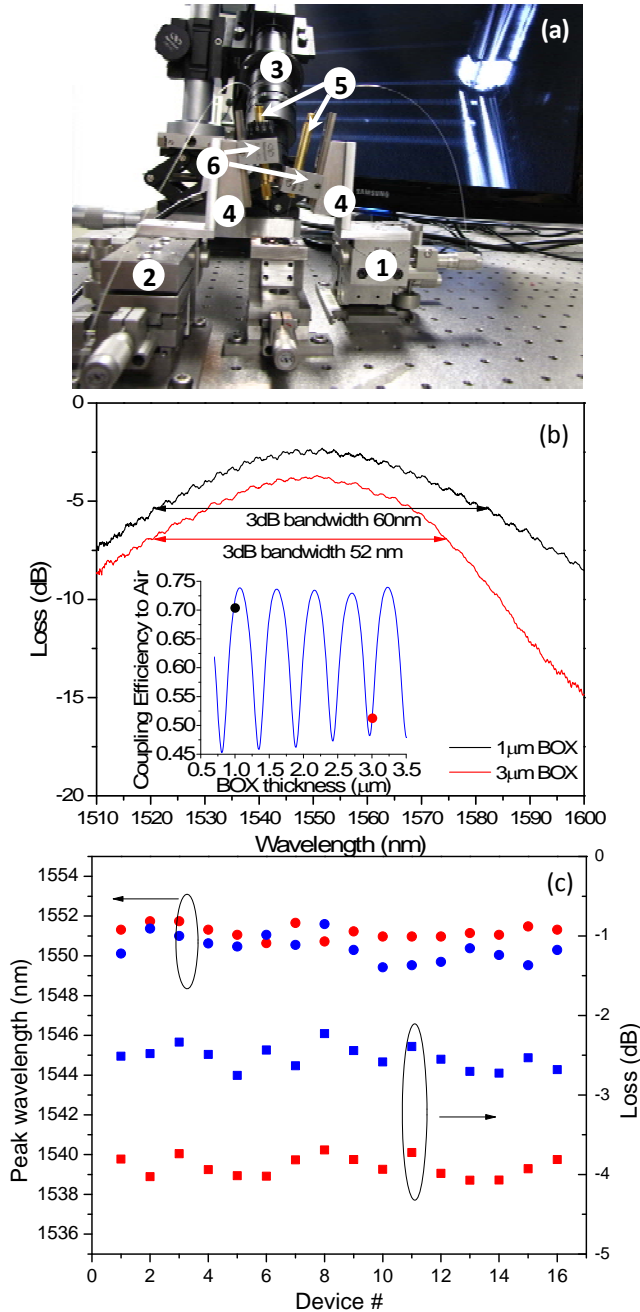
Fig. 4.4.2.4 (a) Testing set up. 1. tilting stage; 2. xyz stage; 3. 45° tilted camera; 4. 10° wedges; 5. fiber chuck; 6. chuck holder; (b) The measured transmission of the grating fabricated on the SOI with 1 μm BOX (black) and 3 μm BOX (red). Inset: Upward power efficiency vs. BOX thickness. (c) The peak wavelengths (dots) and the coupling losses (squares) of the fabricated 32 grating pairs on SOI with 1μm (blue) and 3μm (red) BOXs [3]

respectively. The Fabry-Perot fringes near the peak wavelength are ~0.3 dB in magnitude, indicating low back reflection. It is much smaller than conventional through-etched GC due to the SWN not only reducing the Fresnel reflection and also functioning as a destructive interference enhancer to reduce the reflection at the interface of the grating and free space. The efficiency increases 1.73 times (from 34% to 59%), and the bandwidth increases 1.5 times (from

40 nm to 60 nm) compared to the previously reported TE polarized SWG on SOI. The performance enhancement is due to the fact that the refractive index of the SWN is more precisely controlled compared to the previously reported GC. The bandwidth can be further extended through increasing the tilt angle [86]. In this manner, back reflections may also be further suppressed. The high efficiency of the grating also benefits from destructive interference in the BOX layer. Due to the interference effects from the downward diffracted light beam, the waveguide to free space coupling efficiency has a strong periodic dependence on the BOX thickness. The coupling efficiency could vary by as much as 30%, as illustrated in the inset of Fig. 4.4.2.4(b).

The commercially available 1 μm BOX is close to the optimum thickness yielding the highest upward power efficiency. For comparison, the same design is also fabricated on an SOI with a 3 μm BOX, which is close to the lowest point in the power efficiency curve shown in the inset of Fig. 4.4.2.4(b). For the 3 μm BOX SWG, the measured peak efficiency is 42.8% (-3.69 dB) at 1550.7 nm with 1 dB and 3 dB bandwidths of 28 nm and 52 nm, respectively. As expected, the performance is worse than that of 1 μm BOX but is still acceptable compared to recently reported gratings. To verify fabrication repeatability, 32 grating pairs, with 16 pairs on each of the 1 μm and the 3 μm BOX chips are fabricated. The measured peak wavelengths and coupling efficiencies are shown in Fig. 4.4.2.4(c). Peak wavelength and power vary by 1.1 nm and 0.38 dB for 3 μm BOX devices and 2.2 nm and 0.52 dB for 1 μm BOX devices, demonstrating acceptable consistency.

4.4.2.2 Subwavelength grating couplers on transferred Silicon Nanomembrane

For successful in-plane SiNM photonic devices, one needs to overcome the challenges of intricate device development and light coupling on foreign substrates. The former has been addressed with novel SiNM transfer techniques [2, 64] to enable development of large aspect ratio SiNM photonic devices on foreign substrates. However, the latter still remains a challenge to overcome. Unlike conventional SOI based photonic devices, wherein facet preparation techniques have matured significantly, such techniques are improper for SiNM based photonic devices due to the soft polymer cladding underneath the semiconductor membrane. Moreover, if the integration is performed on a flexible substrate, the problem becomes even more severe.

To our knowledge, we report the first subwavelength grating coupler (SWG) to achieve low-loss coupling into in-plane SiNM-based photonic devices. Utilizing the design concepts in section 4.4.2.1, we designed SWG couplers for transferred NMs.

The SWG consists of an array of periodic rectangular air holes with subwavelength dimensions formed in a 250 nm thick SiNM transferred onto a glass substrate with an SU-8 bottom cladding layer, as shown in Fig. 4.4.2.5 [6].
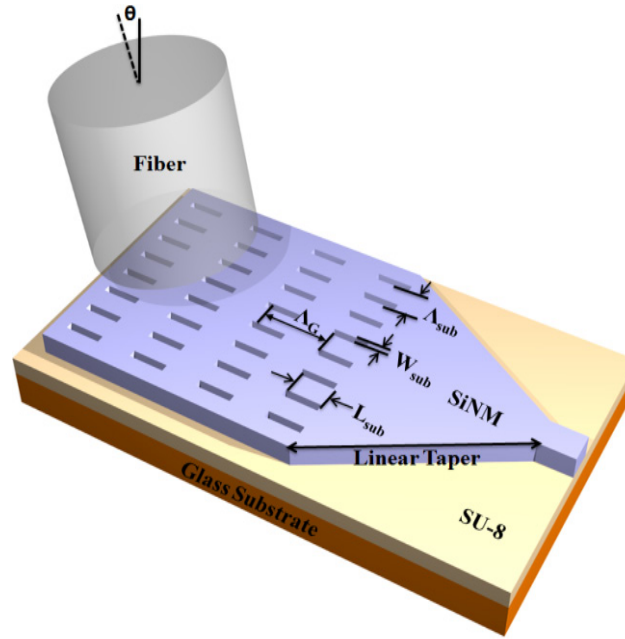
Fig. 4.4.2.5. Schematic illustration of the subwavelength grating (SWG) coupler on a SiNM transferred onto a glass substrate. L_{sub}, W_{sub}, Λ_{sub}, Λ_G, and θ denote the hole length, the hole width, the hole period, the grating period, and the angle of the fiber with respect to the surface normal, respectively [6].

Four grating parameters, namely, the trench length (L_{sub}), the hole width (W_{sub}), the hole period (Λ_{sub}), and the grating period (Λ_G) define the SWG. In order to simplify the calculations for an optimum design, an effective index approximation method, such as the Effective Material Theory (EMT), is utilized to approximate the subwavelength section as a uniform material with refractive index n_{sub}. An open source simulation package CAMFR, which is based on eigenmode expansion, is utilized to search for a best combination of grating period Λ_G and n_{sub} in order to obtain the highest power efficiency around 1550 nm. In our design, the filling factor of the grating is fixed at 50%. The calculated optimum Λ_G and n_{sub} are Λ_G=0.690 µm and n_{sub} =2.45, respectively, corresponding to L_{sub}=0.345 µm, W_{sub}=0.090 µm, and Λ_{sub}=0.390 µm.

Fabrication is performed on a 2cm x 2cm 250nm thick SiNM transferred onto a 1mm thick glass substrate, with an 8.22µm thick SU-8 bottom cladding layer, as shown in Fig. 4.4.2.6(a). The SiNM is transferred using a SOI bonding and handle wafer removal method similar to that described in section 4.3.4. In order to transfer the SiNM onto the 1mm thick glass substrate, a pre-cleaned 2 cm by 2 cm SOI chip (250 nm single crystal silicon layer, 3 µm buried oxide (BOX) layer and 500 µm handle wafer) and a 2.5 cm by 2.5 cm glass slide are spin coated with 5 µm thick SU-8 layer. After pre-baking, the SOI chip is brought into contact with the glass slide and pressure is applied. Next, the sample is heated to the glass transition temperature of SU-8 to enable reflow and removal of trapped air pockets. Then, ultra violet (UV) light is illuminated through the glass slide to cure SU-8. Post exposure baking is performed to complete cross linking. Following this, the 500 µm silicon handle is removed by polishing and deep silicon etching, with the 3 µm BOX layer serving as a stopping layer for the silicon etching process. The remaining 3µm BOX is then selectively etched away using hydrofluoric acid, thus leaving a 250

nm silicon device layer with the SU-8 bottom cladding layer on the glass substrate. Twenty five periods of the designed SWG grating coupler are fabricated at the input and the output of an 8 mm long, 2.5 μm wide SiNM waveguide using electron beam lithography (JEOL JBX-6000). A pair of linear waveguide tapers, each with a length of 500 μm, is incorporated to bridge the 10 μm wide grating region to the waveguide. An SEM of the fabricated SiNM SWG coupler is shown in Fig. 4.4.2.6(b). A schematic of the fabricated structure is shown in the inset.
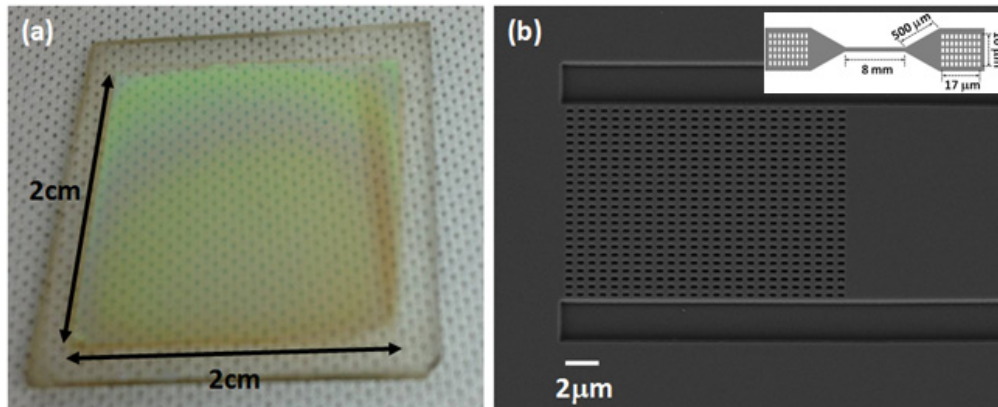
Fig. 4.4.2.6 (a) Optical microscope image of a 2cm x 2cm 250nm thick SiNM transferred onto a 1mm thick glass substrate. The thickness of the SU-8 bottom cladding layer is measured to be 8.22μm, (b) Scanning electron microscope (SEM) image of the fabricated subwavelength grating coupler (SWG) on the transferred SiNM. A schematic of the fabricated structure is shown in the inset [6].

Since the SU-8 layer thickness cannot be controlled accurately using our custom-made bonding setup, the post fabrication measured SU-8 layer thickness of 8.22 μm is used to simulate the grating characteristics. Calculations are performed for TE polarization since that is the polarization of interest for several interesting photonic crystal waveguide and other active devices we are working on. The calculated back reflection (black curve), coupling efficiency to air (red curve), and coupling efficiency into a single mode fiber tilted at a 10° angle with respect to the normal (blue curve) is shown as a function of wavelength in Fig. 4.4.2.7. At a wavelength of 1550nm, a peak upward power efficiency of 54 %, corresponding to a 42 % coupling efficiency into a single mode fiber, is achieved.

Our fabricated grating coupler is characterized by measuring the fiber-to-waveguide-to-fiber insertion loss. The input and output fibers are mounted on two 10° wedges, whose position with respect to the gratings can be controlled using two xyz stages. The input fiber is a polarization maintaining (PM) fiber whose polarization is controlled via a waveplate-based polarization controller (PC). The output fiber is a conventional single mode fiber with a core diameter of 9 μm. The tilt angle can be adjusted from $0^o \sim 20^o$. For this design, both the input and output fibers are tilted ~9.4^o from normal incidence. TE polarized light from a broadband amplified spontaneous emission (ASE) source is coupled into the 8 mm long, 2.5 μm wide SiNM waveguide via the grating couplers. The transmission through the grating pair and the SiNM waveguide is measured on an optical spectrum analyzer (OSA). The coupling efficiency is

extracted assuming equal coupling efficiencies for both gratings. Fig. 4.4.2.8 shows the measured transmission spectrum for a single grating.
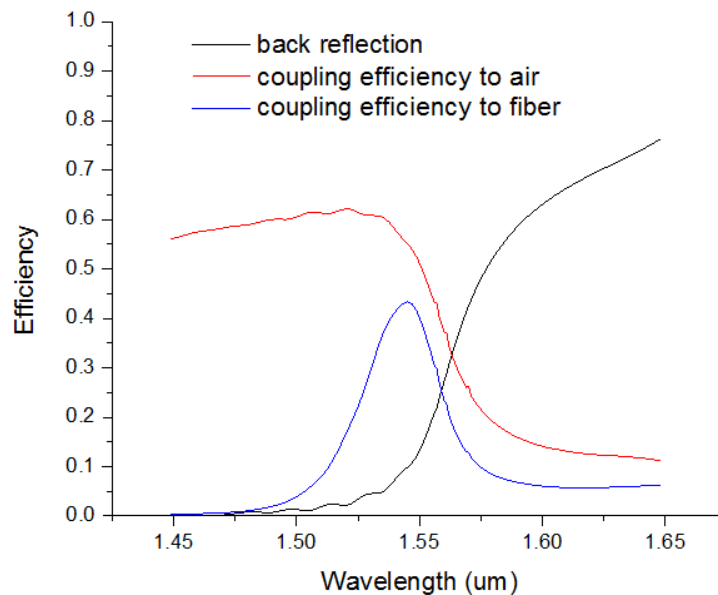

Fig. 4.4.2.7. Simulated back reflection (black), coupling efficiency to air (red) and coupling efficiency to a fiber positioned at 10° with respect to surface normal of the designed SWG coupler (blue) as a function of wavelength of operation. A peak fiber coupling efficiency of 42 % is achieved at a wavelength of 1549nm. An SU-8 layer thickness of 8.22 μm is used in the simulation [6].

The peak efficiency is measured to be 39.17 % (-4.07 dB) at 1555.56 nm. Measurements are also performed on a set of 5 pairs of grating couplers, and a maximum deviation in peak efficiency of -0.26dB is obtained, thus showing a high uniformity in performance. The 1 dB and 3 dB bandwidths are measured to be 29 nm and 57 nm, respectively. The shift in the peak wavelength from the design value could possibly be due to fabrication errors which subsequently change n_{sub} from its designed value.

It should be noted, however, that the overall coupling efficiency is strongly affected by the thickness of the underlying SU-8 cladding layer. This is due to the fact that the constructive and destructive interference between the upward diffracted beam and the downward diffracted beam reflected upwards at the SU-8/glass interface is a periodic function of the cladding layer thickness. Due to the absence of a precise SiNM bonding tool, the SU-8 layer thickness cannot be controlled precisely. However, by utilizing a specialized bonding tool with a pressure monitoring system for the SiNM transfer process, the SU-8 layer thickness can be controlled accurately.
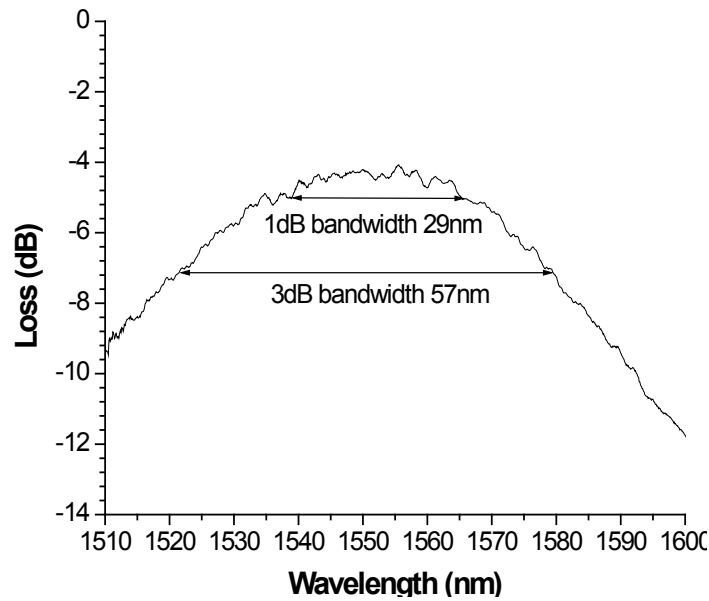
Fig. 4.4.2.8 Measured transmission spectrum of the grating coupler fabricated on SiNM on glass substrate. Peak efficiency of 39.17% (-4.07dB) is obtained at a wavelength of 1555.56nm. The 1 dB and 3 dB bandwidths are 29 nm and 57 nm, respectively [6].

Fig. 4.4.2.9 is a simulation result showing the effect of changing the SU-8 layer thickness from 7 μm to 9 μm on the coupling efficiency to air. It can be seen that the efficiency fluctuates between 53% to 67% within 0.25 μm of SU-8 layer thickness variation. Our measurement point is indicated as a red dot in the figure. Better control of the SU-8 layer thickness will further increase the efficiency. Nevertheless, the 'worst-case' scenario of 53% coupling efficiency to air is still better than other demonstrated coupling methods [64, 2].
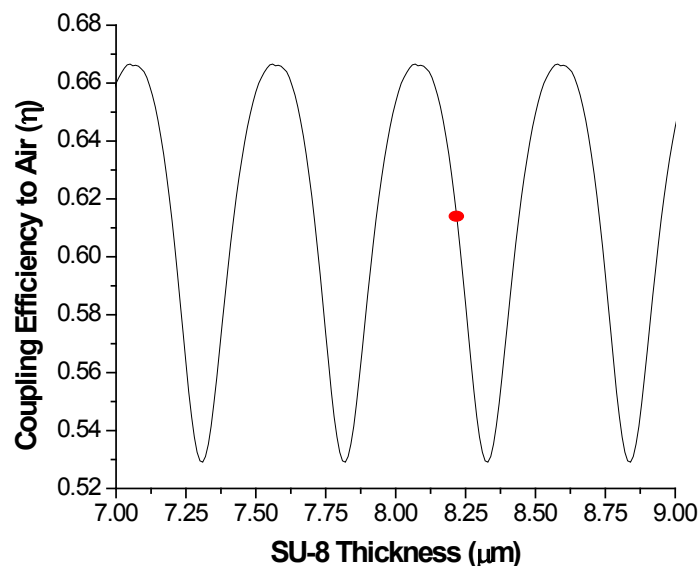

Fig. 4.4.2.9. Simulation showing the effect of SU-8 layer thickness variation from 7μm to 9μm on the coupling efficiency to air. A periodic efficiency fluctuation between 53% to 67% is produced. The red dot indicates our fabricated result [6].

We then utilized the grating couplers to fabricated and test SiNM based photonic devices. Since propagation loss is a deterministic factor to investigate whether a material is suitable for photonic applications, a cut-back method is first used to measure the propagation loss of single mode waveguides fabricated on transferred SiNMs. Then, a 1× 16 splitter, covering an area of 0.5 mm × 6 mm, is fabricated to demonstrate that the transferred SiNM is capable of accommodating large scale photonic circuits. To determine the propagation loss, 500 nm wide single mode waveguides with different lengths (0.5 cm, 1.5 cm, and 2.5 cm) are fabricated. Subwavelength grating (SWG) couplers are utilized for input and output light coupling. 10 μm wide, 17 μm long SWG couplers are connected to the single mode waveguide through a 500 μm adiabatic taper. A set up described in section 4.3.3 is exploited for measurements. Light from a broadband amplified spontaneous emission (ASE) light source is transverse-electric (TE) polarized and coupled into the single-mode waveguide via a 10° tilted polarization maintaining fiber. The output light is collected by a single mode fiber tilted at the same angle as the input fiber, and analyzed in an optical spectrum analyzer. The results are presented in Fig. 4.4.2.10. The average propagation loss is about 4.3 dB/cm in the wavelength range from 1535 nm to 1565 nm for waveguides fabricated on transferred SiNM, while the value is around 3.1 dB/cm for SOI based single mode waveguides with the same dimensions. The higher loss in the SiNM waveguides is possibly due to the increase of the roughness. The atomic force microscopy (AFM) images shown in the inset of Fig. 4.4.2.10 confirm that the surface roughness of the transferred SiNM increased to 0.522 nm, while it is 0.128 nm for SOI.
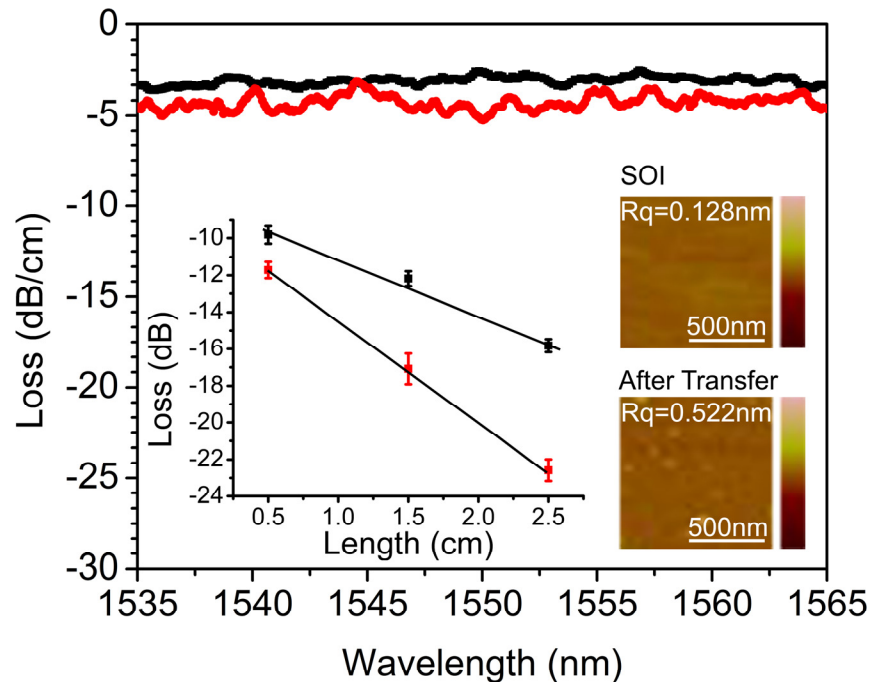

Fig. 4.4.2.10. The propagation loss of single mode waveguides on the transferred SiNM (red) and on SOI (black). Left inset: the slope loss at 1550nm. Right inset: the top surface roughness of the SOI and the SiNM after transfer [4].

Energy dispersion spectrometry shows rich carbon, hydrogen, and oxygen elements in the white spots shown in the AFM images indicating that these spots are possibly the polymer residues from the DRIE process. Since the ICP power is kept low, the polymer deposited in the deposition step cannot be stripped completely during the silicon etching step, causing the increase of roughness. However, the size of the polymer spots is small so that the effects on propagation loss are limited.

4.5 Silicon Nanomembrane Based Photonic Devices on Other Substrates

4.5.1 SiNM based 1x16 MMI Power Splitter

To demonstrate the feasibility of fabricating photonic devices on the transferred SiNM, a 1x4 multimode interference (MMI) optical beam splitter is designed for air (top) and SU-8 (bottom) cladding. The length and width of the multimode regions are 119.4μm and 16 μm, respectively. The input and access waveguides are both 2.5 μm wide to ensure low insertion loss and high uniformity [4]. A 1×16 splitter is formed by cascading five 1×4 MMIs together. Subwavelength grating couplers are again used for input and output light coupling. The optical microscope image of the fabricated MMI is shown in Fig. 4.5.1.1(a). Figs. 4.5.1.1(b~f) show the details of each section of the splitter. To clearly resolve the individual output spots using a 45° tilted infrared camera, a fanout design is used to separate the 16 MMI output channels by 30 μm. A tunable laser with a wavelength precision of 0.001nm is exploited to scan the working wavelength of the splitter. Figure 4.5.1.1(g) shows the infrared image of the 16 output spots. A uniformity of 0.96dB is obtained at 1545.60 nm across the 16 output channels, while the insertion loss for the device is 0.56 dB. The uniformity and the insertion loss are determined by using a single mode fiber to scan the output power of each output channel. The performance is quite acceptable and is comparable with SOI based MMI splitters.
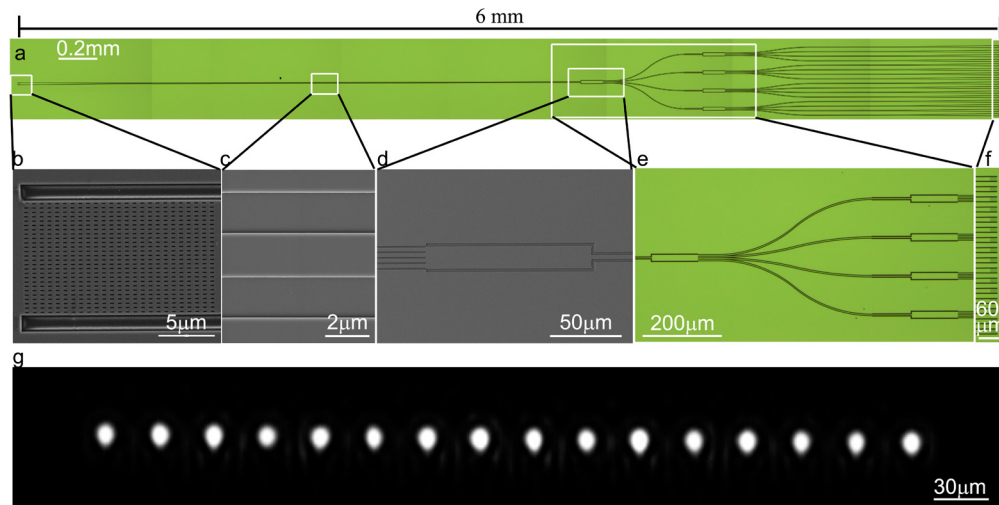

Fig. 4.5.1.1 Fabricated two-level cascaded 1 × 16 MMI. a. optical microscope image of the 1 × 16 MMI. b. SEM picture of the subwavelength grating coupler for in and output coupling. c.SEM picture of the 2μm wide multimode waveguide. d. SEM picture of the 1 × 4 MMI. e. cascaded 1 × 4 MMI. f. output subwavelength grating array, consisting of 16 couplers. g. The infrared image of the sixteen output spots captured with a tilted camera [4].

4.5.2 Photonic Crystal Waveguide TTD on transferred SiNM

In this work, a slow-light photonic crystal waveguide (PCW), with a period (L) of 405 nm, and a hole diameter (d) 190 nm was patterned on the transferred SiNM using conventional e-beam lithography. An SEM picture of the fabricated PCW is shown in Fig. 4.5.2.1(a). SWG couplers are utilized to couple light into and out of the waveguides. The SWG couplers are fabricated simultaneously together with the photonic waveguides. An SEM picture of the SWG coupler is shown in Fig. 4.5.2.1(b).
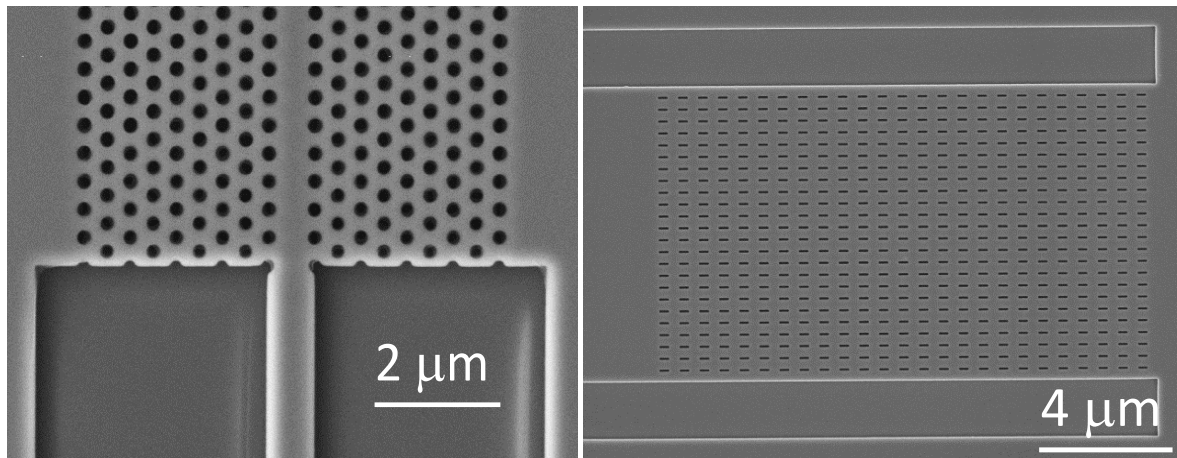

Fig. 4.5.2.1. (a-b) SEM images of fabricated PCW and SWG,

A Fourier transform interferometer is designed and fabricated in order to accurately measure the group index of the fabricated PCWs. A microscope image of the interferometer is shown in Fig. 4.5.2.2. The interferometer consists of a signal arm (S) consisting of 100 μm of the designed PCW; a reference arm (R) consisting of 5.256 mm of a reference strip waveguide; and an interference arm (I) the combines the R and S signals using a Y-splitter. Using the method outlined in ref [7], we measure the group index of the PCW. Fig. 4.5.2.3 shows the measured transmission spectrum from the S (blue), and the I (black) arms. The calculated group index is shown as red data points. Group index up to 28.5 is measured on the SiNM based PCWs. Thus, using our scheme, we have successfully demonstrated the idea of the development and working of intricate photonic devices on foreign substrates. Moreover, SWGs prove to be an ideal packaging tool for such devices.
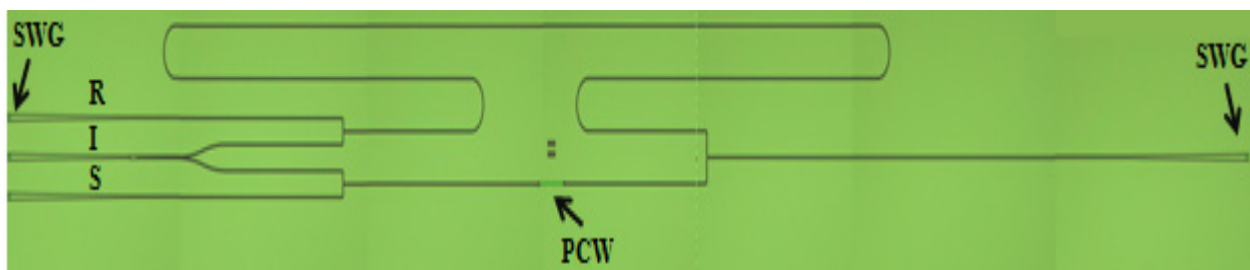

Fig. 4.5.2.2 Optical microscope image of the fabricated Fourier transform interferometer on SiNM: glass,
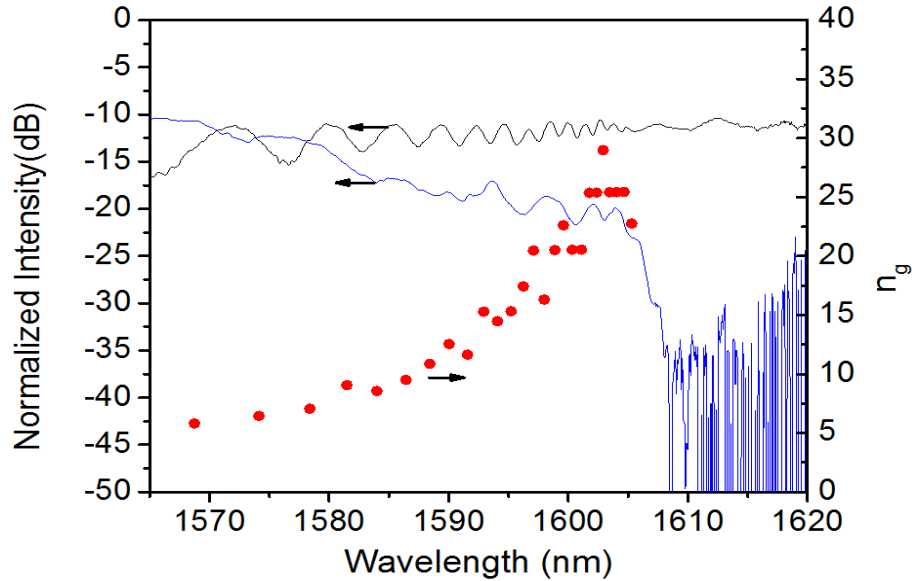
Fig. 4.5.2.3 Measured transmission spectrum from S (blue) and I (black) channels. Calculated group index is shown as red data points

4.5.3 SiNM based Photonic Devices on Flexible Substrates

Based on the achievements above, we developed and demonstrated photonic devices on flexible substrates for the first time to our knowledge. In order to demonstrate the proof-of-concept, we developed a flexible photonic crystal microcavity device, and demonstrated sensing capability. Fig. 4.5.3.1 shows the schematic of the process flow for developing flexible SiNM based devices.
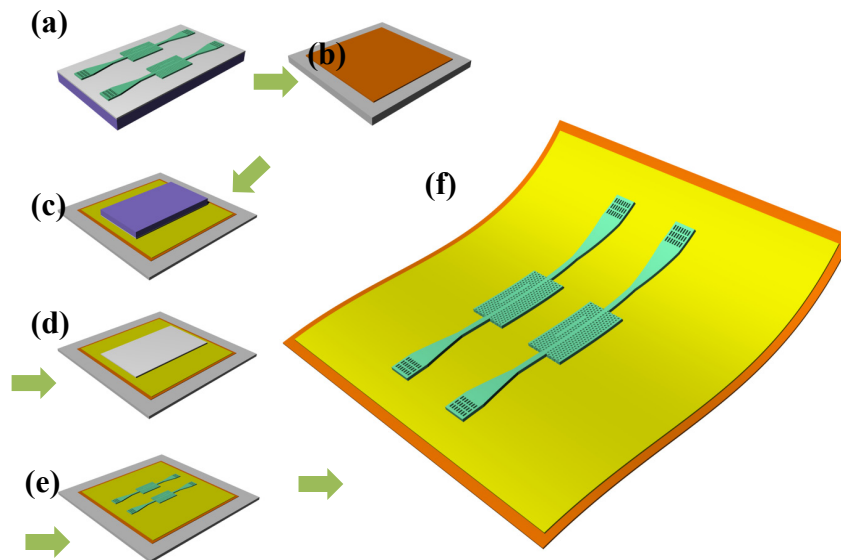

Fig. 4.5.3.1 Transfer process. a. Pattern L13 photonic crystal microcavity. b. Mount kapton film on top of a silicon chip. c. Bonding. d. Using polishing and deep reactive ion etching to remove the silicon handle. e. Remove box layer. f. Peel up Kapton film

The L13 photonic crystal micro cavity is fabricated on a Uni-bond silicon-on-insulator wafer with a 250 nm top silicon layer and 3 μm buried oxide layer. Photonic crystal waveguides, photonic crystal couplers and strip waveguides are patterned in one step using a JEOL JBX-6000FS electron-beam lithography system followed by reactive ion etching, as shown in Fig.4.5.3.1(a). The Kapton film is cleaned with Acetone and Methanol, and dried with nitrogen. To simplify the following process, the Kapton film is mounted on a rigid substrate, such as glass slides and silicon chips, as shown in Fig. 4.5.3.1(b).

A 5 μm thick SU-8 layer is spun on the SOI chip and also on the Kapton film and soft baked at 95 ^{o}C to evaporate the solvent. Then, the SOI chip is put upside down on the Kapton and placed in an oven at 65 ^{o}C for 20 mins without applying any pressure. The glass transition temperature of the non-cross-linked SU-8 is 64 ^{o}C, and at the glass transition temperature or above, SU-8 exhibits excellent self-planarization, which minimizes the edge bead effect as well as other thickness variations. Since both of the Kapton and the SOI are not transparent in the UV region, the SU-8 layer cannot be cured in an ordinary way. This problem can be solved by curing the SU-8 first and heat the sample up to glass transition temperature ($\sim$ 180 ^{o}C, depends on different crosslink level) to let the SU-8 reflow. Since the materials involved have quite different coefficients of thermal expansion, the stack could be cracked during the bonding thermal cycle with such a high temperature. As the crosslink of SU-8 relies on the generation of acid upon UV exposure as a result of protolysis of triarylsulfoniumhexafluorantimonium, the cationic photointiator, we come up with this idea of bringing one layer of cured SU-8 and one layer of uncured SU-8 together. The cured SU-8 will provide the acid and the uncured SU-8 serves as a soft layer which makes bonding with simple set up possible. The UV exposure dose is around 75mJ/cm^{2}.Pressure is applied afterwards through a home-made bonder. The sample is kept in a 90°C vacuum oven for 20 hours to allow for polymer to reflow and to squeeze out the trapped air bubbles.

After bonding, the silicon handle is removed by DRIE, as shown in Fig. 4.5.3.1(d). Since DRIE generates heat at a high rate, the carrier wafer on which the sample sits, is kept at $\sim$ 10 ^{o}C by flowing Helium underneath. However, the thermal conductivities of SU-8 and glass slides are merely 0.2 W/mK and 0.96 W/mK, respectively, and thus the heat generated by the etching process cannot be dissipated fast enough. Consequently, a significant temperature gradient builds up between the top surface and the glass slide, subjecting the sample to cracking. The mismatch of the coefficients of thermal expansion (CTE) further aggravates the thermal problem. To control the thermal budget, the silicon handle is mechanically polished down to ~100 μm prior to DRIE to shorten the etching time. The etching recipe is also carefully modified to accommodate the thermal requirements. The conventional Bosch process for DRIE contains three steps: polymer deposition, polymer etching, and silicon etching. The polymer deposition time is set to 5 s to protect the perimeter of the membrane, because the charges accumulated on the glass surface bend the electric field and etch silicon and SU-8 from the side, possibly causing undercut. The anisotropic polymer etching step is skipped in this application because the quality of the

perimeter is not important. The polymer is removed during the silicon etching step. The inductively coupled plasma (ICP) power is carefully tuned to keep it slightly above the threshold of maintaining plasma to reduce the heat generation rate to match the heat dissipation rate. However, this adjustment sacrifices the etch rate. To compensate it, a long silicon etching time of 30 s is used in each cycle. The silicon etch rate of this recipe is around 2.7 µm/cycle. Besides, the recipe has a high selectivity (~80) of oxide to silicon, meaning the 3 µm BOX can be used as a stopping layer to protect the SiNM underneath, and it can be removed by dropping hydrofluoric (HF) acid on its top. The surface tension of the silicon dioxide constrains the solution within the SiNM without flowing over. The drawback is that etching speed could fall as the HF concentration decreases. Thus, a few more drops of HF needs to be added to maintain necessary HF concentration. The cartoon showing the sample after removing the BOX layer is in Fig. 1e. Finally, the Kapton can be peeled up from the rigid handle together with the modulator on top, as shown in Fig. 4.5.3.1(f).The SEM pictures of the transferred L13 devices are shown in Fig. 4.5.3.2.
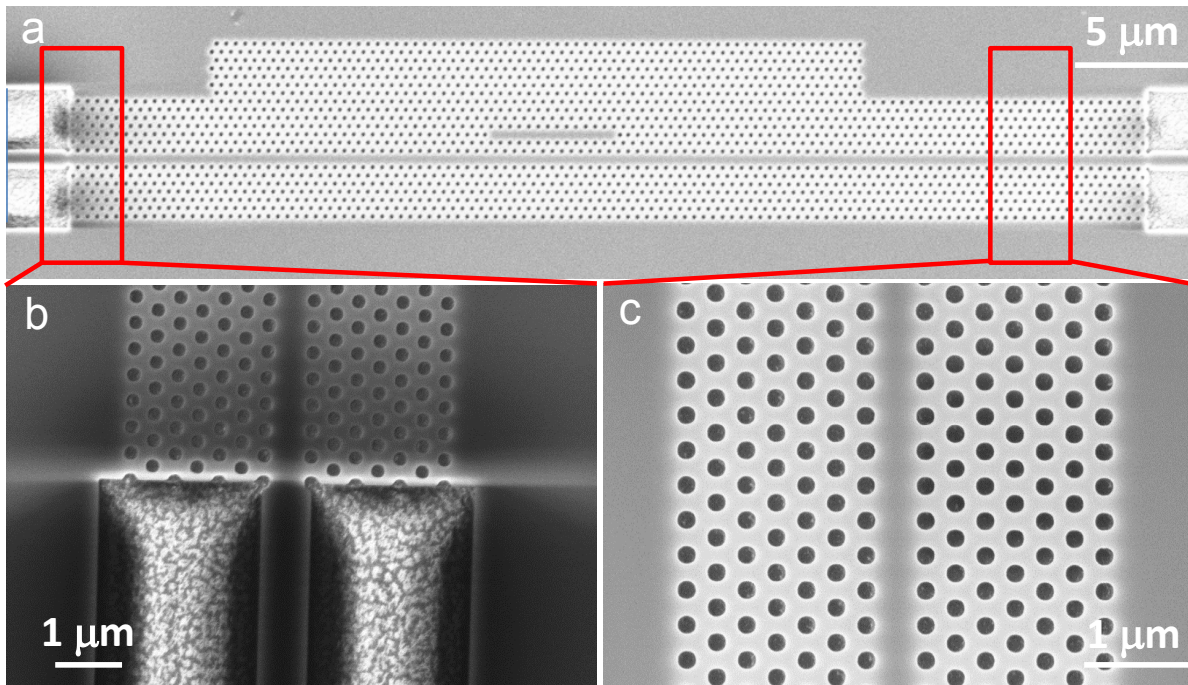

Fig.4.5.3.2 SEM pictures of (a) the transferred L13 device and (b)(c) different sections of the transferred devices

Next, we performed chemical sensing using the developed devices in order to demonstrate the working of SiNM based devices. Fig. 4.5.3.3 shows the resonance shift $\Delta\lambda$ when water (n=1.33) and glycerol (n=1.47) are applied. The change of refractive index causes a shift $\Delta\lambda$ of 9.91nm, corresponding to a sensitivity of 70.8 nm/RIU (RIU-refractive index unit). The sensitivity is comparable to the devices demonstrated on SOI.
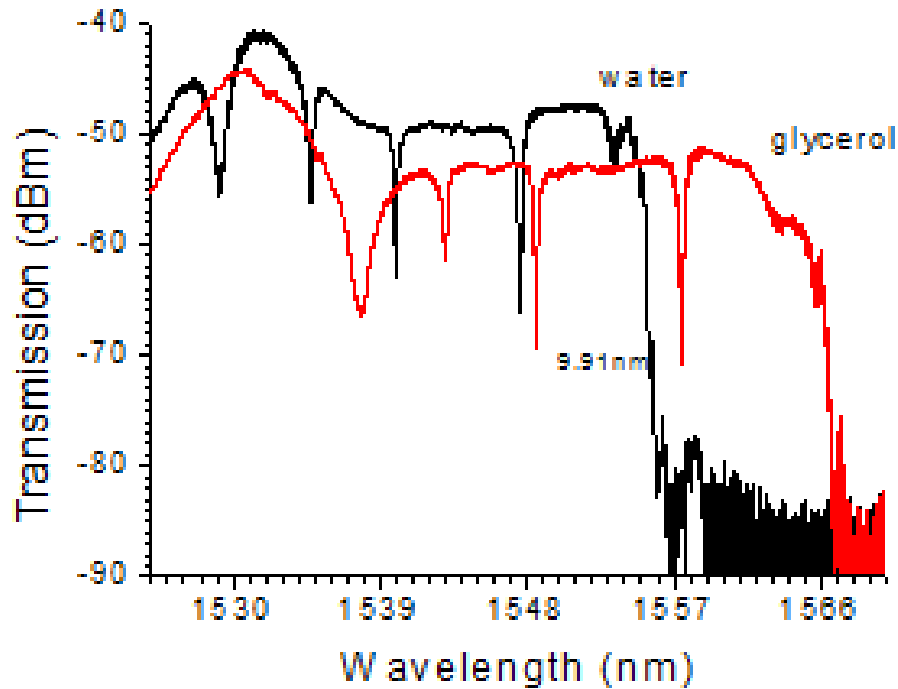
Fig. 4.5.3.3 the transmission curves when water (black) and glycerol (red) are applied

To investigate the sensor performance on a curved surface, the kapton is bended with a radius of ~7cm, as shown in Fig. 4.5.3.4(a) and 4.5.3.4(b). The resonance peak shifted 1.32 nm [Fig. 4.5.3.4(c)], which is possibly due to the bending induced elongation of the cavity.
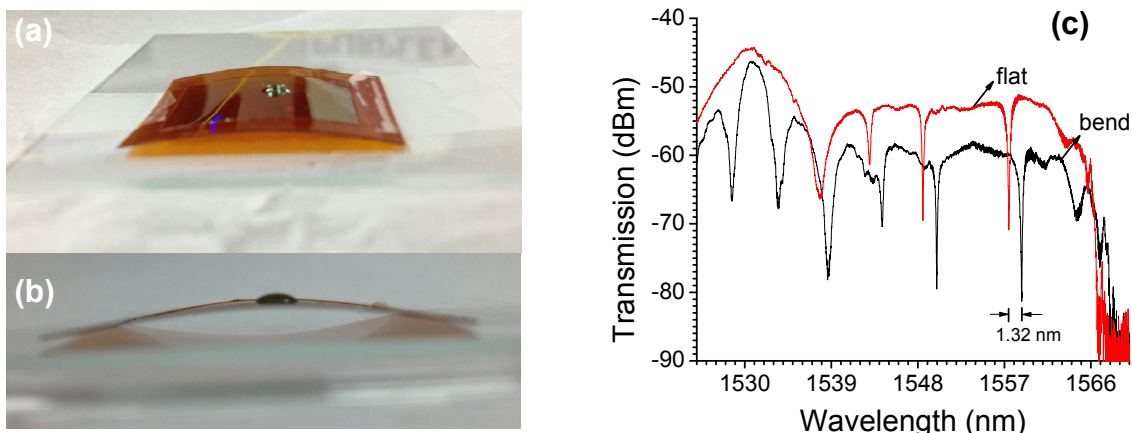

Fig. 4.5.3.4 (a) tilted view and (b) side view of the bended kapton film (bending radius is around 7cm). (c) the resonance shift.

4.6 Ink-Jet Printing of Phased Array Antenna

In this task, we designed an S-band Phased Array Antenna communication system that can be used for surface-to-air, as well as surface-to-satellite and GPS applications.

4.6.1 Design of microstrip lines, coplanar waveguides and patch antenna elements

In order to ensure minimum signal loss in the printed circuits, impedance matched microstrip transmission lines, coplanar waveguides and antenna elements need to be designed. For easy

probing of the input RF signal on the flexible substrate, a grounded co-planar waveguide, as shown in Fig. 4.6.1.1 is designed so that both the signal and ground are on the top surface of the printed phased-array antenna system [87, 88]. In order to make the most compact circuit, microstrip transmission lines are used to carry signal throughout the circuit. The coupling region is chosen to be $L=\lambda_g/4$, where λ_g is the guided wavelength of the three-conductor line [88].
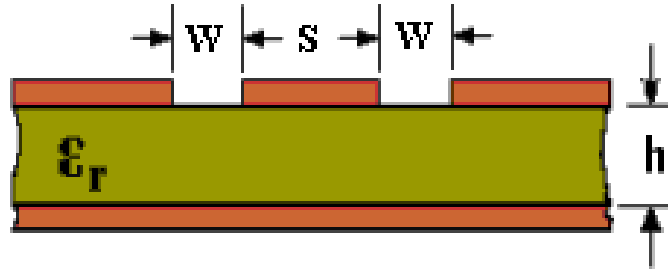

Fig. 4.6.1.1 Coplanar waveguide for probing

Here an infinite ground coplanar waveguide is designed for the transition. HFSS is used to calculate the impedance of the coupler. The dimension of the coplanar waveguide is shown in Fig. 4.6.1.1. The length of the coupler is $\lambda_g/4$. λ_g is the effective wavelength in the coplanar waveguide. From simulations, the dimensions of the coplanar waveguide for achieving 50Ohm impedance are found to be S=279µm, and W=219µm. Similarly, we also designed microstrip lines, and the width for 50Ohm impedance was calculated to be 279micron.

The antenna element is a microstrip antenna as shown in Fig. 4.6.1.2(a), which is basically a conductor printed on top of a layer of substrate with a ground plane on the back of the substrate. In most microstrip end fed antennas, the feed line impedance (50Ω) is not always the same as the radiation resistance at the edge of the patch, which is usually a few hundred ohms, depending on the patch dimensions and the substrate used. As a result this input mismatch will affect the antenna performance because maximum power is not being transferred. Thus, we use an inset feed at a distance x_0 as shown in Fig. 4.6.1.2(b) to match the resistance [89-91].
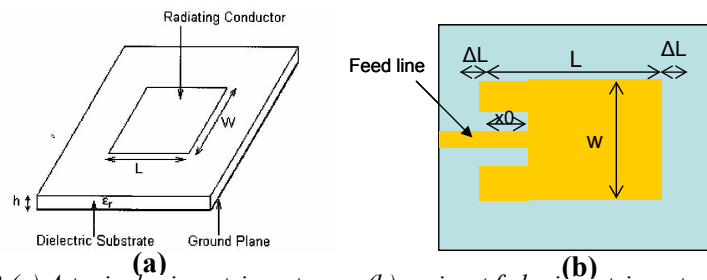

Fig. 4.6.1.2 (a) A typical microstrip antenna, (b) an inset fed microstrip antenna.

The design is intended to operate 4GHz frequency and at the same time keeping the return loss as large as possible. The width and the length of the patch is made approximately $\lambda_g/2$ (λ_g is the wavelength of the operating RF signal in the substrate). Since the dimension is designed to help maximize efficiency, we use the average of the value for ε_r of the substrate and ε_r of air (=1) to obtain a half-wavelength when we design the width W as shown in equation (4.6.1).

$$W = \frac{c}{2f_0 \sqrt{\frac{\varepsilon_r + 1}{2}}} \tag{4.6.1}$$

The effective dielectric constant due to the air/dielectric boundary is expressed as ε_{eff} and given by:

$$\varepsilon_{eff} = \frac{\varepsilon_r + 1}{2} + \frac{\varepsilon_r - 1}{2}(1 + \frac{10h}{W})^{-1/2} \tag{4.6.2}$$

Due to the fringing fields along the radiating edges of the antenna there is a line extension ΔL associated with the patch, which is given by:

$$\Delta L = 0.412h \frac{(\varepsilon_{eff} + 0.3)(\frac{W}{h} + 0.264)}{(\varepsilon_{eff} - 0.258)(\frac{W}{h} + 0.8)} \tag{4.6.3}$$

The effective length of the antenna due to the substrate dielectric constant is given by:

$$L_{eff} = \frac{c}{2f_0 \sqrt{\varepsilon_{eff}}} \tag{4.6.4}$$

Therefore, the design length of the microstrip antenna will be the effective length minus the line extension on both edges, which is expressed as

$$L = L_{eff} - 2\Delta L \tag{4.6.5}$$

The analysis of the inset fed distance is summarized in [91, 92] which uses a transmission line network model to analyze the antenna as in Fig. 4.6.1.3.
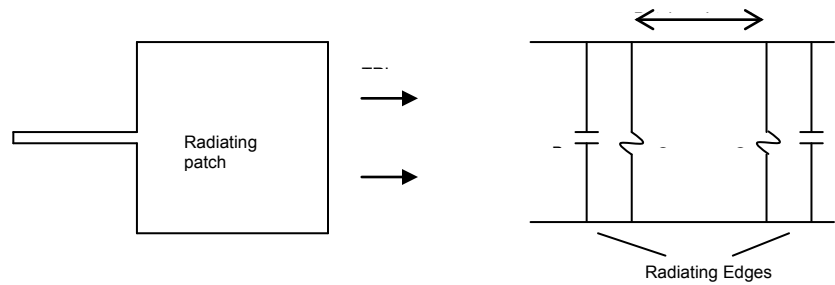

Fig. 4.6.1.3 Transmission line network model of a rectangular patch antenna.

The input resistance of the antenna is expressed as

$$R_{in} = \frac{1}{2(G_1 + G_{12})} \tag{4.6.6}$$

where G1 is self conductance, G12 is mutual conductance.

The self conductance can be calculated using the following expressions:

$$G_1 = \frac{I_1}{120\pi^2} \tag{4.6.7}$$

63

where I1 is the integral defined by:

$$I_1 = \int_0^{\pi} \left[\frac{\sin(\frac{k_0 W}{2} \cos \theta)}{\cos \theta} \right]^2 \sin^3 \theta \, d\theta \qquad (4.6.8)$$

where $k_0 = 2\pi / \lambda_0$.

The mutual conductance is calculated using the following expressions:

$$G_{12} = \frac{1}{120\pi^2} \int_0^{\pi} \left[\frac{\sin(\frac{k_0 W}{2} \cos \theta)}{\cos \theta} \right]^2 J_0(k_0 L \sin \theta) \sin^3 \theta \, d\theta \qquad (4.6.9)$$

where J0 is Bessel function of the first kind.

The input resistance for an inset fed patch is given by the simplified expression:

$$R_{in}(x = x_0) = \frac{1}{2(G_1 + G_{12})} \cos^2 (\frac{\pi x_0}{L}) \qquad (4.6.10)$$

where x_0 is the inset feed distance.

When $x_0 = 0$, the resistance at the edge of the patch can be found as:

$$R_{in}(x = 0) = \frac{1}{2(G_1 + G_{12})} \qquad (4.6.11)$$

The optimum value of x_0 for Rin=50Ω can be found using the following expression:

$$x_0 = \frac{L}{\pi} \arccos(\sqrt{\frac{50}{R_{in}}}) \qquad (4.6.12)$$

We designed an inset feed patch antenna working at 4 GHz. The dielectric material is Kapton polyimide with $127 \, \mu m$ thickness and dielectric constant of 3.5. The designed patch antenna parameters are W 2.5cm, L = 2cm, X_0 = 7.3mm. Since the notch width has little effect on the resonance frequency and the return loss, we just set it to three times of the width of input waveguide.

4.6.2 Design of 1-D and 2-D 4GHz Phased Array Antenna Systems

Using the components designed above, we designed 1-D and 2-D Phased Array Antenna systems. In this task, we designed 4-bit, 1x4 PAA; 2-bit 1x8 PAA; 4-bit 1x8 PAA; and 2-bit 2x2 PAA working at 4GHz frequency.
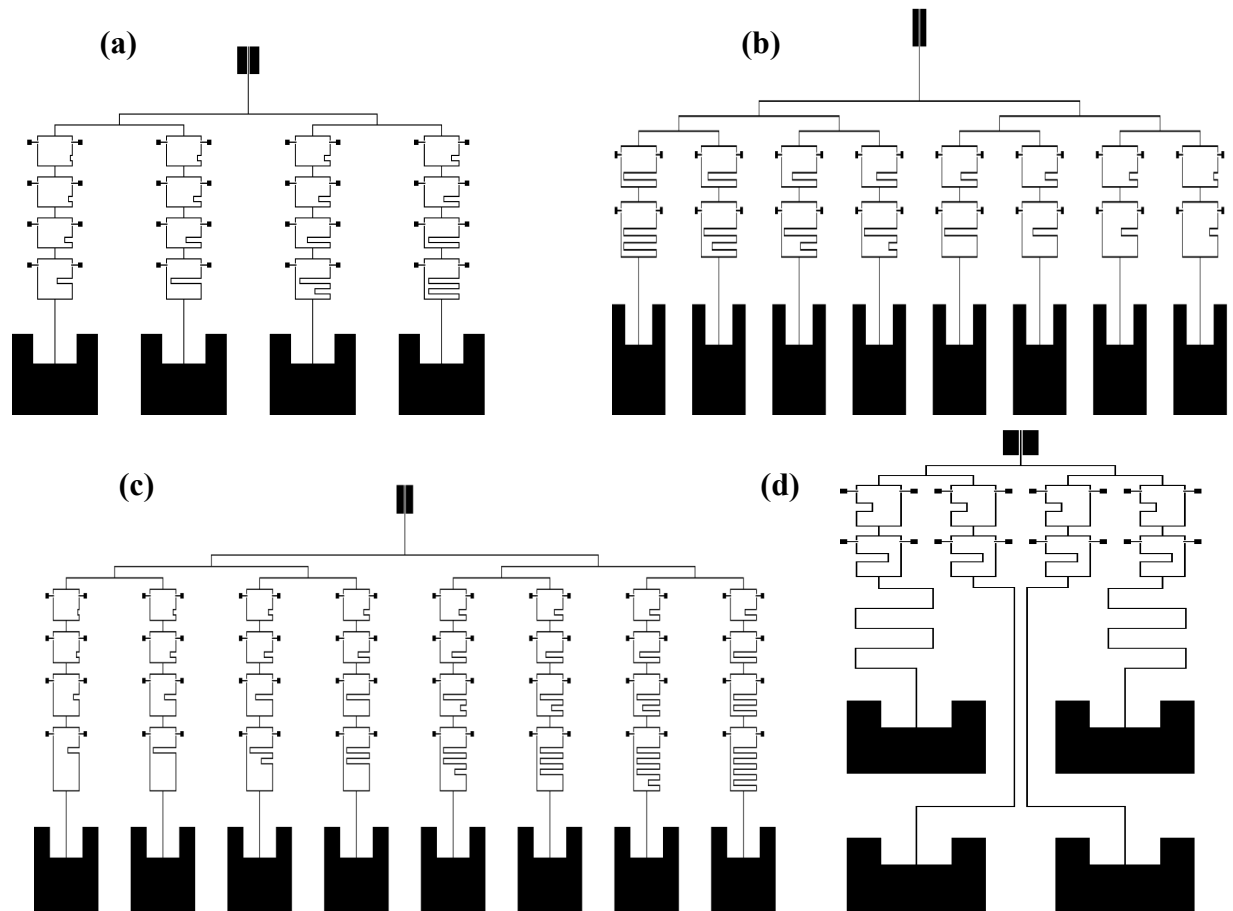
Fig. 4.6.2.1 Schematic layout of (a) 4-bit 1x4 PAA, (b) 2-bit 1x8 PAA, (c) 4-bit 1x8 PAA, and (d) 2-bit 2x2 PAA

Previously, we utilized a Dimatix DMP-2800 printer in order to achieve our 1x4 system. However, one disadvantage with the DMP system is that it can only print over an area of 8.5"x11". Therefore, using this printer, it is not possible to achieve larger antenna arrays (>1x8), or antenna arrays working at lower frequencies (due to large size of antenna elements). Therefore, we investigated a high-speed Roll-to-Roll (R2R) ink-jet printer at Omega. A picture of the printer is shown in Fig. 4.6.2.2.

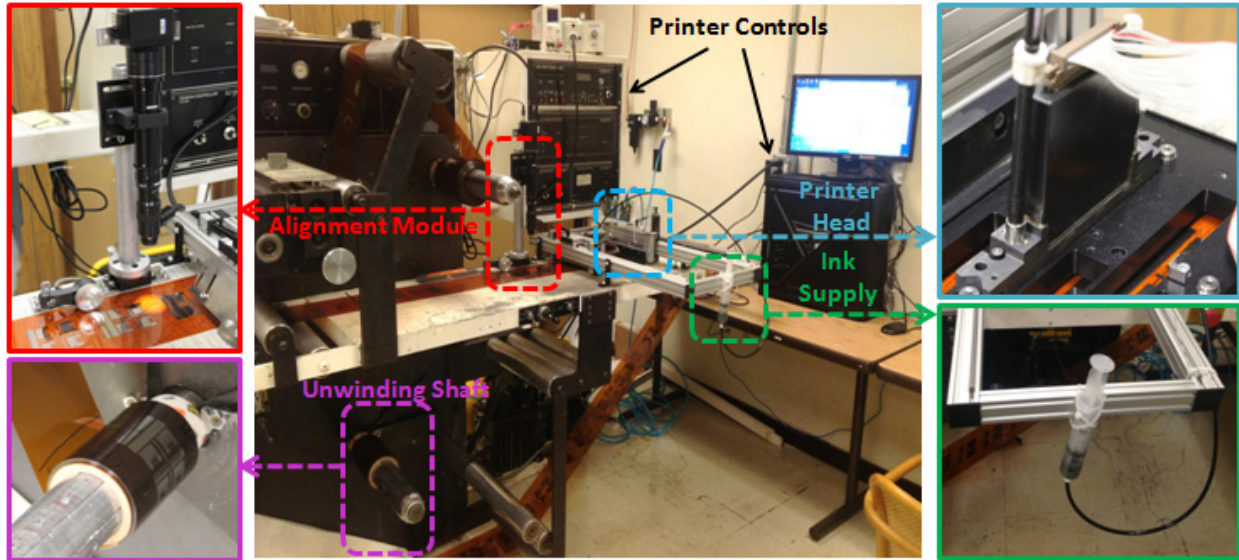*Fig. 4.6.2.2. R2R Ink-Jet Printer at Omega Optics, Inc.*

The Roll-to-Roll ink-jet printing system with alignment capability is a complex electric-mechanic system that contains the substrate moving module (web tracker, encoder), alignment module (illumination, image acquisition and processing) and printer module (printer server, printer head). The cartoon picture shows a schematic view of all the components and main connection used to align and print the second layer on top of the first layer.

- The tracker system is Arpeco Tracker with edge detection sensor. The sensor detects the edge and controls one of the shaft's tilting angle so that web edge can be aligned in real time to minimize the lateral direction (Y) offset and minimize web wander. The rewinding shaft runs slightly faster than the unwinding shaft to apply tensile stress on the web so that the web will be tightened. The web speed is adjustable and in this particular project, it is set around 15-20 meters/minute.

- The alignment module includes a CCD camera and an optical zoom-in lens that provide 5mm field of view (FOV). A picture of the alignment module on our printer is shown in Fig. 4.6.2.3. It should be noted that, in order to have quick response and refreshing rate, line scan camera is used so that each "frame" the CCD captures is 1 by 2048 pixels. By combing several frames, an image can be formed for image processing purpose. Also, to ensure the image can be transferred quickly, Base CameraLink interface is used which provides 1.8Gbps bandwidth for image transfer. Image acquisition board is installed in the controlling computer and LabVIEW from National Instrument is used to capture and analysis the image. The
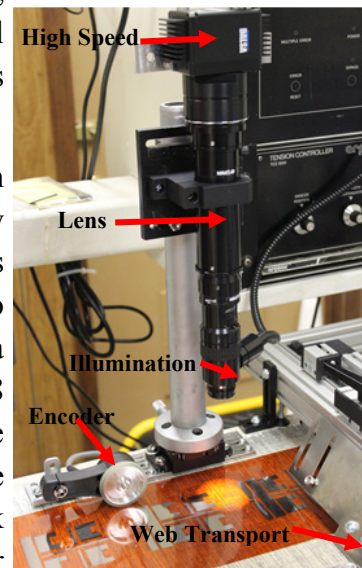

Fig. 4.6.2.3. Setup on the high-rate R2R ink-jet printer for achieving automatic in-line alignment and quality control

onset moment when the alignment mark falls within the FOV and image Y offset value will be provided and control the printer actuation. Detail alignment strategy will be provided below.

- Ink-jet printer software is provided by Global Inkjet System (GIS). The GIS Printer Manager Board controls the printer head through Ethernet cable using TCP/IP connection. Customized application can be developed to control the printer actuation.

Using such a printer, we printed the circuit consisting of printed silver transmission lines, coplanar waveguides, antenna elements, and contacts for gate/drain/source for FETs. The results for roll to roll printing are shown in Fig. 4.6.2.4.
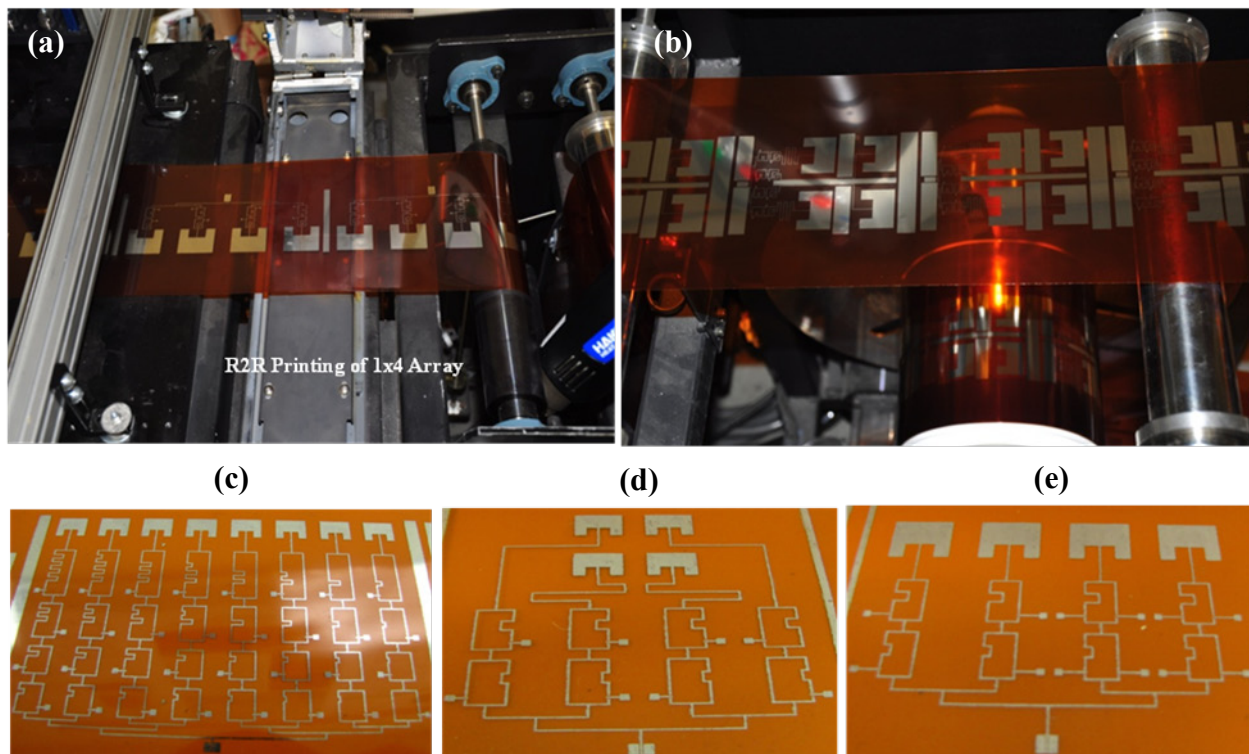

Fig. 4.6.2.4. (a-b) Roll-to-Roll printing showing 2-bit 1x4 and 2-bit 2x2 PAA. (c-e) Printed 4-bit 1x8 PAA, 2-bit 2x2 PAA and 2-bit 1x4 PAA.

We measured the far-field radiation pattern of the array in order to determine the performance of the printed array. A picture of the measurement setup used for the measurement is shown in Fig. 4.6.2.5. The RF signal from a network analyzer is fed to the antenna array via a coaxial cable and a micro probe. The radiated signal is received by a receiving horn antenna. The power received by the receiving antenna is measured on a microwave spectrum analyzer. The antenna array is mounted on a precision rotation stage. Therefore, by measuring the received power as a function of the angular position of the array, the far-field is obtained.

The measured far-field patterns for the array setup at two steering angles of 0° and -13.63^o are shown in Figs. 4.6.2.6 (a) and (b), respectively. The simulated patterns are also plotted together

with the measured data points. It can be seen that the measured and simulated curves agree well with each other, thus showing good performance of the printed layer.
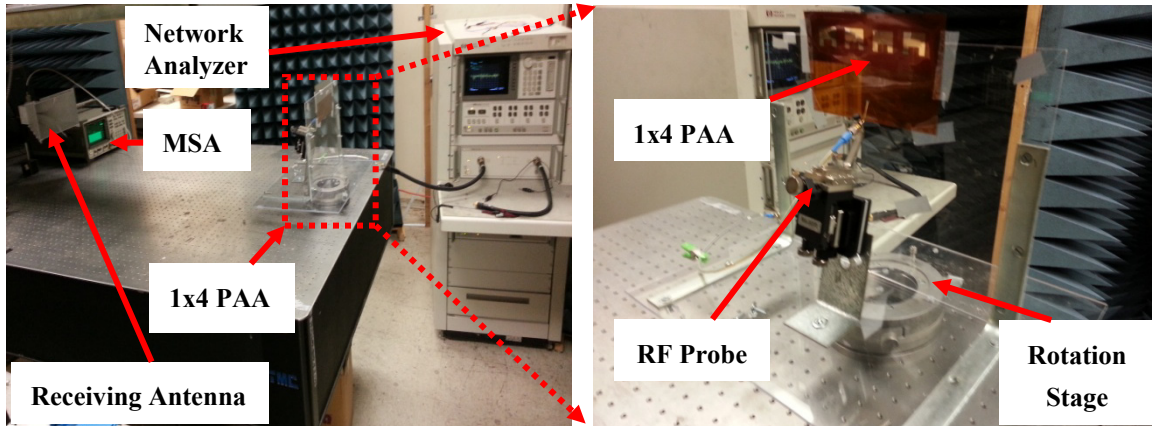

Fig. 4.6.2.5 Measurement setup for measuring the far-field radiation pattern of the printed 1x4 PAA.
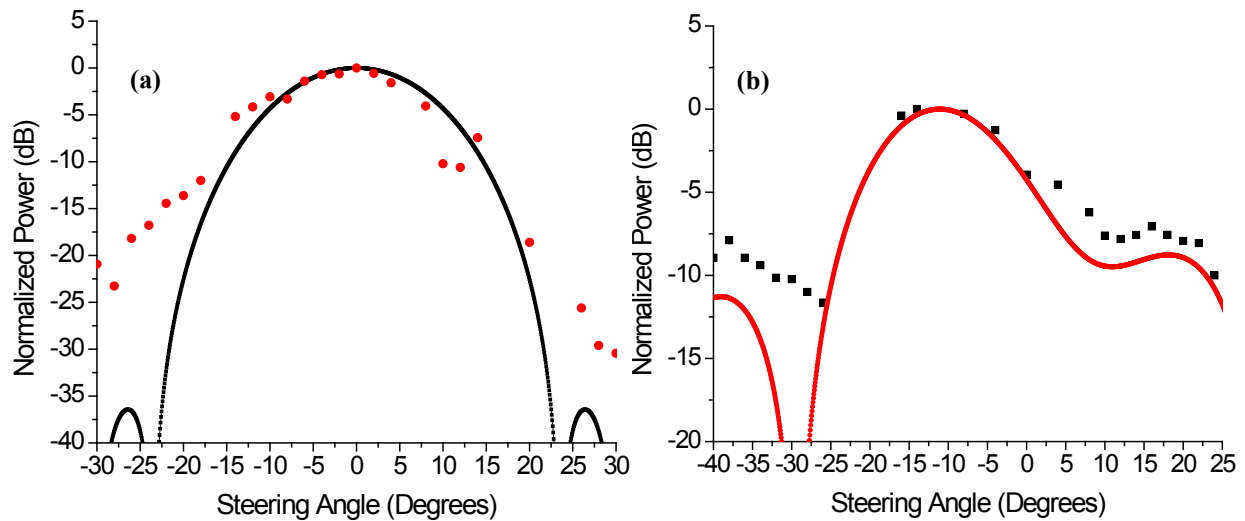

Fig. 4.6.2.6 Measured (data points) and Simulated (smooth curves) Far- Field radiation for the 1x4 PAA configured to steer at (a) 0° and (b) -13.63^o. The simulated and measured data agree well with each other

5. CONCLUSIONS

In the Phase II program, we have several important achievements related to silicon nanomembrane technology. We developed SiNM transfer schemes that can enable development of intricate photonic devices on any substrate. In order to couple light efficiently into SiNM based devices, we developed a subwavelength grating (SWG) coupler, that can achieve over 40% coupling efficiency using a single mode fiber. Several components crucial for the development of a conformal phased array antenna system, including compact modulator with highest slow down factor, PCW TTD lines with >216ps time delay, 1x16 MMI power splitters for array functionality, printed PAA system operation etc were demonstrated. For the first time, demonstration of SiNM photonic devices on other substrates such as glass, Kapton etc was performed. These achievements will lead to the widespread development and use of SiNM based high performance photonic components in several air-borne and space-borne applications.

6. PERSONNEL SUPPORTED

1. Dr. Harish Subbaraman - Research Scientist at Omega Optics, Inc. Dr. Subbaraman served as the PI on this program

2. Dr. Ray T. Chen - Professor - University of Texas at Austin. Dr. Chen served as the Co-PI on this program.

3. Mr. Xiaochuan Xu - Graduate Student at the University of Texas at Austin.

7. PUBLICATIONS RESULTING FROM PHASE II WORK

Our work in the Phase II program has resulted in several journal and conference proceedings. A list of publications is provided below.

Journal Publications

1. X. Xu, H. Subbaraman, A. Hosseini, D. Kwong, Yang Zhang, and R. T. Chen, "Single crystal silicon nanomembrane based photonics devices on unusual substrates," submitted to Optics Express (2012)
2. C.-Y. Lin, H. Subbaraman, A. Hosseini, Alan X. Wang, L. Zhu, and R. T. Chen, "Silicon nanomembrane based photonic crystal waveguide array for wavelength-tunable true-time-delay lines," Appl. Phys. Lett. 101 (5), 051101-051104 (2012).
3. H. Subbaraman, X. Xu, J. Covey, and R. T. Chen, "Efficient light coupling into in-plane semiconductor nanomembrane photonic devices utilizing a sub-wavelength grating coupler," Optics Express, Vol. 20, No. 18, pp. 20659-20665 (2012)
4. X. Xu, H. Subbaraman, J. Covey, D. Kwong, A. Hosseini, and R. T. Chen, "Complementary metal–oxide–semiconductor compatible high efficiency subwavelength grating couplers for silicon integrated photonics," Appl. Phys. Lett. 101, 031109 (2012)
5. A. Hosseini, X. Xu, H. Subbaraman, C. Lin, S. Rahimi, and R. Chen, "Large optical spectral range dispersion engineered silicon-based photonic crystal waveguide modulator," Opt. Express 20, 12318-12325 (2012).
6. X. Xu, H. Subbaraman, A. Hosseini, C. Lin, D. Kwong, and R. Chen, "Stamp printing of silicon-nanomembrane-based photonic devices onto flexible substrates with a suspended configuration," Opt. Lett. 37, 1020-1022 (2012).
7. S. Rahimi, A. Hosseini, X. Xu, H. Subbaraman, and R. T. Chen, "Group-index independent coupling to band engineered SOI photonic crystal waveguide with large slow-down factor," Opt. Express 19, 21832-21841 (2011)
8. A. Hosseini, X. Xu, H. Subbaraman, D. Kwong, Way Jiang, and R. T. Chen, "On the Role of Evanescent Modes and Group Index Tapering in Slow Light Photonic Crystal Waveguide Coupling Efficiency," Appl. Phys. Letts, vol. 98, pp. 031107, 2011.

Conference Publications

1. H. Subbaraman, X. Xu, and R. T. Chen, "Silicon nanomembrane based photonic crystal waveguide true-time-delay lines on a glass substrate," SPIE OPTO, Silicon Photonics VIII, 8629-49, San Francisco, CA, Feb 2-7, 8629-49 (2013)

2. H. Subbaraman, X. Xu, J. Covey, and R. T. Chen, "Subwavelength grating couplers for efficient light coupling into silicon nanomembrane based photonic devices," SPIE OPTO, Optoelectronic Interconnects XIII, 8630-48, San Francisco, CA, Feb 2-7, 8630-48 (2013)

3. X. Xu, H. Subbaraman, A. Hosseini, D. N. Kwong, and R. T. Chen, "Demonstration of silicon nanomembrane based photonic crystal waveguide PIN modulators on unusual substrates," SPIE OPTO, Silicon Photonics VIII, 8629-49, San Francisco, CA, Feb 2-7, 8629-51 (2013)

4. X. Xu, H. Subbaraman, J. Covey, D. N. Kwong, A. Hosseini, and R. T. Chen, "CMOS compatible subwavelength grating couplers for silicon integrated photonics," Photonics Conference (IPC), 2012 IEEE, vol., no., pp.350-351, 23-27 Sept. 2012

5. H. Subbaraman, X. Xu, Nassibe Rahimi, A. Hosseini and R. T. Chen, "Silicon nanomembranes for high performance flexible photonic interconnects and devices," in Optoelectronic Interconnects XII, SPIE OPTO, Proc. SPIE 8267, 82670H 21-26 January 2012, San Francisco, California United States 8267-15 (2012)

6. C.-Y. Lin, A. Hosseini, H. Subbaraman, Z. Xue, A. Wang, R. T. Chen, "Wavelength-Tunable on-Chip True Time Delay Lines Based on Photonic Crystal Waveguides for X-Band Phased Array Antenna Applications," CLEO 2012 Proceedings of the Conference on Lasers and Electro-Optics CTu3I.7 (2012)

7. X. Xu, H. Subbaraman, A. Hosseini, D. N. Kwong, C.-Y. Lin, R. T. Chen, "Stamp Printing of Silicon Nanomembrane Based Flexible Photonic Devices," CLEO 2012 Proceedings of the Conference on Lasers and Electro-Optics CM4A.7 (2012)

8. X. Xu, A. Hosseini, H Subbaraman, C.-Y. Lin, S. Rahimi, and R. T. Chen, "Extremely Low Vp×L Slow Light Photonic Crystal Modulator with GHz Bandwidth," IEEE Optical Interconnects Conference, paper WC5, 2012

9. A. Hosseini, X. Xu, D. Kwong, H. Subbaraman, and R. T. Chen, "On the Mechanism of Efficient Coupling into Slow Light Photonic Crystal Waveguides," OSA Quantum Electronics and Laser Science Conference (QELS), paper JTuI4, 2011

10. X. Xu, H. Subbaraman, Daniel Pham, A. Hosseini, Xiaohui Lin, and R. T. Chen, "Transfer and characterization of silicon nanomembrane based photonic devices on flexible polyimide substrate," Proc. of SPIE Vol. 7944, 79440F (2011)

8. REFERENCES

[1] H. Subbaraman, X. Xu, N. Rahimi, A. Hosseini and R. T. Chen, "Silicon nanomembranes for high performance flexible photonic interconnects and devices," in Optoelectronic Interconnects XII, SPIE OPTO, 21-26 January 2012, San Francisco, California United States 8267-15 (2011 accepted)

[2] X. C. Xu, H. Subbaraman, A. Hosseini, C. Y. Lin, D. Kwong, and R. T. Chen, "Stamp printing of silicon-nanomembrane-based photonic devices onto flexible substrates with a suspended configuration," Opt Lett 37, 1020-1022 (2012).

[3] X. Xu, H. Subbaraman, J. Covey, D. Kwong, A. Hosseini, and R. T. Chen, "Complementary metal-oxide-semiconductor compatible high efficiency subwavelength grating couplers for silicon integrated photonics," Appl Phys Lett 101, 031109-031104 (2012).

[4] X. Xu, H. Subbaraman, A. Hosseini, D. Kwong, Y. Zhang, and R. T. Chen, "Single crystal silicon nanomembrane based photonics devices on unusual substrates," submitted to Optics Letters (2012)

[5] X. Xu, H. Subbaraman, A. Hosseini, D. N. Kwong, R. T. Chen, "Demonstration of silicon nanomembrane based photonic crystal waveguide PIN modulators on unusual substrates," SPIE OPTO [Accepted]

[6] H. Subbaraman, X. Xu, J. Covey, and R. T. Chen, "Efficient light coupling into in-plane semiconductor nanomembrane photonic devices utilizing a sub-wavelength grating coupler," Opt. Express 20, 20659-20665 (2012).

[7] S. Rahimi, A. Hosseini, X. Xu, H. Subbaraman, and R. T. Chen, "Group-index independent coupling to band engineered SOI photonic crystal waveguide with large slow-down factor," Optics Express 19, 21832-21841 (2011).

[8] A. Hosseini, X. Xu, H. Subbaraman, C.-Y. Lin, S. Rahimi, and R. T. Chen, Large optical spectral range dispersion engineered silicon-based photonic crystal waveguide modulator, Opt. Express, Vol.20, No. 11, pp. 12318-12325 (2012)

[9] C.-Y. Lin, H. Subbaraman, A. Hosseini, L. Zhu, A. X. Wang, and R. T. Chen, "Silicon Nanomembrane Based Photonic Crystal Waveguide Array for Wavelength-Tunable True-Time-Delay Lines," Appl. Phys. Letts, Vol. 101. pp. 4739003 (2012)

[10] H. Subbaraman, X. Xu, and R. T. Chen, "Silicon nanomembrane based photonic crystal waveguide true-time-delay lines on a glass substrate," SPIE OPTO, Silicon Photonics VIII, 8629-49, San Francisco, CA, Feb 2-7 (2013) [accepted]

[11] R. G. Heideman, R. P. H. Kooyman, and J. Greve, "Performance of a highly sensitive optical waveguide Mach–Zehnder interferometer immunosensor," Sens. Actuators B, vol. 10, pp. 209–217 (1993)

[12] B. J. Luff, R. D. Harris, and J. S. Wilkinson, "Integrated-optical directional coupler biosensor," Opt. Lett., vol. 21, no. 8, pp. 618-620 (1996)

[13] H. Sohlström and M. Öberg, "Refractive index measurement using integrated ring resonators," Proceedings of the 8th European Conference on Integrated Optics (EICO'97), pp. 322-325 (1997)

[14] A. Yalçin et al., "Optical sensing of biomolecules using microring resonators," IEEE J. Sel. Top. Quant. Elec. vol. 12, pp. 148-155 (2006)

[15] K. De Vos, I. Bartolozzi, E. Schacht, P. Bienstman, and R. Baets, "Silicon-on-insulator microring resonator for sensitive and label-free biosensing," Opt. Express. vol. 15, pp. 7610-7615 (2007)

[16] A. Schweinsberg, S. Hocdé, N. N. Lepeshkin, R. W. Boyd, C. Chase, and J. E. Fajardo, "An environmental sensor based on an integrated optical whispering gallery mode disk resonator," Sens. Act. B. vol. 123, pp. 727-732 (2007)

[17] N. A. Mortensen and S. Xiao, "Slow-light enhancement of Beer-Lambert-Bouguer absorption," Appl. Phys. Lett. vol. 90, pp. 141108 (2007)

[18] B . Jalali and S. Fathpour, "Silicon photonics," J. Lightwave Technol. vol. 24, pp. 4600-4615 (2006)

[19] F. Cavallo and M. G. Lagally, "Semiconductors turn soft: inorganic nanomembranes," Soft Matter. vol. 6, 439 – 455 (2010)

[20] M. M. Roberts et al., "Elastically relaxed free-standing strained-silicon nanomembranes," Nat. Mater. vol. 5, pp. 388-393 (2006)

[21] D. Kim, J. Ahn, W. Choi, H. Kim, T. Kim, J. Song, Y. Huang, Z. Liu, C. Lu, and J. Rogers, "Stretchable and foldable silicon integrated circuits," Science. vol. 320, pp. 507 (2008)

[22] H. C. Yuan et al., "Silicon-based nanomembrane materials: the ultimate in strain engineering," Silicon Monolithic Integrated Circuits in RF Systems, 2005. Digest of Papers. 2005 Top. Meeting on, pp. 327-333 (2005)

[23] H. C. Yuan, MM. Ma, Z., Roberts, D. E. Savage, and M. G. Lagally, "High-speed strained-single-crystal-silicon thin-film transistors on flexible polymers," J. Appl. Phys. vol. 100, pp. 013708 (2006)

[24] H. Yang, Z. Qiang, H. Pang, Z. Ma, and W. D. Zhou, "Surface-Normal Fano Filters Based on Transferred Silicon Nanomembranes on Glass Substrates," Elec.. Lett. vol.44, pp. 858-859 (2008)

[25] W. Zhou et al., "Semiconductor nanomembranes for stacked and flexible photonics," Proc. SPIE. vol. 7606, pp. 76060U (2010)

[26] T. Saha, and W. Zhou, "High efficiency diffractive grating coupler based on transferred silicon nanomembrane overlay on photonic waveguide," J. Phys. D. vol. 42, pp. 085115 (2009)

[27] J. P. Hugonin, P. Lalanne, T. P. White, and T. F. Krauss, Opt. Lett. 32, 2638 (2007)

[28] C. Martijn de Sterke, K. B. Dossou, T. P. White, L. C. Botten, and R. C. McPhedran, Opt. Express 17, 17338 2009

[29] N. Ozaki et al., "High transmission recovery of slow light in a photonic crystal waveguide using a hetero groupvelocity waveguide," Opt. Express 15, 7974-7983 (2007).

[30] Y. Hamachi, S. Kubo, and T. Baba, "Slow light with low dispersion and nonlinear enhancement in a lattice-shifted photonic crystal waveguide," Opt. Lett. 34, 1072-1074 (2009).

[31] P. Pottier, M. Gnan, and R. M. De La Rue, "Efficient coupling into slow-light photonic crystal channel guides using photonic crystal tapers," Opt. Express 15, 6569-6575 (2007).

[32] S. Assefa et al., "Coupling into Slow-Light in Photonic Crystal Waveguides," OSA in Conference on Lasers and Electro-Optics/Quantum Electronics and Laser Science Conference and Photonic Applications Systems Technologies, paper QThJ1, (2008).

[33] C.-Y. Lin et al., "Wideband group velocity independent coupling into slow light silicon photonic crystal waveguide," Appl. Phys. Lett. 97, 183302 (2010).

[34] R. J. P. Engelen, D. Mori, T. Baba, and L. Kuipers, "Two Regimes of Slow-Light Losses Revealed by Adiabatic Reduction of Group Velocity," Phys. Rev. Lett. 101, 103901 (2008).

[35] M. Patterson, S. Hughes, S. Combrié, N. V. Tran, A. De Rossi, R. Gabet, and Y. Jaouën, "Disorder-induced coherent scattering in slow-light photonic crystal waveguides," Phys. Rev. Lett. 102(25),253903–253906 (2009).

[36] L. H. Frandson, A. V. Lavrinenko, J. Fage-Pedersen and P. I. Borel, "Photonic crystal waveguides with semi-slow light and tailored dispersion properties", Optics Express 14, 9444-9450 (2006).

[37] S. A. Schulz, L. O'Faolain, D. M. Beggs, T. P. White, A. Melloni, and T. F. Krauss, "Dispersion engineered slow light in photonic crystals: a comparison," J. Opt. 12(10), 104004 (2010).

[38] J. Li, T. P. White, L. O'Faolain, A. Gomez-Iglesias and T. F. Krauss, "Systematic design of flat band slow light in photonic crystal waveguides", Optics Express 16, 6227-6232 (2008).

[39] Y. Hamachi, S. Kubo and T. Baba, "Slow light with low dispersion and nonlinear enhancement in a lattice-shifted photonic crystal waveguide", Optics Letters 34, 1072-1074 (2009).

[40] R. Hao et al., "Improvement of delay-bandwidth product in photonic crystal slow-light waveguides," Opt. Express 18, 16309-16319 (2010).

[41] J. Nocedal and S. Wright, NumericalOptimization. NewYork: Springer-Verlag (1999).

[42] S. G. Johnson et al., "Adiabatic theorem and continuous coupled-mode theory for efficient taper transitions in photonic crystals", Physical Review E, 66, 066608 (2002)

[43] P. Pottier, M. Gnan, and R. M. De La Rue, "Efficient coupling into slow-light photonic crystal channel guides using photonic crystal tapers," Opt. Express 15, 6569-6575 (2007).

[44] J. P. Hugonin, P. Lalanne, T. P. White, and T. F. Krauss, "Coupling into slow-mode photonic crystal waveguides," Opt. Lett. 32, 2638-2640 (2007).

[45] N. Ozaki et al., "High transmission recovery of slow light in a photonic crystal waveguide using a hetero groupvelocity waveguide," Opt. Express 15, 7974-7983 (2007).

[46] C. Martijn de Sterke, K. B. Dossou, T. P. White, L. C. Botten, and R. C. McPhedran, "Efficient coupling into slow light photonic crystal waveguide without transition region: role of evanescent modes," Opt. Express 17, 17338-17343 (2009).

[47] Y. Cui, K. Liu, D. L. MacFarlane, and J.-B. Lee, "Thermo-optically tunable silicon photonic crystal light modulator," Opt. Lett. 35, 3613-3615 (2010).

[48] A. Gomez-Iglesias et al., "Direct measurements of the group index of photonic crystal waveguide via Fourier transform spectral interferometry", Applied physics Letters 90, 261107 (2007)

[49] Y. A. Vlasov and S. J. McNab, "Coupling into the slow light mode in slab-type photonic crystal waveguides," Opt. Lett. 31, 50-52 (2006).

[50] R. Jacobsen et al., "Direct experimental and numerical determination of extremely high group indices in photonic crystal waveguides," Opt. Express 13, 7861-7871 (2005).

[51] M. Soljačić, S. G. Johnson, S. Fan, M. Ibanescu, E. Ippen, and J. Joannopoulos, "Photonic-crystal slow-light enhancement of nonlinear phase sensitivity," JOSA B 19, 2052-2059 (2002).

[52] Y. Jiang, W. Jiang, L. Gu, X. Chen, and R. T. Chen, "80-micron interaction length silicon photonic crystal waveguide modulator," Applied Physics Letters 87, 221105 (2005).

[53] L. Gu, W. Jiang, X. Chen, and R. T. Chen, "Physical mechanism of pin-diode-based photonic crystal silicon electrooptic modulators for gigahertz operation," Selected Topics in Quantum Electronics, IEEE Journal of 14, 1132-1139 (2008).

[54] Y. Tang, and B. Wang, "Study of active width-reduced line-defect photonic crystal waveguides for high speed applications," (2008), p. 71350R.

[55] L. O'Faolain et al., "Loss engineered slow light waveguides," Optics Express 18, 27627-27638 (2010).

[56] L. Gu, Micro-and nano-periodic-structure-based devices for laser beam control 99-100 (ProQuest, 2007).

[57] H. C. Nguyen, Y. Sakai, M. Shinkawa, N. Ishikura, and T. Baba, "10 Gb/s operation of photonic crystal silicon optical modulators," Optics Express 19, 13000-13007 (2011).

[58] J. A. Rogers, et al., "Paper-like electronic displays: Large-area rubber-stamped plastic sheets of electronics and microencapsulated electrophoretic inks," P Natl Acad Sci USA 98, 4835-4840 (2001).

[59] D. H. Kim, et al., "Stretchable and foldable silicon integrated circuits," Science 320, 507-511 (2008).

[60] W. D. Zhou, et al., "Flexible photonic-crystal Fano filters based on transferred semiconductor nanomembranes," J Phys D Appl Phys 42, 234007-234017 (2009).

[61] L. Chen, et al., "Polarization and angular dependent transmissions on transferred nanomembrane Fano filters," Opt Express 17, 8396-8406 (2009).

[62] T. Someya, et al., "Integration of organic FETs with organic photodiodes for a large area, flexible, and lightweight sheet image scanners," IEEE T Electron Dev 52, 2502-2511 (2005).

[63] M. J. Zablocki, et al., "W. Nanomembrane enabled nanophotonic devices," Proceedings of the SPIE 7606, 9 (2010).

[64] M. J. Zablocki, et al., "Nanomembrane transfer process for intricate photonic device applications," Opt. Lett. 36, 58-60 (2011).

[65] M. A. Meitl, et al., "Transfer printing by kinetic control of adhesion to an elastomeric stamp," Nat Mater 5, 33-38 (2006).

[66] S. Kim, et al. "Microstructured elastomeric surfaces with reversible adhesion and examples of their use in deterministic assembly by transfer printing," P Natl Acad Sci USA 107, 17095-17100 (2010).

[67] S. I. Park, et al., "Light Emission Characteristics and Mechanics of Foldable Inorganic Light-Emitting Diodes," Adv Mater 22, 3062-3066 (2010).

[68] J. Yoon, et al., "GaAs photovoltaics and optoelectronics using releasable multilayer epitaxial assemblies," Nature 465, 329-U380 (2010).

[69] G. Shin, et al., "Micromechanics and Advanced Designs for Curved Photodetector Arrays in Hemispherical Electronic-Eye Cameras," Small 6, 851-856 (2010).

[70] T. Santeri and F. Sami, "Wafer-Level Bonding of MEMS Structures with SU-8 Epoxy Photoresist," Physica Scripta 2004, 223 (2004).

[71] R. S. Jacobsen, K. N. Andersen, P. I. Borel, J. Fage-Pedersen, L. H. Frandsen, O. Hansen, M. Kristensen, A. V. Lavrinenko, G. Moulin, H. Ou, C. Peucheret, B. Zsigri, and A. Bjarklev, "Strained silicon as a new electro-optic material," Nature 441, 199-202 (2006).

[72] M. Asghari and A.V. Krishnamoorthy, "Silicon photonics: Energy-efficient communication," Nat Photon 5 (5), 268 (2011).

[73] M. Lipson, "Guiding, Modulating, and Emitting Light on Silicon-Challenges and Opportunities," J. Lightwave Technol. 23 (12), 4222 (2005).

[74] L. Liu, M. Pu, K. Yvind, and J. M. Hvam, "High-efficiency, large-bandwidth silicon-on-insulator grating coupler based on a fully-etched photonic crystal structure," Appl Phys Lett 96 (5), 051126 (2010).

[75] T. Shoji, T. Tsuchizawa, T. Watanabe, K. Yamada, and H. Morita, "Low loss mode size converter from 0.3 mu m square Si wire waveguides to singlemode fibres," Electron Lett 38 (25), 1669 (2002).

[76] S. J. McNab, N. Moll, and Y. A. Vlasov, "Ultra-low loss photonic integrated circuit with membrane-type photonic crystal waveguides," Opt Express 11 (22), 2927 (2003).

[77] M. Pu, L. Liu, H. Ou, K. Yvind, and J. M. Hvam, "Ultra-low-loss inverted taper coupler for silicon-on-insulator ridge waveguide," Optics Communications 283 (19), 3678 (2010).

[78] V. R. Almeida, R. R. Panepucci, and M. Lipson, "Nanotaper for compact mode conversion," Opt. Lett. 28 (15), 1302 (2003).

[79] P. Cheben, D. X. Xu, S. Janz, and A. Densmore, "Subwavelength waveguide grating for mode conversion and light coupling in integrated optics," Opt Express 14 (11), 4695 (2006).

[80] P. Cheben, P. J. Bock, J. H. Schmid, J. Lapointe, S. Janz, D. X. Xu, A. Densmore, A. Delage, B. Lamontagne, and T. J. Hall, "Refractive index engineering with subwavelength gratings for efficient microphotonic couplers and planar waveguide multiplexers," Opt Lett 35 (15), 2526 (2010).

[81] P. Yeh, A. Yariv, and C.-S. Hong, "Electromagnetic propagation in periodic stratified media. I. General theory," J. Opt. Soc. Am. 67 (4), 423 (1977).

[82] R. Halir, et al., "Waveguide grating coupler with subwavelength microstructures," Opt. Lett. 34 (9), 1408 (2009).

[83] D. Taillaert, P. Bienstman, and R. Baets, "Compact efficient broadband grating coupler for silicon-on-insulator waveguides," Opt. Lett. 29 (23), 2749 (2004).

[84] S. M. Rytov, "Electromagnetic properties of finely stratified medium," Sov. Phys. JETP 2 (3), 10 (1956).

[85] X. Chen and H. K. Tsang, "Polarization-independent grating couplers for silicon-on-insulator nanophotonic waveguides," Opt. Lett. 36 (6), 796 (2011).

[86] C. R. Doerr, Chen Long, Chen Young-Kai, and L. L. Buhl, "Wide Bandwidth Silicon Nitride Grating Coupler," Photonics Technology Letters, IEEE 22 (19), 1461 (2010).

[87] D. Pavlidis and H. L. Hartnagel, The design and performance of three-line microstrip couplers, IEEE Trans. Microwave Theory and Tech. 24, pp. 631-640 (1976)

[88] G. P. Gauthier, etc, W-band Finite Ground Coplanar waveguide (FGCPW) to Microstrip Line Transition, IEEE MTT-S Digest, TU2E-3, pp. 107-109 (1998)

[89] K. R. Carver and J.W. Mink, Microstrip Antenna Technology, IEEE Trans. Antenna propagation. AP-29, pp 2-24 (1981).

[90] J. R. James, P. S. Hall and C. Wood, Microstrip Antenna Theory and Design. London, United Kingdom, Peter Peregrinus, pp 87-89 (1981)

[91] Balanis, C.A. Op Cit. pp 730-734.

[92] James J.R., P.S.Hall and C. Wood. Microstrip Antenna Theory and Design. London, United Kingdom, Peter Peregrinus 1981., pp 87-89.